



MICROFLUIDIC POWER GENERATION

THESIS

Aaron J. Sprecher, Captain, USAF

AFIT/GE/ENG/08-29

**DEPARTMENT OF THE AIR FORCE
AIR UNIVERSITY**

AIR FORCE INSTITUTE OF TECHNOLOGY

Wright-Patterson Air Force Base, Ohio

APPROVED FOR PUBLIC RELEASE; DISTRIBUTION UNLIMITED

The views expressed in this thesis are those of the author and do not reflect the official policy or position of the United States Air Force, Department of Defense, or the U.S. Government.

AFIT/GE/ENG/08-29

MICROFLUIDIC POWER GENERATION

THESIS

Presented to the Faculty

Department of Electrical and Computer Engineering

Graduate School of Engineering and Management

Air Force Institute of Technology

Air University

Air Education and Training Command

In Partial Fulfillment of the Requirements for the
Degree of Master of Science in Electrical Engineering

Aaron J. Sprecher, BSEE

Captain, USAF

March 2008

APPROVED FOR PUBLIC RELEASE; DISTRIBUTION UNLIMITED

MICROFLUIDIC POWER GENERATION

Aaron J. Sprecher, BSEE

Captain, USAF

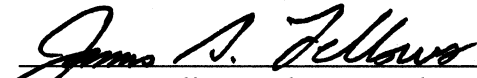
Approved:



LaVern A. Starman, PhD, Maj, USAF (Chairman)

5 Mar 08

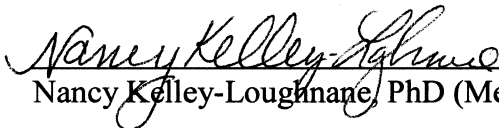
Date



James A. Fellows, PhD, Lt Col, USAF (Member)

5 MAR 08

Date



Nancy Kelley-Loughnane, PhD (Member)

28 Feb 08

Date

Abstract

This thesis includes the detailed mathematical calculations used to determine the feasibility of harnessing electrical energy from the blood flow through human capillaries. The designs are inspired by human physiology and well established electromagnetic energy harvesting techniques and the fabrication methods have been proposed for the various components of the device. The fabrication and the design of these components have also been extensively analyzed using calculations based on the governing principles of microfluidics, kinetics, and electromagnetics. The analysis has confirmed that this design can produce sufficient energy to power a MEMS device using non-standard materials and fabrication methods. The designs were based on a standard hydroelectric dam model, modified to account for the biological aspects. Nickel and gold were selected as the primary components of the electromagnetic portion of the device because of their electromagnetic properties and the ability to deposit and pattern them. Of the four portions of the device, the coil was fully fabricated, experiments were conducted for the fabrication of the stator and the microchannels and the proposed fabrication method was explained for the turbine. Three sets of the gold induction coils were fabricated, each with different thicknesses, but the same width and length. Since the resistance of the coil is determined by the resistivity of the material and the dimensions, the cross-sectional area of these coils determined the differences in resistance. As predicted, the average resistance increased as thickness decreased. However, the resistance was greater than calculated for the two thinner coil sets due to fabrication methods.

Acknowledgments

I would like to express my sincere appreciation to my faculty advisor, Maj LaVern Starman, for his guidance and support throughout the course of this thesis effort. The insight and experience was certainly appreciated. I would also like to thank my sponsor, Dr. Nancy Kelley-Loughnane, from the Air Force Research Laboratory – Human Effectiveness Directorate for both the support and latitude provided to me in this endeavor and Capts Mark Bellott and Derrick Langley from the Air Force Research Laboratory – Sensors Directorate without who's assistance I could not have overcome the many fabrication difficulties that were encountered.

Aaron J. Sprecher

Table of Contents

	Page
Abstract.....	iv
Acknowledgments	v
Table of Contents	vi
List of Figures.....	x
List of Tables	xviii
Foreword.....	xx
I. Introduction to BioMEMS.....	1
1.1. The Need for Microfluidic Power Generation	1
1.2. Microelectromechanical Systems (MEMS)	2
<i>1.2.1. BioMEMS</i>	<i>3</i>
<i>1.2.2. Microfluidics</i>	<i>5</i>
1.3. Problem Overview: Limitations in MEMS and Microfluidics	5
1.4. Intent of Research.....	6
<i>1.4.1. Proposed Solution and Research Objectives</i>	<i>8</i>
<i>1.4.2. End Goal of Microfluidic Power Generation Project</i>	<i>8</i>
<i>1.4.3. Design Requirements</i>	<i>9</i>
1.5. Organization of Thesis	9
II. Literature Review	10
2.1. Chapter Overview	10
<i>2.1.1. Historical Perspective.....</i>	<i>10</i>
<i>2.1.2. Potential Microfluidic Power Generation Applications</i>	<i>11</i>
2.2. Microfluidics: A Drop in the Bucket	13

2.3. Turbines: Turning the Wheel of History.....	17
2.4. Electromagnetism: The Interaction of Charged Particles.....	19
2.5. MEMS Energy Harvesting: Energy from the Ether	21
2.6. Relevant Research	22
2.6.1. <i>Similar Designs</i>	22
2.6.2. <i>Microfluidic Power Generation</i>	23
2.7. Chapter Summary	25
III. Theory	26
3.1. Chapter Overview	26
3.2. Fluid Dynamics	26
3.2.1. <i>Turbulent vs. Laminar Flow</i>	28
3.2.2. <i>Fluid in Microchannels</i>	29
3.3. Transduction: Mechanical to Electrical Energy Transfer.....	31
3.4. Chapter Summary	33
IV. Calculations.....	34
4.1. Chapter Overview	34
4.2. Calculations.....	35
4.2.1. <i>Fluid Flow in Microchannels</i>	35
4.2.2. <i>Turbine Rotation</i>	39
4.2.3. <i>Electromagnetic Induction</i>	42
4.3. Chapter Summary	49
V. Designs.....	51
5.1. Chapter Overview	51

5.2. Design Inspiration	51
5.2.1. Inspiration From Human Physiology	51
5.2.2. Inspiration From Hydro-Electric Dam	55
5.3. Design Details.....	56
5.3.1. Microfluidic Channel Design	56
5.3.2. Original Generator Design (Gear Ratio Design)	57
5.3.3. Revised Generator Design (Flat Coil Design).....	60
5.4. Dominant Design Elements.....	62
5.4.1. Fluid Flow Rate.....	62
5.4.2. Turbine Size (Rate of Rotation)	63
5.4.3. Dimensions and Material for Stator Magnets.....	63
5.4.4. Coil Size and Number of Loops	65
5.5. Chapter Summary	66
VI. Fabrication	67
6.1. Chapter Overview	67
6.2. Glass Slides.....	67
6.3. Turbine and Shaft.....	68
6.4. Coil.....	71
6.5. Stator	77
6.6. Chapter Summary	81
VII. Analysis and Results	82
7.1. Chapter Overview	82
7.2. Coil.....	82

7.2.1. <i>Coil Resistance</i>	84
7.2.2. <i>Current Carrying Capacity</i>	88
7.3. Stator	89
7.3.1. <i>Deformation Due to Strain</i>	89
7.3.2. <i>Magnetization</i>	91
7.4. Chapter Summary	92
VIII. Conclusions and Recommendations	93
8.1. Chapter Overview	93
8.2. Thesis Review	93
8.3. Scientific Contributions	94
8.4. Recommendations	94
8.4.1. <i>Continuation of Power Generation Evaluation</i>	95
8.4.2. <i>Examination of Alternate Power Generation Designs</i>	97
8.4.3. <i>Energy Storage Capabilities</i>	97
8.4.4. <i>Integration of Probes and Control Circuitry</i>	97
8.5. Conclusions	98
Appendix A: Mathematica Code	99
Appendix B: Mask Designs	119
Appendix C: Fabrication Methods	134
Appendix D: Experiments and Raw Data	139
Bibliography	148
Vita	153

List of Figures

Figure 1.1: Standard Diabetic Glucose Monitoring Equipment including diagnostic meter, lancet for piercing skin and test strip for collecting blood and transporting it to the diagnostic meter [2]	1
Figure 1.2: The AbioCor implantable replacement heart uses an implanted electronics package to monitor and control pumping speed of the heart based on the physiological needs of the patient [5].	3
Figure 1.3: The Learning Retinal Implant from Intelligent Medical Systems. It is designed to help patients with retinitis pigmentosa. The eye glasses and photoprocessor worn on the waist are used to train the retinal implant, thus restoring vision [5].	4
Figure 1.4: Braingate neural implant devised by Brown University. The implantable chip will enable the mind to manipulate electronic devices and may lead to restored mobility in paralyzed patients [5].	4
Figure 1.5: Theoretical image of the completed MicroFluidic Power Generation (MFPG) device showing the outer shape, the microchannel, and the protein coating at the opening of the microchannel. The turbine, generator and microchannel probes are not shown.	7
Figure 2.1: Individual organs drawn in inks and opaque watercolors from an 18th century Persian translation of an Arabic medical compendium [12].	11
Figure 2.2: Implanted pacemaker used to regulate electrical activity in the heart [14]....	12
Figure 2.3: Graphical representation of a microchannel with particulate fluid flow and analysis probes. Each probe pair is coated to identify a specific type of particle.	13
Figure 2.4: Diagram of a gas chromatograph used for sample analysis [15]. This method often made identification of small samples impossible.....	14
Figure 2.5: Micronit Lab-on-a-Chip microfluidic analysis tool shown with glass microreactor chip [6].	15
Figure 2.6: Effects of viscosity on fluid flow in a channel.....	16
Figure 2.7: Cross-sectional views of an axial-flow turbine (a) [22] and an impulse turbine (b) [23]	18

Figure 2.8: Voltaic pile consisting of a series of alternating zinc and copper disks separated by cardboard soaked with an acid or salt solution [25]	20
Figure 2.9: Cross-section of Micro-engineered turbo-generator based on an axial-flow turbine. The generator uses permanent magnets (magnetite), which are inserted after the rotor is fabricated [27].	22
Figure 2.10: A schematic of the mobile-ion-drain method. (a) Surface has adopted a charge when in contact with water and electron double layer forms; (b) A stable streaming potential exists due to the water flow and accumulation of mobile ions; (c) The mobile ions in (b) have drained and the surface will disassociate and become negatively charged; (d) The surface has become more negatively charged when flow resumes, resulting in a larger streaming potential.	24
Figure 3.1: Turbulent fluid flow due to an object in the path of the flow [33]	28
Figure 3.2: Simulation of a laminar fluid flow through a cylindrical pipe [35]	29
Figure 3.3: Rendition of a human capillary shown with red blood cells and pressure gradients (red-brown arrows) [36]	30
Figure 4.1: Fluid pressure in the microchannel as a function of channel length. Pressure at the channel inlet is 5332.9 N/m^2	38
Figure 4.2: Change in flow rate as a function of capillary length, for a given change in pressure.	38
Figure 4.3: Cross-sectional view of turbine showing fluid pressure and resultant torque.	41
Figure 4.4: Vector diagram for the angular velocity of a particle in a 2-dimensional plane [39]	42
Figure 4.5: Side view (a) and end view (b) illustration of Ampere-Maxwell current induction in a loop of wire (gold) due to a time-changing magnetic field (red).	43
Figure 4.6: Magnetic field lines shown perpendicular (a) and parallel (b) to the cross-sectional area.	45
Figure 4.7: Output current as a function of the stator magnet height, or thickness. The current increases linearly with the height of the magnets.	47
Figure 4.8: Output voltage as a function of the cross-sectional area of the coil. Voltage is maximum when the cross-sectional area is minimum.	48

Figure 4.9: Power output of the device as a function of the cross-sectional area of the coil. Like the output voltage, output power is maximized when the coil cross-section is minimized.	49
Figure 5.1: Typical amplitudes and frequency ranges for various biomagnetic fields and reference fields. Field strength is in fT = 10^{-15} T [41].	52
Figure 5.2: Simple zinc/copper voltaic cell with 1.1V potential under standard conditions [43].....	53
Figure 5.3: Standard hydroelectric power plant model using an impulse turbine [46].....	55
Figure 5.4: Top view of original microfluidic channel design with winding microchannels.	56
Figure 5.5: Original generator design with horizontal stator shaft.	58
Figure 5.6: Gears used for original generator design with respective radii: Gear A - Turbine shaft gear, Gear B - Stator shaft gear.	58
Figure 5.7: Hinged designs for the stator shaft (a) with stator gears (b) and back plate components (c and d).....	59
Figure 5.8: Side view of the flat-coil design illustrating the horizontal stator with magnetized nickel suspended above a gold coil.	60
Figure 5.9: Bottom view of gold induction coil with partial nitride layer (grey) shown where the wires cross (a) and stator arms with nickel (purple) (b) in the flat-coil design.	61
Figure 6.1: Completed fabrication steps showing the turbine etch (a), the primary shaft etch (b), and the secondary shaft etch (c).	69
Figure 6.2: Fabrication steps necessary to encapsulate and release the fabricated turbine and shaft.	70
Figure 6.3: Slide pattern after ashing. Dried 1813 photoresist can be seen through the slide.	73
Figure 6.4: 0.25 μ m thick gold coil trace with excess gold remaining between the trace and the small alignment marks.	74
Figure 6.5: 1.0 μ m thick coil trace with good resolution. Outline is sharp and free of excess gold.	74

Figure 6.6: Profilometer measurement showing the profile of a 0.25 μm center coil trace through the window opened in the Si_3N_4 .	75
Figure 6.7: Profilometer measurement of the main and center coil traces leading to the probe pads of a coil on slide #12. Target coil thickness was 0.5 μm .	76
Figure 6.8: Nickel electroplating bath setup [52].	78
Figure 6.9: First nickel electroplating test wafer five days after electroplating. Dot on the left side of the wafer was the location of the Kapton dot and shows the copper seed layer. Circled areas show sites of initial delamination.	79
Figure 6.10: Second nickel electroplating test three days after electroplating. Slow cooling of the nickel from 50 $^{\circ}\text{C}$ caused more severe delamination.	80
Figure 7.1: Potential thinning sidewalls created as a result of metal deposition method.	83
Figure 7.2: Center coil trace damaged by probe contact during resistance measurements.	85
Figure 7.3: Fully fabricated coil with gold traces shown in yellow and nitride in orange.	86
Figure 7.4: Second attempt at nickel electroplating. Tensile strain caused the nickel delamination to remove sections of substrate up to 30 μm deep.	90
Figure 7.5: Profilometer measurement of second electroplating test wafer after cooling. Ni layer was 8 μm thick, seed layers comprised 0.1 μm in thickness. Red dashed line indicates original surface of the silicon substrate.	90
Figure 7.6: Magnetization (a) of the electroplated nickel and magnetic attraction (b) lifting the substrate.	91
Figure 8.1: Potential design of microturbine with w-shaped buckets before release (a) and after release (b).	96
Figure A.1: Mathematica code used to determine the flow rate of blood through human capillaries.	99
Figure A.2: Mathematica code used to determine the pressure at the opening to the turbine cavity in the ideal MFPG device using blood as the fluid.	100
Figure A.3: Mathematica code and graph illustrating the relation between capillary length and outlet pressure. Note that for blood flowing through a capillary with a 5 μm radius and an initial pressure of 5332.9 N-m, the cut-off length is 800	

μm . Beyond this length, adhesive and cohesive forces within the blood will counteract the initial pressure and the blood will not flow.....	101
Figure A.4: Mathematica code used to calculate the rate of water flowing through the microchannels of the fabricated MFPG device. The pressure at the inlet is matched to human capillary arteriole pressure and the outlet pressure is matched to that calculated for the ideal MFPG device.....	102
Figure A.5: Mathematica code and graph used to illustrate the rate of water flow through the fabricated MFPG microchannels as a function of capillary height.	103
Figure A.6: Mathematica code and graph used to illustrate the rate of water flow through the fabricated MFPG microchannels as a function of capillary length.	104
Figure A.7: Mathematica code used to calculate the torque applied to the turbine, by the fluid pressure at the opening to the turbine cavity, in the fabricated MFPG device.....	105
Figure A.8: Mathematica code used to calculate the angular velocity of the turbine in the fabricated MFPG device as a function of the ideal fluid flow rate.....	106
Figure A.9: Mathematica code used to calculate the rate of work done on the turbine by the fluid in the fabricated MFPG device.....	107
Figure A.10: Mathematic code used to calculate the magnetic field strength produced by the stator arms on the coil. Note that the magnetic field strength was calculated for stator magnet height of $20\mu\text{m}$	108
Figure A.11: Mathematic code used to calculate the maximum theoretical current that can be produced by the MFPG device. This was calculated for stator magnet height of $20\mu\text{m}$ and coil height of $2\mu\text{m}$	109
Figure A.12: Mathematica code used to calculate the voltage and maximum theoretical power output from this design. Again this is calculated for stator magnet height of $20\mu\text{m}$ and coil height of $2\mu\text{m}$	110
Figure A.13: Mathematica code used to calculate the magnetic field strength of the stator magnets with respect to the height of the coil. Note this calculation is for a magnet height of $20\mu\text{m}$. The field strength would be 512 Teslas for a magnet height of $80\mu\text{m}$	111
Figure A.14: Mathematica code used to calculate the total output current as a function of the magnet height. Note the output current for the device when the magnets are $80\mu\text{m}$ in height is just over $27\mu\text{A}$	112

Figure A.15: Mathematica code used to calculate the total output current as a function of the magnets height and width. Both are changing at the same rate to keep a square cross-sectional area. The output current for the device when the magnets are 80 μm in height is approximately 27.16 μA	113
Figure A.16: Mathematica code used to calculate the voltage output of the device as a function of the coil's cross-sectional area. The voltage is maximum when the coil is thinnest, for a value of 12.24 mV when the coil's cross-section is $2.5 \cdot 10^{-12} \text{ m}^2$	114
Figure A.17: Mathematica code used to calculate the theoretical maximum power output of this device as a function of the coil's cross-sectional area. The curve follows the same shape as the voltage curve and again is maximized when the cross-sectional area is minimum. The maximum theoretical power output from this calculation is 0.3325 μW when the stator magnets are 80 μm high and the cross-sectional area of the coil is $2.5 \cdot 10^{-12} \text{ m}^2$	115
Figure A.18: Mathematica code used to calculate the theoretical resistance for the 0.25, 0.5 and 1.0 μm thick center coil traces using the average fabricated dimensions for each group.....	116
Figure A.19: Mathematica code used to calculate the theoretical resistance for the complete 0.25, 0.5 and 1.0 μm thick coil traces using the average fabricated dimensions of each group.	117
Figure A.20: Mathematica code used to calculate the theoretical resistance of the 200 Å thick titanium seed layer between the two gold traces. Each section of titanium between the two layers of gold has an area of 100 μm^2	118
Figure B.1: L-edit layout showing all layers of the MFPG device.....	119
Figure B.2: L-edit layout for the top of first glass slide.....	120
Figure B.3: L-edit layout for the bottom of the first glass slide.	120
Figure B.4: Enlarged image of features on bottom of the first glass slide.....	121
Figure B.5: L-edit layout of first etch design for top of second glass slide.....	121
Figure B.6: Enlarged image of features on the first etch design for the top of the second glass slide.....	122
Figure B.7: L-edit layout of second etch design for top of second glass slide.	122
Figure B.8: Enlarged image of features on the second etch design for the top of the second glass slide.....	123

Figure B.9: L-edit layout of third etch design for top of second glass slide.....	123
Figure B.10: Enlarged image of features on the third etch design for the top of the second glass slide.....	124
Figure B.11: L-edit layout of first etch design for the bottom of the second glass slide.....	124
Figure B.12: Enlarged image of features on the first etch design for the bottom of the second glass slide.....	125
Figure B.13: L-edit layout of second etch design for the bottom of the second glass slide.....	125
Figure B.14: Enlarged image of features on the second etch design for the bottom of the second glass slide.....	126
Figure B.15: L-edit layout of first deposition design for the top of the third glass slide.....	126
Figure B.16: Enlarged image of features on the first deposition design for the top of the third glass slide.	127
Figure B.17: L-edit layout of second deposition design for the top of the third glass slide.....	127
Figure B.18: Enlarged image of features of the second deposition design for the top of the third glass slide.	128
Figure B.19: 2X-enlarged image of features of the second deposition design for the top of the third glass slide.	128
Figure B.20: L-edit layout of third deposition design for the top of the third glass slide.....	129
Figure B.21: Enlarged image of features of the third deposition design for the top of the third glass slide.	129
Figure B.22: L-edit layout of stator arms with alignment marks and non-etch buffer. ..	130
Figure B.23: Enlarged image of stator center showing shaft opening with groves.	130
Figure B.24: L-edit layout of stator magnets with alignment marks.	131
Figure B.25: L-edit layout of stator magnets (red) superimposed on stator arms (gold) with alignment marks and non-etch buffer.....	131
Figure B.26: L-edit layout of the turbine wheel with non-etch buffer.....	132

Figure B.27: L-edit layout of primary turbine shaft design.	132
Figure B.28: L-edit layout of secondary turbine shaft design.	133
Figure C.1: Recipe used to deposit Cr/Cu seed layer for nickel electroplating.	137
Figure C.2: Recipe used for first two nickel electroplating attempts.	138
Figure D.1: Current vs. voltage plot for all five coils on slide #2 with an averaged plot line.	142
Figure D.2: Current vs. voltage plot for the remaining four coils on slide #3 with an averaged plot line.	143
Figure D.3: Current vs. voltage plot for the remaining two coils on slide #4 with an averaged plot line.	144
Figure D.4: Current vs. voltage plot for the one remaining coil on slide #12.	145
Figure D.5: Current vs. voltage plot for the remaining four coils on slide #5 with an averaged plot line.	146
Figure D.6: Current vs. voltage plot for the remaining three coils on slide #6 with an averaged plot line.	147

List of Tables

Table 2.1: Equations governing fluid flow through a channel [16].	16
Table 3.1: Transducer categories and examples [24].	31
Table 4.1: Critical design elements and dimensions for the Ideal and Fabricated designs.	35
Table 4.2: Parameters used to calculate the flow rate of blood in human capillaries.	36
Table 4.3: Parameters used to calculate the pressure at the opening to the ideal turbine chamber.	37
Table 4.4: Values used to calculate pressure at the fabricated turbine chamber opening.	37
Table 5.1: Magnetic properties of ferromagnetic materials [43].	64
Table 5.2: Resistivity values for common materials at 0 °C [24].	65
Table 6.1: Chemical composition of standard Nickel electroplating bath [53].	81
Table 7.1: Average thickness and width of the center coil traces after fabrication.	83
Table 7.2: Average thickness and width of the main coil traces after fabrication.	84
Table 7.3: Calculated and measured resistance of the center coil trace for each of the three thicknesses.	85
Table 7.4: Calculated and measured resistance of the full coil trace for each of the three thicknesses.	87
Table 7.5: Cross-sectional area and resistance values for the coils on slide #5.	88
Table C.1: Recipe used for patterning of metal deposition with SF-11 and AZ5214E photoresist.	134
Table C.2: Recipe used for patterning Silicon Nitride and Borosilicate Glass (Silicon Dioxide) with 1813 photoresist.	136
Table D.1: Measured height and width of the 1.0 μm center traces.	139
Table D.2: Measured height and width of the 0.25 μm center traces.	139
Table D.3: Measured height and width of the 0.5 μm center traces.	140

Table D.4: Measured height and width of the 1.0 μm main traces.....	140
Table D.5: Measured height and width of the 0.25 μm center traces.	141
Table D.6: Measured height and width of the 0.5 μm center traces.	141
Table D.7: Voltage versus current measurements for Slide #2 (1 μm trace thickness)..	142
Table D.8: Voltage versus current measurements for Slide #3 (1 μm trace thickness)..	143
Table D.9: Voltage versus current measurements for Slide #4 (1 μm trace thickness)..	144
Table D.10: Voltage versus current measurements for Slide #12 (0.5 μm trace thickness).	145
Table D.11: Voltage versus current measurements for Slide #5 (0.25 μm trace thickness).	146
Table D.12: Voltage versus current measurements for Slide #6 (0.25 μm trace thickness).	147

Foreword

Technology is neither inherently good nor evil; rather, it is the intent with which it is used that often causes us to view it as one or the other. This project was undertaken in the hopes that research derived from it may one day help to improve the quality of life for all mankind and the optimistic hope that it will never be used with malice.

Aaron J. Sprecher
March 2008

*nam beneficium omnis populus
ad astra per aspera*

MICROFLUIDIC POWER GENERATION

I. Introduction to BioMEMS

1.1. The Need for Microfluidic Power Generation

The biomedical field currently has a need for self-sufficient, implantable devices to monitor and correct biological disorders such as heart attacks, strokes, diabetes, high blood pressure, etc [1]. Many of the devices that are currently used for these purposes are run on batteries, requiring major surgery every five to ten years to replace the battery, or are external, requiring frequent visits to doctors or constant blood samples, as with the diabetic testing kit shown in Figure 1.1.



Figure 1.1: Standard Diabetic Glucose Monitoring Equipment including diagnostic meter, lancet for piercing skin and test strip for collecting blood and transporting it to the diagnostic meter [2]

1.2. Microelectromechanical Systems (MEMS)

The field of MEMS is often compared to integrated circuits (IC) because they use many of the same manufacturing techniques. This comparison is misleading, however, because ICs are used primarily to manipulate electronic and some photonic signals. MEMS devices, on the other hand, are an interface between the physical world and the electronic world on a microscopic scale [3]. As such, they must operate in a much wider and more diverse environment.

MEMS devices can be created through several methods. The most common method involves alternating steps of depositing and removing layers in a given pattern. Incredibly complex devices can be made through the MEMS process, including rotating wing microflying devices, internal combustion engines, and electrical motors, all smaller than a penny.

MEMS encompasses a vast breadth and diversity of technology. The acronym describes a large selection of micromachined sensors and actuators that span many disciplines including: electrical engineering, mechanical engineering, IC processing, circuit design, materials science, chemistry, instrumentation, fluidic engineering, optics and packaging. Because of the complex nature of these devices, they also have a diverse range of utility. Today, MEMS devices are used in optical fiber switching, microfluid control, micromechanical electrical relays, biosensors, forensic analysis, digital video projectors, inkjet printing cartridges, and many other everyday items.

1.2.1. BioMEMS

The first decade of the 21st century has seen rapid blending between the fields of biomedicine, microdevices, and informatics that has led to the formation of a new field of research known as BioMEMS. It encompasses biochemistry, microfabrication, microfluidics, micromechanics, biophysics, protein engineering, cell physiology and computational power to create self-contained systems that can be used as a complete biological laboratory-on-a-chip, an artificial organ, or implantable biosensors [4]. Examples of such advances include the AbioCor implantable replacement heart (Figure 1.2), Learning Retinal Implant (Figure 1.3), and BrainGate (Figure 1.4) [5].



Figure 1.2: The AbioCor implantable replacement heart uses an implanted electronics package to monitor and control pumping speed of the heart based on the physiological needs of the patient [5].



Figure 1.3: The Learning Retinal Implant from Intelligent Medical Systems. It is designed to help patients with retinitis pigmentosa. The eye glasses and photoprocessor worn on the waist are used to train the retinal implant, thus restoring vision [5].

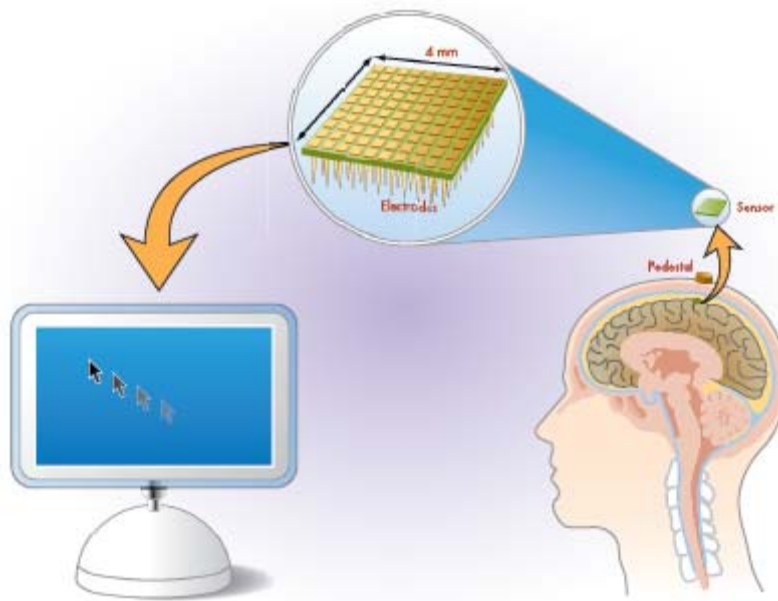


Figure 1.4: Braingate neural implant devised by Brown University. The implantable chip will enable the mind to manipulate electronic devices and may lead to restored mobility in paralyzed patients [5].

1.2.2. Microfluidics

The field of microfluidics involves the handling and manipulation of minute amounts of fluid, usually on the order of micro-liters to pico-liters and lies on the boundary between biotechnology, medicine, chemistry and MEMS [6]. It has been beneficial for cell characterization, leading to increased sensitivity for cancer screenings and increased efficiency for drug discoveries [1].

1.3. Problem Overview: Limitations in MEMS and Microfluidics

As MEMS is a relatively young field of research, there are still many aspects of fabrication and device performance that are not well understood. Device designs are often used because they function, even though it is not fully understood why they behave as they do. Many of the properties of the materials used in the fabrication process are likewise not fully understood because of the shift in material behavior from macro-size samples to micro-size samples. Documentation on the electromagnetic properties of sub-micrometer volumes of ferromagnetic materials, for example, is essentially non-existent.

Microfluidics also has its limitations. While this area of research is better understood, it still has physical restrictions. Due to the nature of fluidics, there are limits as to how small the channels can be before a fluid will not be able to flow.

Since this project incorporates both MEMS and microfluidics, it will require multiple trial configurations in order to collect sufficient data to extrapolate an efficient design. The questions then to be answered are: a) how can the nickel be magnetized once it is deposited, b) what volume of nickel will be sufficient to maintain a stable magnetic

field, c) what is the tolerance for distance between the nickel and the current loop, and finally, d) what coil dimensions will allow adequate current flow while preventing overheating and burnout of the coil.

1.4. Intent of Research

Given the current state of MEMS technology and microfluidics, a self-sufficient device could be constructed to monitor all aspects of human blood from inside the body and then relay the information to an external device for monitoring. Such a device would require six different components: a non-reactive housing, microfluidic channels for the blood to flow through, probes in the microchannels to monitor blood composition, microprocessors to process data from the probes, an external communications link, and finally a method to produce its own power.

With the exception of power generation, all of these components currently exist or are being rigorously researched. Many different materials, such as glass or polyimides, are currently used in the fabrication and structures of MEMS devices and will not cause an adverse reaction if implanted into the human body [7]. The housing for the device, as well as the microchannels, would be made of such a material. The openings of the channels would be coated with a protein that controls angiogenesis [8], or the formation of blood vessels (Figure 1.5). When implanted, the body would react to the protein by growing capillaries to the two openings of the device, thus providing the necessary blood flow through the device.

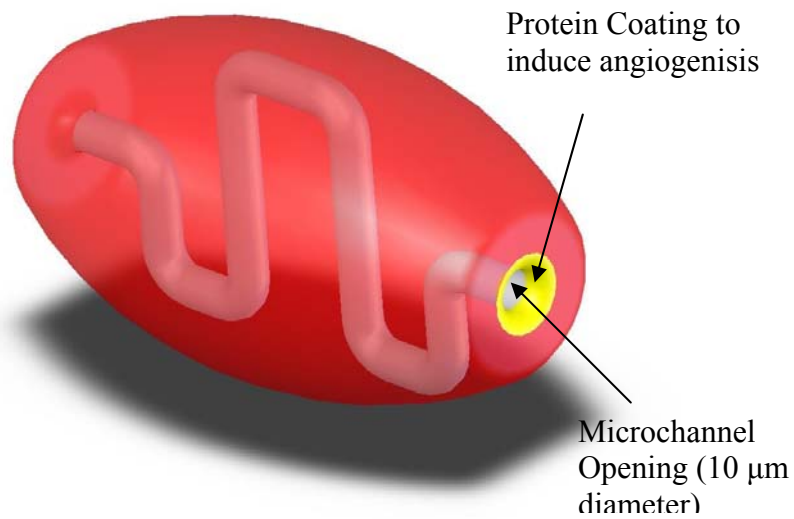


Figure 1.5: Theoretical image of the completed MicroFluidic Power Generation (MFPG) device showing the outer shape, the microchannel, and the protein coating at the opening of the microchannel. The turbine, generator and microchannel probes are not shown.

The composition of the blood would be detected by measuring the resistance between sets of protein-coated probes positioned in the microchannels. Each set of probes would be used to monitor different elements in the blood, i.e. – glucose, oxygen, white blood cells, etc, depending on the coating. The probes would need to be spaced appropriately so that there is no interaction between adjacent probes. Such probes are currently being used in a new generation of glucose monitors, requiring a significantly reduced blood sample size and an increase in accuracy [9].

Once blood is flowing through the device, the probes will measure the composition of the blood and send the raw data to microprocessors. The number of probe pairs in the channel and the required sampling rate will determine the number of microprocessors needed to format the data and send it to the external communications link for transmission to an external monitoring device. Such microprocessor arrays with

radio frequency (RF) links are currently being researched for wireless implantable neural probes [10].

1.4.1. Proposed Solution and Research Objectives

This project was undertaken to determine the feasibility of using well established electromagnetic power generation techniques to harness energy from the human body.

As such, the objectives of this portion of the project are to

1. Determine if it is theoretically possible to harness energy in this manor
2. Design a method for electromagnetic power generation using a microfluid flow as the external energy source
3. Begin testing fabrication methods
4. Characterize any portions of the device that are fabricated

1.4.2. End Goal of Microfluidic Power Generation Project

The power generation system that is the core of this research is not meant to be a stand-alone device. Rather, it is meant to be one module within a larger device. Like the mitochondria within a living cell, it is meant to be the powerhouse that allows all other parts to perform the necessary operations. Once fabrication methods have been perfected for this power system, it must be integrated with other components to produce a self-sufficient module that will improve the quality of life for any who have need of it, whether they are patients in a hospital, soldiers on the battlefield, or astronauts walking through the void of space.

1.4.3. Design Requirements

There are no concrete design requirements (i.e.- specific voltage or current levels) as this is a novel project. The requirement, rather is to determine if this is a feasible method for generating sufficient power to allow a BioMEMS system to operate self-sufficiently.

1.5. Organization of Thesis

This thesis is divided into eight chapters with four appendices. Chapter one details the need for this project, a basic definition of MEMS and microfluidics, a review of the potential problems that may be encountered, and the intent of the research. Chapter two contains a brief history of medicine, microfluidics, and electromagnetism, a brief overview regarding energy harvesting on a MEMS scale, and a review of theoretical and fabricated designs that are similar to that proposed for this project. Chapter three is a review of the theory behind fluid mechanics, both on the macro and micro scale, and electromagnetic theory. Chapter four contains information on the models used to design these devices and the calculations necessary for the models. Chapter five contains details on the device designs. Chapter six contains details on the methods of fabrication. Chapter seven details the analysis and results of experiments. Finally, Chapter eight discusses conclusions from the results and recommendations for future research.

Of the four appendices: Appendix A contains Mathematica code used to calculate flow rates, pressure, rates of rotation, magnetic field strength, and coil resistances; Appendix B contains design images; Appendix C contains the recipes used for the device fabrication; and Appendix D contains tables listing experimental data.

II. Literature Review

2.1. Chapter Overview

Technology has always played a part in medicine, but only recently has medicine played a part in technology. The birth of the biomedical engineering field in the 1940s, heralded a shift from unmanaged, often crude single-problem technology solutions to organized research into future biomedical technology solutions. This chapter illuminates the need for an MFPG system, its relevance in current medicine, and similar research that has already been completed and its relevance to this project.

2.1.1. Historical Perspective

“Medicine is a science from which one learns the states of the human body with respect to what is healthy and what is not, in order to preserve good health when it exists and restore it when it is lacking.”

Abū Alī ibn Sīnā, the opening to the *Al-qanun fi al-tibb*

Since before recorded history, mankind has looked for ways to help those who are injured or infirm. The first forms of help were often crude and made from readily available local materials. Orchid bulbs were a common remedy for stomach problems while cuts and sores were usually smeared with animal fat and bandaged with animal skins. Broken limbs would be crudely set and then covered in river clay, which would harden to form a crude cast to protect the bone as it healed [11].

Since then, the level and complexity of help that can be given has increased immensely. From the foundations laid by the Greeks and the Arabs, studying human

anatomy, as shown by Figure 2.1, and the establishment of the first true hospitals, mankind has compiled a vast knowledge of human ailments and cures [12].

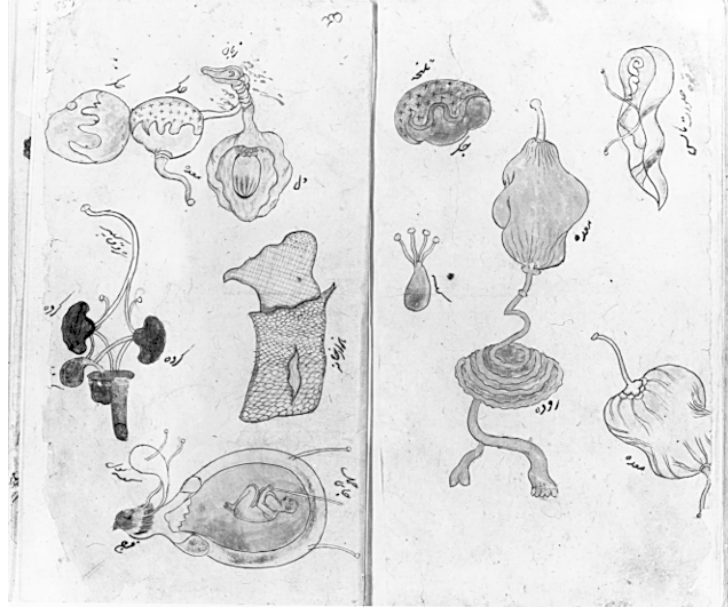


Figure 2.1: Individual organs drawn in inks and opaque watercolors from an 18th century Persian translation of an Arabic medical compendium [12].

The last century has seen the greatest advances in medicine, culminating in today's prosthetic limbs, complex surgeries, and intricate knowledge of medicinal affects on the human body. This knowledge and ability has greatly improved the average lifespan and the quality of life for millions of people.

2.1.2. Potential Microfluidic Power Generation Applications

Many of today's "cures," however, are still invasive and discomforting, often requiring the use of scalpels and needles. As of the 2005 census, an estimated 20.8 million people in the United States, or 7.0% of the population, live with diabetes [13]. Those that are diagnosed with the disease are required to prick their finger several times

per day to monitor their blood-glucose level. Once the finger has been pricked, the patient applies the blood to a test strip, and only then can the blood be analyzed for protein levels.

Other cures often require the placement of bulky electrical devices, such as pacemakers like the one shown in Figure 2.2, inside the body to regulate heart or nerve functions. These devices are typically run on batteries, which must be periodically replaced, requiring major surgery each time.

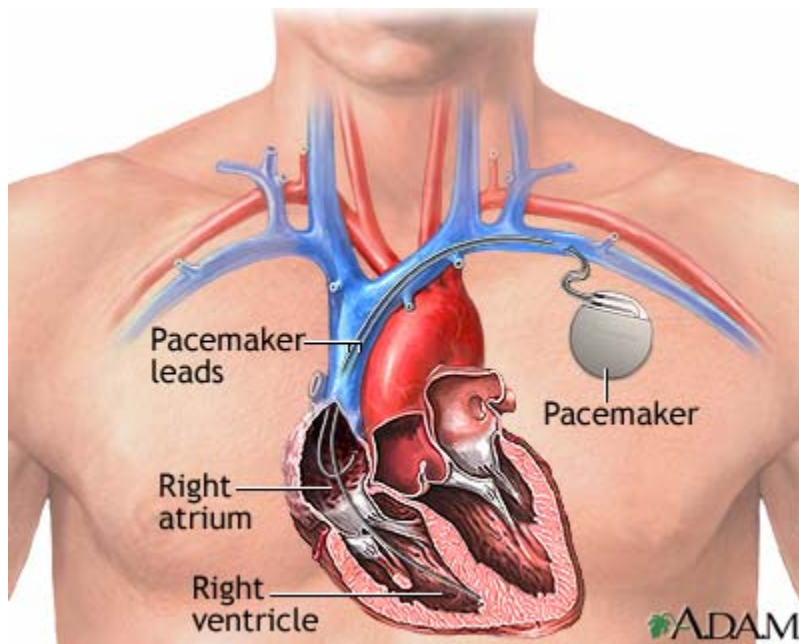


Figure 2.2: Implanted pacemaker used to regulate electrical activity in the heart [14]

The MFPG system would alleviate many of these necessities. By generating power in an array of self-contained units within the body, many opportunities arise. The MFPG systems could be combined with current blood analysis tools to create a self-contained blood analysis lab like the one shown in Figure 2.3 that would use the flow of blood through the device to power its array of probes. These probes could be used for real-time

monitoring of proteins, molecules and foreign bodies in the bloodstream. Pacemakers could be replaced by much smaller units, which do not require replaceable batteries. They would instead be linked to an array of MFPGs, which could be used to charge the pacemaker's capacitors. MFPGs coupled with RF components could also be used to link severed nerve endings, converting biochemical signals into RF and back, returning mobility and sensory capability to patients with spinal cord damage. This ability could also be used to control prosthetic appendages, while increasing the manual dexterity and sensory capabilities.

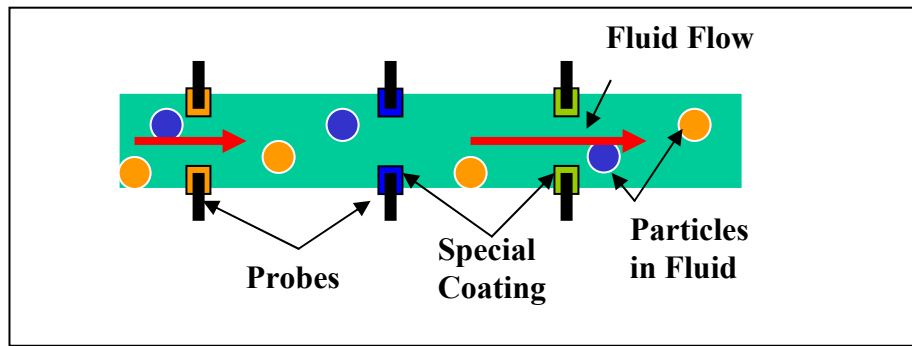


Figure 2.3: Graphical representation of a microchannel with particulate fluid flow and analysis probes. Each probe pair is coated to identify a specific type of particle.

2.2. Microfluidics: A Drop in the Bucket

Research into microfluidics has been well documented since its inception at Stanford University in the 1990s. It was developed to study the composition of a sample that would normally have been analyzed in a chromatograph, like the one shown in Figure 2.4. Due to the relatively small size of the samples, however, the chromatograph was ineffective. The analysts needed a way to handle and study these small volumes of

liquid, and so, micro-fluidics was born. Shortly thereafter, IBM revolutionized the world of printers when it picked up microfluidics as a way to transfer ink to paper, giving rise to the inkjet printer.

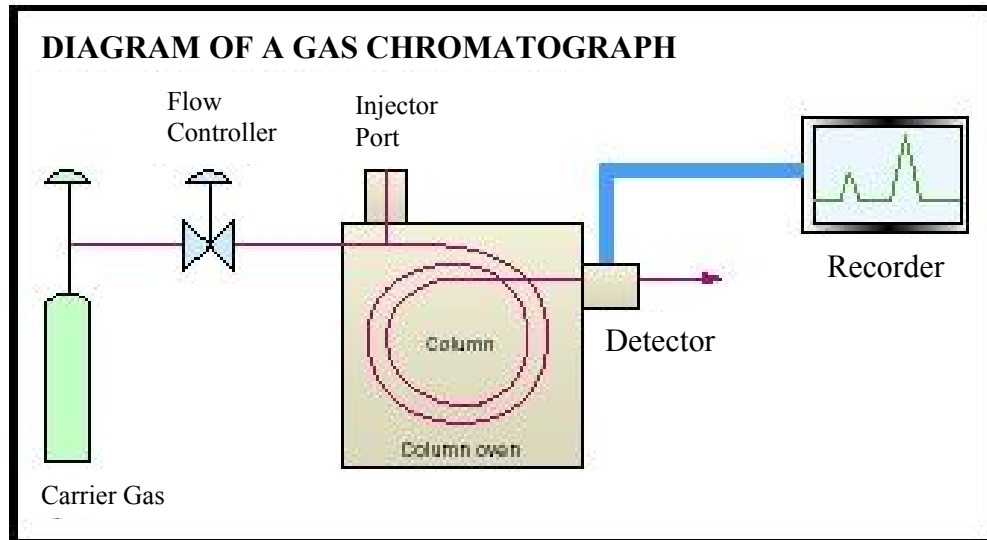


Figure 2.4: Diagram of a gas chromatograph used for sample analysis [15]. This method often made identification of small samples impossible.

Since that time, microfluidics has been incorporated into many fields, but the basic design for all microfluidic systems is essentially the same. They use non-reactive materials such as glass or polymers with microchannels ranging from a few micrometers in diameter up to a few millimeters. The methods for inputting and removing the fluids from the system vary from simple delivery and extraction by syringe or connections via tubing to external systems for the Lab-on-a-Chip, shown in Figure 2.5, to cohesion from a reservoir out to open air, in the case of an inkjet printer. There are also several common methods for moving the fluid through the microchannels, including simple pressure gradients, micro-turbines, and electro-osmotics. Some current applications for

microfluidics include inkjet printers, forensic analysis, genomics and proteomics, food and nutrition, pharmacology, and chemistry.

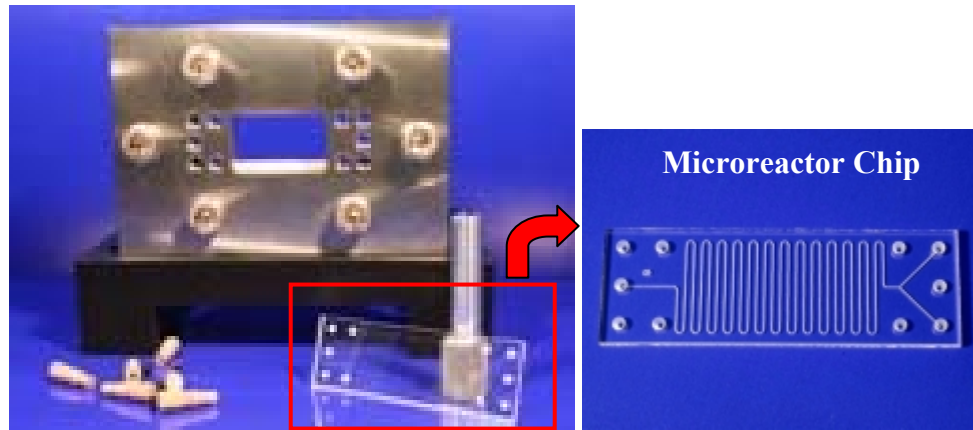


Figure 2.5: Micronit Lab-on-a-Chip microfluidic analysis tool shown with glass microreactor chip [6].

In common microfluidic applications, complications arise when trying to deal with very small channels, due to the physics that govern fluid flow through a channel. The first complication, low flow rate, arises from the nature of the fluid flowing in the channel [16]. Fluid flowing through a channel flows slower around the edges of the channel than it does in the center, as shown in Figure 2.6, due to its coefficient of viscosity (η). A fluid's coefficient of viscosity is a measure of its cohesive and adhesive nature or the degree to which it resists flow under an applied force. The higher a fluid's coefficient of viscosity, the more it resists flowing through the channel. The second complication, resistance to fluid flow, relates directly to the size of the channel through which the fluid is flowing. Table 2.1 shows that the equations for flow rate and resistance to fluid flow both depend heavily on channel size. The resistance to fluid flow

(R) is proportional to the square of the radius (r) of the channel and the fluid flow rate (F) is inversely proportional to r^4 . This means, as the channel becomes smaller, more force is required to push the fluid through the channel. These equations will be discussed in further detail in Section 4.2.1. Other variables in the equations include the channel length (L) and the change in fluid pressure from one end of the channel to the other (ΔP).

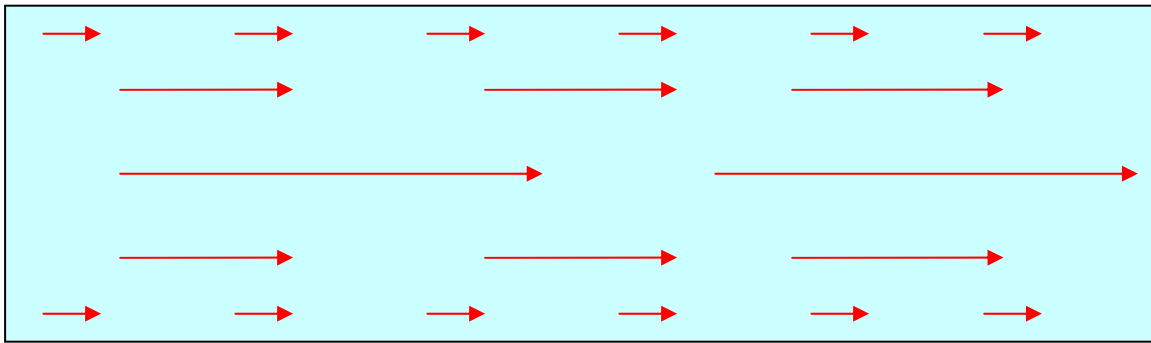


Figure 2.6: Effects of viscosity on fluid flow in a channel.

These complications should not arise in the proposed power generation unit, because the microchannels would be approximately 10 μm in diameter [17], the same size as a human capillary; thus the body would not be placed under any appreciable strain because there should be no increase in blood pressure required to push the blood through the device.

Table 2.1: Equations governing fluid flow through a channel [16]

Resistance to Fluid Flow	$R = \frac{(8 \eta L)}{\pi r^2}$
Flow Rate	$\Phi = \frac{\pi r^4 \Delta P}{(8 \eta L)}$

2.3. Turbines: Turning the Wheel of History

A turbomachine is defined as a device in which energy transfer occurs between a flowing fluid and a rotating element due to dynamic action, and results in a change in pressure and momentum of the fluid. Turbomachines can be used to either extract energy from or impart energy to a continuously moving stream of fluid. This broad definition covers a wide range of machines, such as gas turbines, steam turbines, centrifugal pumps, centrifugal and axial flow compressors, windmills, water wheels, and hydraulic turbines [18].

The term “turbine” was coined in 1828, by a French professor Claude Burdin, to describe the subject of an engineering competition for a water-based power source. The word comes from the Latin *turbo*, meaning a whirling or a vortex and is used to describe a machine in which water moves relative to the surfaces of the machine. This is separate from machines in which this motion is secondary, such as a piston or a cylinder [19]. Water turbines, or hydraulic turbines, are often used to drive electric generators in hydroelectric power stations. The first such station was built in Wisconsin in 1882 and soon became the first of many [20]. By 1920, about 40% of all electric power in the U.S. was derived from hydropower.

Hydraulic turbines can be separated into two basic design categories: axial-flow turbines and impulse turbines [21]. The primary difference between these designs is the direction of fluid flow relative to the axis of the turbine. In axial-flow turbines, the fluid flows parallel to the axis of the turbine, often completely covering a portion of the turbine, as shown in Figure 2.7a. The blades of the turbine can range from a simple

straight blade positioned at an angle of 45° relative to the fluid flow, to complex curved L-shaped geometries designed to more efficiently convert the energy of the fluid flow to turbine rotation.

Impulse turbines like the one shown in Figure 2.7b, on the other hand, use a fluid flow perpendicular to the axis of the turbine. A nozzle at the head of the fluid channel increases the pressure of the fluid before it impacts the blades of the turbine. Unlike the axial-flow turbine design, the fluid flow for an impulse turbine impacts only a single blade at a time. The fluid then falls in to a channel where it can pass out of the system. The blades of an impulse turbine are typically W-shaped, based on the design patented in 1880 by Lester A. Pelton.

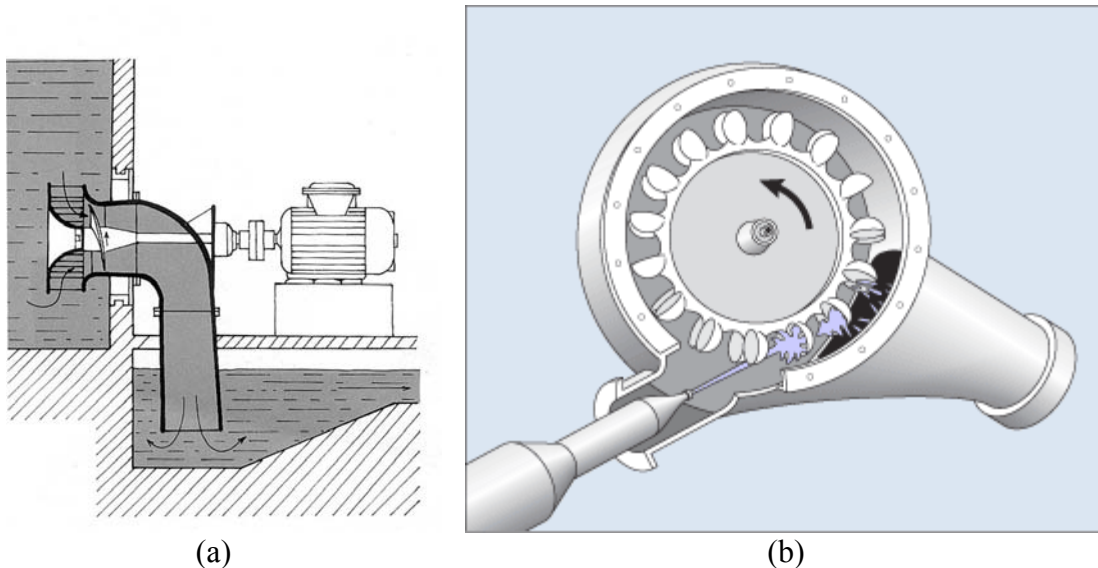


Figure 2.7: Cross-sectional views of an axial-flow turbine (a) [22] and an impulse turbine (b) [23]

Because of the particulate nature of blood, the fluid that the MFPG device should ultimately be utilized for, a modified version of the impulse turbine is the most likely design to be successful and least harmful. The blades of the MFPG turbine, however,

will not be W-shaped like the Pelton turbine because of the difficulties in fabricating curved surfaces on a micron scale.

2.4. Electromagnetism: The Interaction of Charged Particles

While the phenomenon of both electricity and magnetism were known to the Greeks of ancient time, neither one had any practical application at the time and were simply observed as curiosities [24]. The first true attempts to understand and harness electricity and magnetism did not start until the late 16th century, with the Englishman, William Gilbert. In 1600, he published *De Magnete*, one of the first scientific works on the phenomenon. Gilbert's pioneering research into electricity and magnetism became the foundation for our modern technological society.

The 18th century heralded numerous advances in our understanding of electricity and magnetism. There were three key advances during this time period that were critical to our modern understanding. The first was the model of static electricity. Two models were actually developed to explain the phenomenon of static electricity, the one-fluid model proposed by Benjamin Franklin, and the two-fluid model proposed by Charles DuFay. Franklin's model suggested that neutral matter possessed a certain amount of the electric fluid. He supposed that a positive charge was an excess of the fluid and a negative charge was a deficiency of the fluid. DuFay's model suggested that there were two different types of fluid; one positive, the other negative, and that neutral matter composed equal quantities of each. These models would stand until J. J. Thompson's discovery of the electron in 1897. The remaining two key advances were technological

in nature. One was the development of electrostatic devices, to create and store large amounts of static electricity. The second was the development of the voltaic pile shown in Figure 2.8. It was developed by Alessandro Volta in 1800 and is thought to be the earliest known form of battery. With these two advancements, mankind finally had the ability to harness electricity and use it when and where he wanted.

Since that time, our knowledge of electricity and magnetism has been greatly advanced. The development of Coulomb's Law (1785), the Unification theory by Oersted (1820), Ampere's Law regarding magnetic fields generated by electric current, and Faraday's discovery of electromagnetic induction in 1831, all led to the development of the Electromagnetic Field Theory and Maxwell's equations, which are the four key equations that are used today to model electromagnetic phenomenon.



Figure 2.8: Voltaic pile consisting of a series of alternating zinc and copper disks separated by cardboard soaked with an acid or salt solution [25]

While electromagnetic fields have been extensively studied for more than four centuries on the macro scale, their properties and behavior on the micro scale have only recently been studied. Documented experimentation with microscopic samples of ferromagnetic materials has, to date, been limited to altering the spin of electrons passing through the sample. This field of research is known as spintronics or spintronic devices. Its only relevance to this project, however, is to prove that ferromagnetic materials do exhibit the necessary magnetic polarization in samples significantly smaller than those used for this project.

2.5. MEMS Energy Harvesting: Energy from the Ether

Energy scavenging or harvesting is the collecting of energy from the environment to enable work. Mankind has been harvesting environmental energy since the first rock was rolled down a hill (i.e. – gravity), but we have only recently begun to actively examine electrical energy harvesting. There are four main categories of energy harvesting: electromagnetic, kinetic, photonic and thermal. All of the methods, such as solar, electromagnetic fields, thermal gradients, and fluid flow have all been successfully used to power electrical devices, though some more efficiently than others [26].

MEMS energy harvesting has already been demonstrated with a number of different devices; the majority of these devices, however, use piezoelectric materials to convert kinetic energy into electrical energy. Of the other forms of energy harvesting, solar and thermal energy harvesting on the MEMS scale is impractical, due to size restrictions. Fluid flow has been used to generate electrical energy by several methods,

which will be discussed in the next section. Finally, electromagnetic energy harvesting on the MEMS scale has not been widely examined due to the lack of understanding of magnetic field behavior on the micron scale.

2.6. Relevant Research

2.6.1. Similar Designs

In 2003, researchers at the Imperial College in London successfully fabricated and tested an axial-flow turbine for airflow sensing (Figure 2.9) [27]. The turbine was created using UV lithography, Deep Reactive Ion Etching (DRIE), laser etching and electroplating. The prototype device was 18x18x9 mm and could produce an average power of 1.1 mW [28]. This was only 1% of the power predicted by the models. The power loss was most likely due to bearing loss and windage.

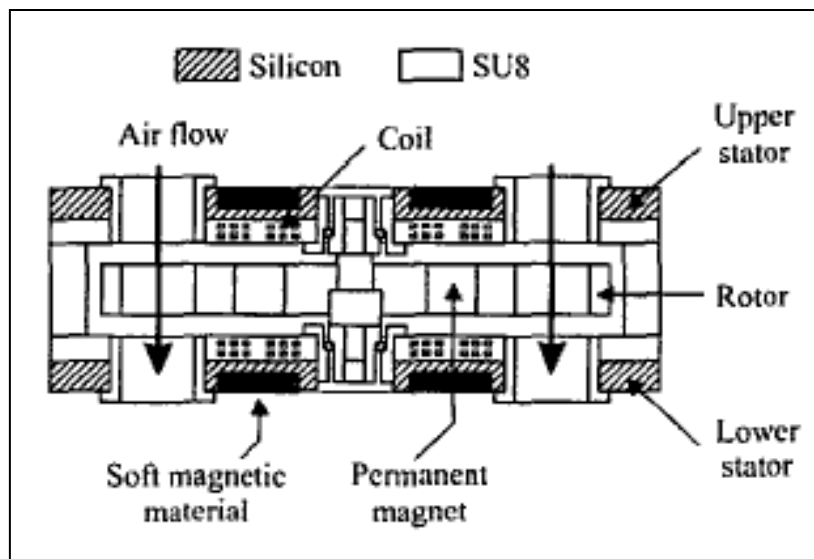


Figure 2.9: Cross-section of Micro-engineered turbo-generator based on an axial-flow turbine. The generator uses permanent magnets (magnetite), which are inserted after the rotor is fabricated [27].

While the axial-flow turbine design shares the same fundamental power generation principles as the design for this project, there are several glaring differences, the primary difference being size. The axial-flow turbine design is three orders-of-magnitude larger than the MFPG design. The second difference is the direction of flow through the turbine. The airflow for the axial-flow turbine is parallel to the axis of the turbine. The MFPG design has the fluid flow perpendicular to the axis of rotation to prevent any fluid from entering the stator cavity. Finally the magnetic components in the axial-flow turbine design were permanent magnets that were manually inserted into the stator after fabrication. Those of the MFPG design will be ferromagnetic nickel that will be magnetized after the device is assembled.

2.6.2. Microfluidic Power Generation

Several methods have been studied for producing power using fluidics on a small scale. In 2000, MIT developed a model of a Micro Hydraulic Transducer that could be used to either induce a fluid flow or generate power from a fluid flow using piezoelectric material [29]. The power generation potential for this device was found by computer simulation to be roughly 1 kW/kg with a flow rate around 1.5 ml/s at 40% efficiency. Like the axial-flow turbine described above, however, the primary drawback again is the device's size. At 20x10x5 mm, it is too large to be used with blood flowing through capillaries. Also, the device was not fabricated, so the actual power generating potential may be significantly less than the simulated levels.

Another method of generating power on a MEMS scale was researched in 2004 by researchers at the University of Alberta, Canada [30]. They forced water through a

ceramic rod, taking advantage of the charge separation phenomenon near the solid-liquid interface in microchannels, shown in Figure 2.10. This is a naturally occurring phenomenon, which can be increased or decreased depending on the composition of the fluid and the solid. This method requires a large number of microchannels and cannot be used to power a device directly. It must be used to charge capacitors which will power the device. Also, this method is only about 0.8% efficient and the resulting charge separation, which generates the power, may cause negative effects on blood.

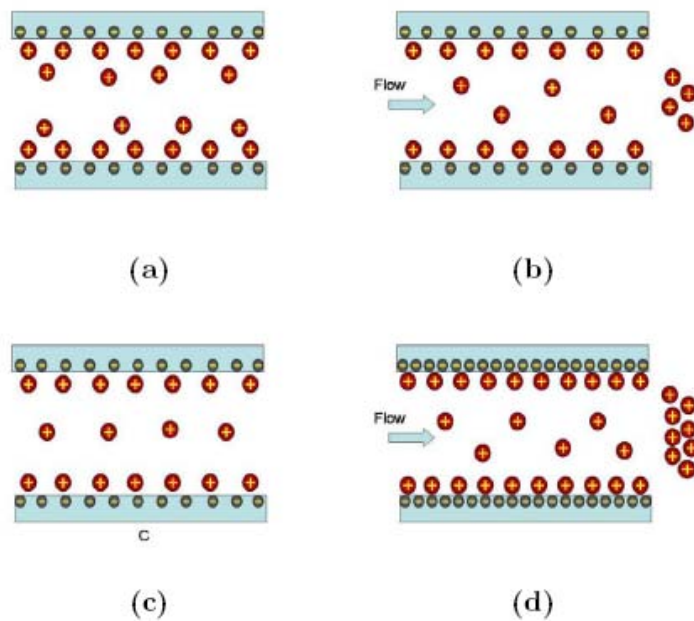


Figure 2.10: A schematic of the mobile-ion-drain method. (a) Surface has adopted a charge when in contact with water and electron double layer forms; (b) A stable streaming potential exists due to the water flow and accumulation of mobile ions; (c) The mobile ions in (b) have drained and the surface will disassociate and become negatively charged; (d) The surface has become more negatively charged when flow resumes, resulting in a larger streaming potential.

2.7. Chapter Summary

Although the field of microfluidics is well understood, very little research has been done into applications of microfluidics with the intent of generating power. Those that have been done are not relevant to this project due to their size or methodology. Also, the electromagnetic portion of this project represents an unknown quantity. It remains to be seen, whether sufficient current can be generated using this method, on this scale.

III. Theory

3.1. Chapter Overview

A scientific theory is defined as an explanation of a set of related phenomena or observations based upon proven hypotheses and independently verified numerous times by other groups of researchers [31]. Scientific theories are accepted to be true by the whole of the scientific community and are used to predict the outcome of future events or experiments. The purpose of this chapter is to review the theory of fluid dynamics, microfluidic flow and transduction, or energy transfer. It will examine the difference between turbulent and laminar fluid flows and how fluid will flow on the micron scale. It will also review the basic operating principles behind a mechanically driven electromagnetic generator.

3.2. Fluid Dynamics

Of the four states of matter, solid, liquid, gas, and plasma, liquid is perhaps the most dynamic. A liquid can change directly to any of the other three states with a relatively small amount of energy and carries the properties of all three. It can have the physical strength of a solid, can become electrically charged, and can conform to the shape of any container that it is placed into.

There are three main forces that govern the movement of a fluid: adhesion, cohesion, and pressure. Adhesion is a molecule's attraction to molecules of other materials. It is the force responsible for holding a drop of rain to a hanging leaf or that last drop of soda that will not come out of the bottle. Cohesion, on the other hand, is the

attractive force between atoms of the same material. This is what causes liquids to form droplets and rivulets. These two forces govern how a liquid interacts with other matter, but it is pressure that governs why a liquid interacts with other matter. Pressure is measured in force per unit area, with the area being defined by the surrounding solid material. The force, acting in a direction perpendicular to the surface of the liquid, can be due to gravity or can be mechanically induced by a pump. A water pump, for instance, creates a positive pressure in a pipe, forcing water away from it, where a vacuum cleaner creates a negative pressure, pulling air towards it.

These three forces can be of great benefit to parents, often entertaining children for hours. By placing a straw in a glass of liquid, placing a finger over the upper opening and lifting the straw out of the liquid, one can demonstrate adhesion, cohesion, and pressure. When the straw is initially placed into the glass, the pressure of the liquid will force it into the straw. When the straw is lifted out of the liquid, the finger covering the upper opening traps the air in the upper part of the straw. The liquid molecules closest to the sides of the straw will adhere to the sidewalls and the remaining liquid molecules will cohere to those liquid molecules that adhered to the straw. As the water attempts to yield to the force of gravity and drop out of the straw, it pulls on the air trapped at the top of the straw. This creates negative pressure in the air pocket and combined with the cohesive and adhesive forces in the liquid, is sufficient to overcome the force of gravity and keep the liquid suspended in the straw.

3.2.1. Turbulent vs. Laminar Flow

Viscosity is a fluid property which relates applied stress to the resulting strain [32]. Simply put, it is a measure of how the adhesive and cohesive forces, described above, interact as a fluid is deformed. Combined with the environment in which the fluid flows, viscosity governs how the fluid flows. There are two basic types of fluid flow: turbulent and laminar flow.

Turbulent flow, as illustrated in Figure 3.1, describes complex, fluctuating, disorderly motion within the fluid as it flows. This can be caused by variations in the walls of the material through which the fluid flows, particulates in the fluid flow, temperature and pressure changes, and many other factors. Turbulent fluid flow is difficult to predict and model due to its complex nature and each solution must be tailored to the specific circumstances of that particular fluid flow. Laminar flow, on the other hand, is much simpler.

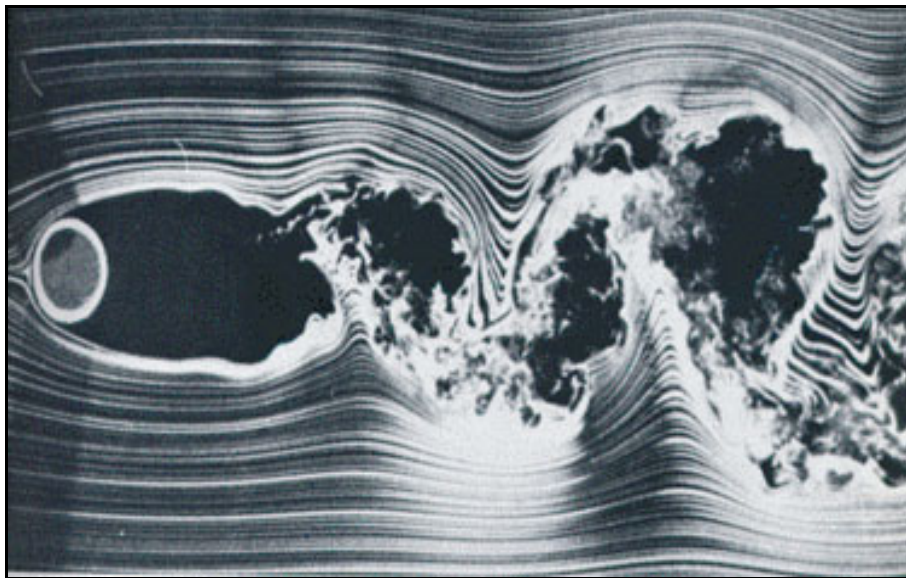


Figure 3.1: Turbulent fluid flow due to an object in the path of the flow [33]

Laminar flow is named for the flow layers that form within the fluid. It is more common when the flow channel is relatively small, the fluid is moving slowly, and its viscosity is relatively high [34]. Laminar flow is the type of flow in which the fluid travels smoothly or in regular paths parallel to the direction of the flow, as shown in Figure 3.2. Laminar flow within a pipe can be considered as the relative motion of concentric circles. The only difference between the circles is their velocity. The circle closest to the sidewall of the pipe is essentially fixed because of its adhesive properties, with a velocity of zero. The circle immediately inside the outer circle has a low velocity, sliding over the outer circle slowly due to cohesion. This continues into the center of the pipe, where the pressure is greatest and the flow has the greatest velocity.

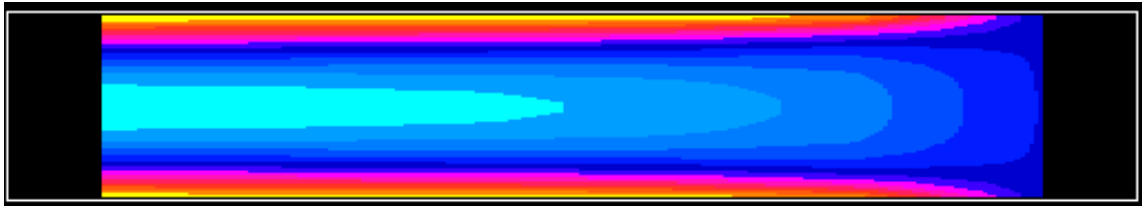


Figure 3.2: Simulation of a laminar fluid flow through a cylindrical pipe [35]

3.2.2. Fluid in Microchannels

As described above, fluid flow in very small channels is almost always laminar, simply because there is no room for turbulence. The viscosity of the fluid prevents the formation of pockets, eddies, and other forms of turbulence in such a confined space. A microfluidic flow is typically modeled as a Poiseuille flow through a duct, after the French physician J. L. M. Poiseuille, who experimented with low-speed flow in tubes.

Poiseuille flows are usually laminar flows that are independent of density and driven by pressure gradients.

Figure 3.3 shows the blood flow in human capillaries, and how it is a prime example of a Poiseuille flow. The relatively small capillary diameter ($6 - 10 \mu\text{m}$) and its relatively high coefficient of viscosity ($\eta = 0.0027 \text{ N}\cdot\text{s}/\text{m}^2$) force the blood flow to remain laminar while within the capillary. The flow is pressure-driven from the arterial side of the capillary and is independent of density, meaning that the particles in the blood do not cause turbulence in the flow.

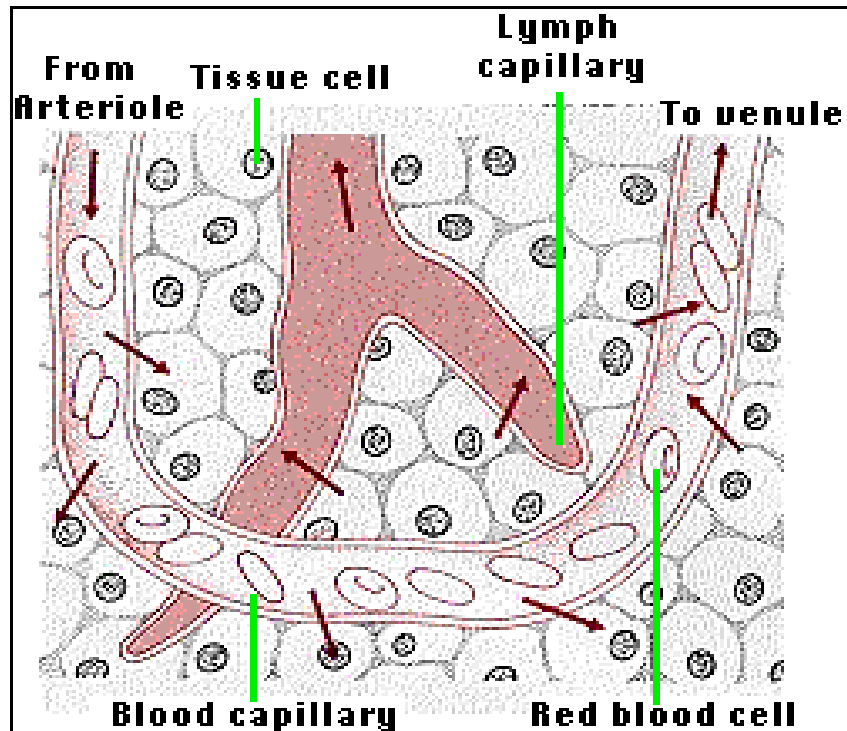


Figure 3.3: Rendition of a human capillary shown with red blood cells and pressure gradients (red-brown arrows) [36]

3.3. Transduction: Mechanical to Electrical Energy Transfer

A transducer is defined as any device that is actuated by power from one system and supplies power, usually in a different form to another system [37]. Table 3.1 lists the six main categories that are commonly used to classify transducers: thermal, mechanical, chemical, magnetic, radiant, and electrical. While the vast majority of transducers fall into one of these categories, there are many that either do not fit neatly into any of the categories, or else fit into several categories at once.

Table 3.1: Transducer categories and examples [24]

Transducer Categories	Examples
Thermal	temperature, heat, and heat flow
Mechanical	force, pressure, velocity, acceleration, and position
Chemical	concentration of chemicals, composition, and reaction rate
Magnetic	magnetic field intensity, flux density, and magnetization
Radiant	electromagnetic wave intensity, wavelength, polarization, and phase
Electrical	voltage, current, and charge

Transducers can be used to either detect changes in the environment (sensors) or to affect a change in the surrounding environment (actuators). Most complex autonomous systems today use a vast network of both sensors and actuators to accomplish their jobs. Sensing transducers detect changes in the environment and relay signals back to a control network. When the proper conditions are met, a signal is then sent from the control circuitry to an actuating transducer to affect the desired result in the

environment. Autonomous assembly robots are a perfect example of this control loop. They exert pressure on a part they need to lift and then use pressure sensors to determine if they have exerted sufficient force to lift the object without dropping it.

The human body is another example of a vast network of transducers. Nerve endings in the skin, eyes, ears, tongue and nose are capable of detecting minute changes in the environment, in any of the categories listed above. These changes are detected, converted to electro-chemical signals and sent to the main control unit, i.e. – the brain, which then determines a course of action and sends new electro-chemical signals down to the muscles to move the body.

The MFPG project, in attempting to create a miniature mechanically driven electromagnetic generator, actually requires two forms of energy conversion in order to generate electricity. The first energy conversion is from mechanical energy to magnetic energy. The water flowing through the microchannels will induce mechanical pressure on the turbine, causing it to rotate. This rotation causes a change in the magnetic flux emanating from the stator magnets. The second energy conversion is from magnetic energy to electrical energy, using the magnets on the stator and the conductive coil below the stator. The changing magnetic flux from the rotating stator induces an electrical current in the coil, producing the desired electrical current flow. This will be illustrated and discussed in detail in the next chapter.

3.4. Chapter Summary

In order to simulate conditions within the human capillaries, the MFPG project will require a laminar fluid flow within relatively small microchannels. This will allow for a close approximation to the actual pressure that would be applied to the turbine if the device were implanted in a human body. Also, the efficiency of the transducers involved in the project and their designs will determine the overall power output of the device.

IV. Calculations

4.1. Chapter Overview

A boundary exists in the behavior of materials, which is determined by the size and quantity of atoms of the material, and so, is different for each material. When dealing with a large sample of material, the material exhibits the characteristics that we are familiar with. When dealing with a relatively small sample, however, the material may exhibit radically different behavior in anything from malleability to resistivity.

The field of MEMS straddles this boundary, often using macro models as the basis for experimental designs. In order to produce the desired results, the equations used for these initial designs must be modified to account for the shift in material behavior. This chapter discusses the models and calculations that were used to create and analyze the designs for this project and how and why the models were modified from the original macro models. Due to the limitations of available tools and baseline material information, computer modeling/simulation of the device was not possible.

Since this project is a proof-of-concept demonstration, there are two designs discussed in the following two chapters when discussing the microchannels and the turbine: the ideal design and the fabricated design. The ideal design has the dimensions necessary to actually be implanted into the body and theoretically function. The fabricated design is roughly four times larger in all dimensions due to the limitations of manual assembly and accurate analysis that will be discussed in Chapters 6 and 7. The dimensions given in Table 4.1 show the size difference between the two designs.

Table 4.1: Critical design elements and dimensions for the Ideal and Fabricated designs.

	Ideal Design	Fabricated Design
Microchannel Radius (μm)	5	20
Microchannel Shape	Round	Square
Microchannel Path	Winding	Straight
Turbine Radius (μm)	48	192
Turbine Fan Blade Width (μm)	10	40
Turbine Fan Blade Height (μm)	10	40

4.2. Calculations

The equations used in this chapter were taken from a variety of sources. Those used for calculations regarding the micro fluid flow were initially empirically derived, but have proven to be applicable for calculating fluid flow parameters in most microchannels. The equations used to calculate parameters regarding the turbine were also empirically derived, but for much larger systems. It remains to be seen if these equations will remain valid at the micron scale. The calculations were accomplished using Mathematica version 6.01.

4.2.1. Fluid Flow in Microchannels

Since the MFPG device is intended to be used in conjunction with the flow of blood through human capillaries, the flow rate for capillary blood was calculated first. This flow rate was then used to determine the flow rate parameters in the MFPG microchannels.

The calculation starts with the basic equation for flow rate of a fluid in a microchannel, as given by

$$\Phi = (\pi r^4) / (8 \eta L \Delta P) \quad (1)$$

In this equation, Φ represents the flow rate, r is the radius of the capillary, η is the viscosity of the fluid, L is the length of the capillary, and ΔP is the change in pressure over the length of the capillary [16]. Using the values given in Table 4.2 for the standard parameters of human capillaries and blood, the resultant flow rate is approximately 0.0364 $\mu\text{L}/\text{min}$.

Table 4.2: Parameters used to calculate the flow rate of blood in human capillaries.

Parameter	Value
Capillary Radius (r)	5 μm
Viscosity of Blood (η)	0.0027 N-s / m^2
Capillary Length (L)	500 μm
Change in Pressure (ΔP)	3333.05 N / m^2

Given this flow rate, the pressure at the opening to the turbine chamber of an ideal MFPG device can be calculated using a modified form of Equation 1. Rearranging to solve for the change in pressure (ΔP), gives

$$\Delta P = (8 \Phi \eta L) / (\pi r^4) \quad (2)$$

The pressure at the inlet should be 5332.9 N/ m^2 , the same as in a standard human capillary on the arteriole side [17]. This leaves only the pressure at the turbine as an unknown. Using the parameters for the ideal MFPG microchannel, the viscosity of blood, provided in Table 4.3, and the flow rate from Equation 1, the pressure at the opening of the turbine chamber should be approximately 2000 N/ m^2 for a 500 μm long channel.

Table 4.3: Parameters used to calculate the pressure at the opening to the ideal turbine chamber.

Parameter	Value
Capillary Radius (r)	5 μm
Viscosity of Blood (η)	0.0027 N-s / m^2
Capillary Length (L)	2500 μm
Fluid Flow Rate (Φ)	$6.06 \times 10^5 \mu\text{m}^3/\text{s}$
Inlet Pressure (P_{Inlet})	5332.9 N / m^2

The length of the microchannel is a critical dimension for this design. As Figure 4.1 shows, the pressure at the opening to the turbine cavity decreases linearly with the length of the capillary. This is primarily due to the viscosity of the fluid. As discussed earlier, the viscosity of blood is relatively high and causes it to resist flowing through a sufficiently small channel. For this design, the cut-off length is approximately 800 μm . Beyond that length, blood will not flow through this capillary without additional pressure at the inlet.

For the fabricated MFPG device to have the same pressure at the turbine end of the microchannel, water must be pumped at a rate of 0.016 mL/min. This value was obtained from Equation 1, the MFPG microchannel parameters and the viscosity of water, given in Table 4.4, and the pressure from Figure 4.1.

Table 4.4: Values used to calculate pressure at the fabricated turbine chamber opening.

Parameter	Value
Capillary Radius (r)	20 μm
Viscosity of water (η)	0.001 N-s / m^2
Capillary Length (L)	20000 μm
Fluid Flow Rate (Φ)	$6.06 \times 10^5 \mu\text{m}^3/\text{s}$
Inlet Pressure (P_{Inlet})	5332.9 N / m^2

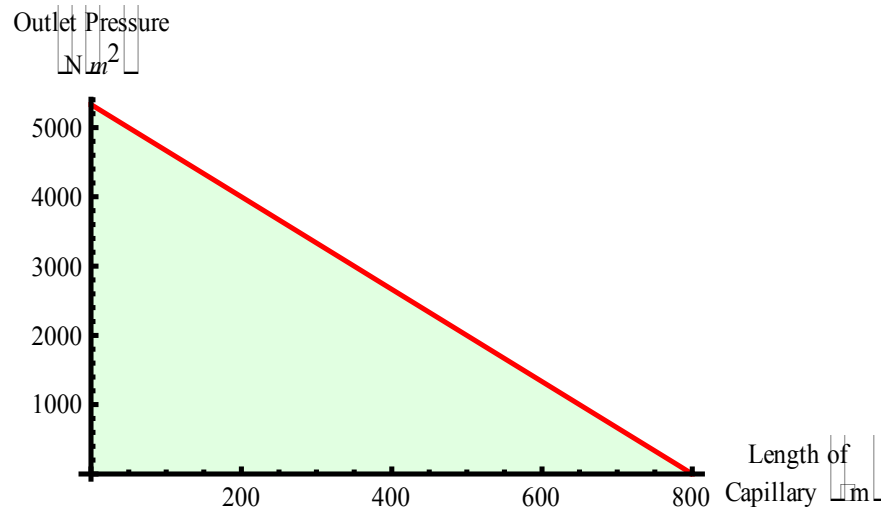


Figure 4.1: Fluid pressure in the microchannel as a function of channel length. Pressure at the channel inlet is 5332.9 N/m².

Again, a small change in the capillary length results in a change in the output parameters. In this case, the flow rate is inversely proportional to the capillary length. In order to maintain a constant pressure at the outlet, the flow rate of the fluid must change with the length of the microchannel, as shown in Figure 4.2.

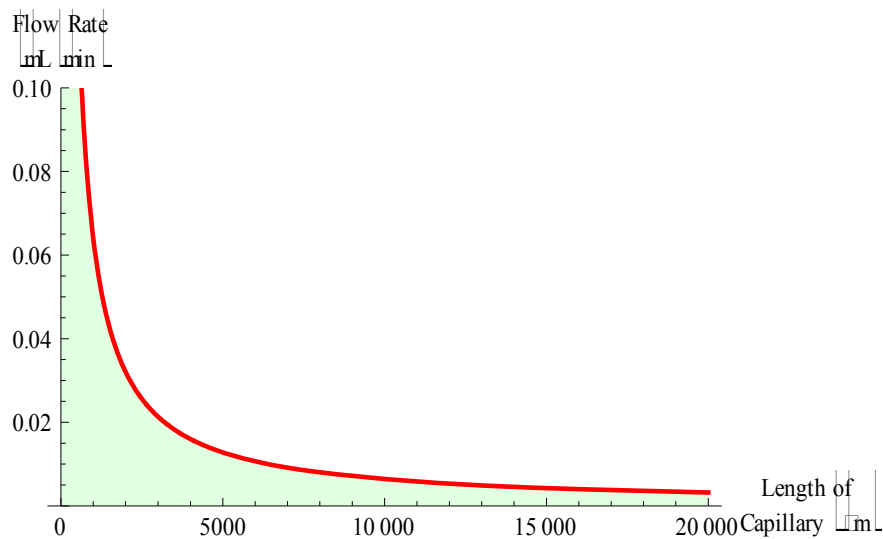


Figure 4.2: Change in flow rate as a function of capillary length, for a given change in pressure.

The parameters calculated are used in the next section to determine the angular velocity of the turbine, the torque applied to the turbine and the total work done on the turbine by the fluid per unit of time. As previously stated, the four stages of this device are all interconnected and so each affects the next. A change in any one of these stages will cause a ripple effect through subsequent stages. In addition, the data from this section is used in the experimental set-up for the analysis of the fabricated device.

4.2.2. Turbine Rotation

The Euler turbine equation (Equation 3) is based on the concepts of conservation of energy and conservation of angular momentum [38]. It is most commonly used to calculate the energy transfer between a fluid flow and a turbine, but can also be used to calculate the energy transfer from a mechanical device such as a compressor or pump, to the fluid flow[18]. The rate of energy conversion per unit mass is given as

$$W = \tau\omega = m\omega(C_{W1} r_1 - C_{W2} r_2) \quad (3)$$

where

τ = net torque exerted by or acting on the rotor

ω = angular velocity of the rotor

m = mass flow rate (kg/s)

C_{W1} & C_{W2} = tangential velocity, in the direction normal to the radius, of the fluid at the inlet and outlet

r_1 & r_2 = radial distance to the point of impact/release on the turbine blade

The standard thermodynamic sign convention for the Euler equation is that work done by a fluid is positive, and work done on the fluid is negative. For the scope of this project, the work produced by the turbine will be positive. By extension of the Euler

equation, the torque on the rotor can be determined by excluding the angular velocity.

This leaves the equation as

$$\tau = m(C_{w1} r_1 - C_{w2} r_2) \quad (4)$$

For this design, Equations 3 and 4 will be modified accordingly to account for differences in the design and the known variables for the ideal case. For instance, the tangential velocity of the fluid at the outlet is unknown and cannot be accurately measured due to current technological restrictions. The torque, therefore, can only be calculated for the ideal case where the tangential velocity of the fluid at the outlet is zero. Energy loss due to friction between the turbine and its housing is also assumed to be negligible because the turbine is suspended within the fluid. Given these assumptions, the torque acting on the turbine can be simplified to a perpendicular force acting on an object at a given distance from the objects center. Torque can therefore be calculated using the previously calculated fluid pressure at the opening to the turbine cavity using the relationship

$$\tau = P A r \quad (5)$$

where P is the pressure at the opening, A is the cross-sectional area of the channel and r is the radial distance from the center of the turbine to the point of impact on the blade, as shown in Figure 4.3. For this design $r = 92 \mu\text{m}$. The torque for the fabricated design should be $2.94 \times 10^{-4} \mu\text{N-m}$.

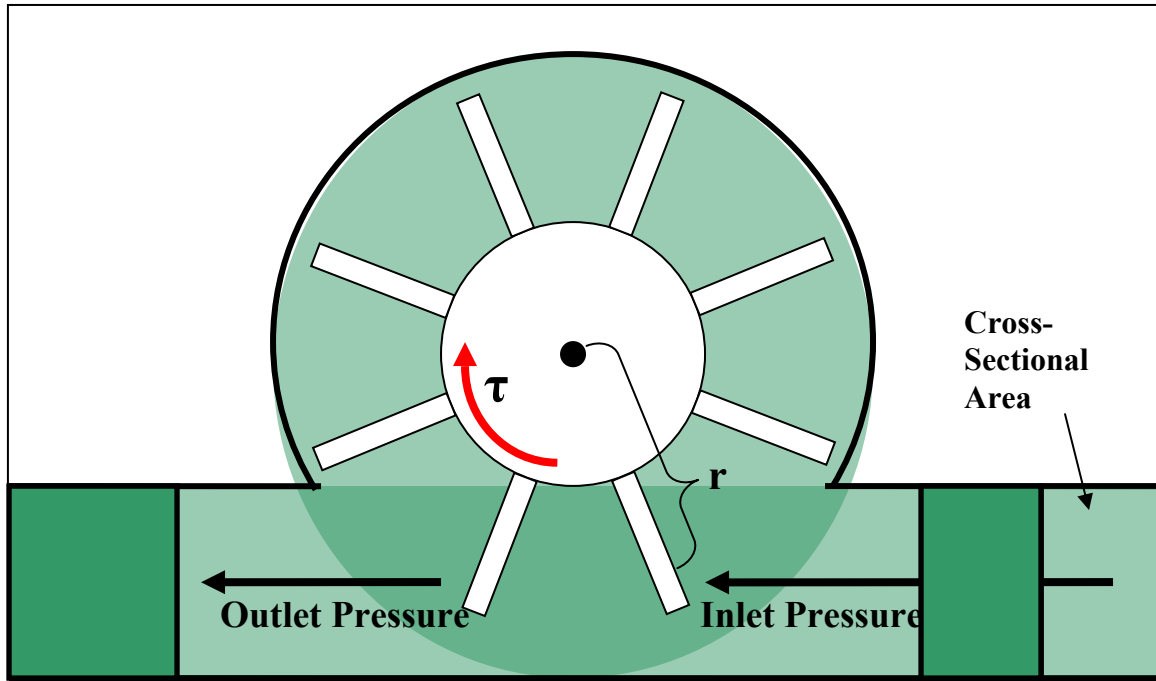


Figure 4.3: Cross-sectional view of turbine showing fluid pressure and resultant torque.

To calculate the angular velocity of the fabricated turbine, the simplified model of a particle in a two-dimensional plane shown in Figure 4.4 can be used because the movement of the turbine is restricted in the z -direction. The turbine's movement is also restricted in the radial direction (V_{\parallel}), so that the velocity is purely in the perpendicular direction (V_{\perp}). The turbine's angular velocity is given by

$$\omega = V_{\perp} / r \quad (6)$$

The calculations for the ideal angular velocity of the turbine, assuming no loss due to friction or backpressure, should be 4.12 radians/second. This translates to a rotation rate of approximately 39.3 revolutions/minute. Since the turbine and stator are connected via the turbine shaft, the stator should also be rotating at 39.3 rpm.

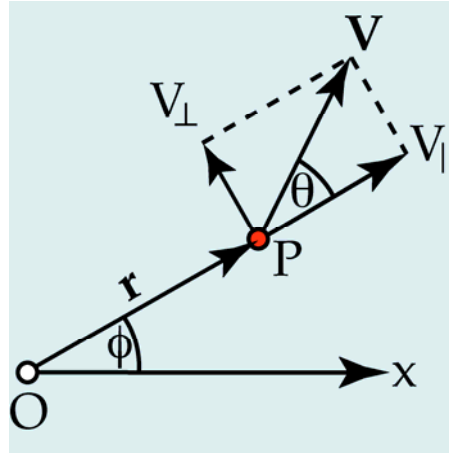


Figure 4.4: Vector diagram for the angular velocity of a particle in a 2-dimensional plane [39].

From Equation 3, the rate of energy transfer from the fluid to the turbine can be determined by multiplying the angular velocity of the turbine by the applied torque. For the fabricated design, this results in an energy transfer rate of $1.213 \times 10^{-9} \text{ N-m/s}$. Although this is a key figure of merit for turbine designs, it will have limited effect on the overall power output of the device. Rather, it is the electromagnetic portion of the device that will affect the majority of the power output characteristics.

4.2.3. Electromagnetic Induction

The four fundamental equations of electromagnetism, known as Maxwell's equations, describe the behavior of electric and magnetic fields. Maxwell's third and fourth equations,

$$\nabla \times \mathbf{E} = -\partial \mathbf{B} / \partial t \quad (7)$$

$$\nabla \times \mathbf{B} = \mu_0 \mathbf{J} + \mu_0 \epsilon_0 \partial \mathbf{E} / \partial t \quad (8)$$

describe the interaction of electric and magnetic fields and are the most relevant to this project. Equation 8, known as Ampère-Maxwell Law, describes the current density (J) and the displacement current ($\partial E/\partial t$) produced by the curl of the magnetic field ($\nabla \times B$). This means that a time changing magnetic field will induce a current in a wire or loop within the field, as illustrated in Figure 4.5 [24].

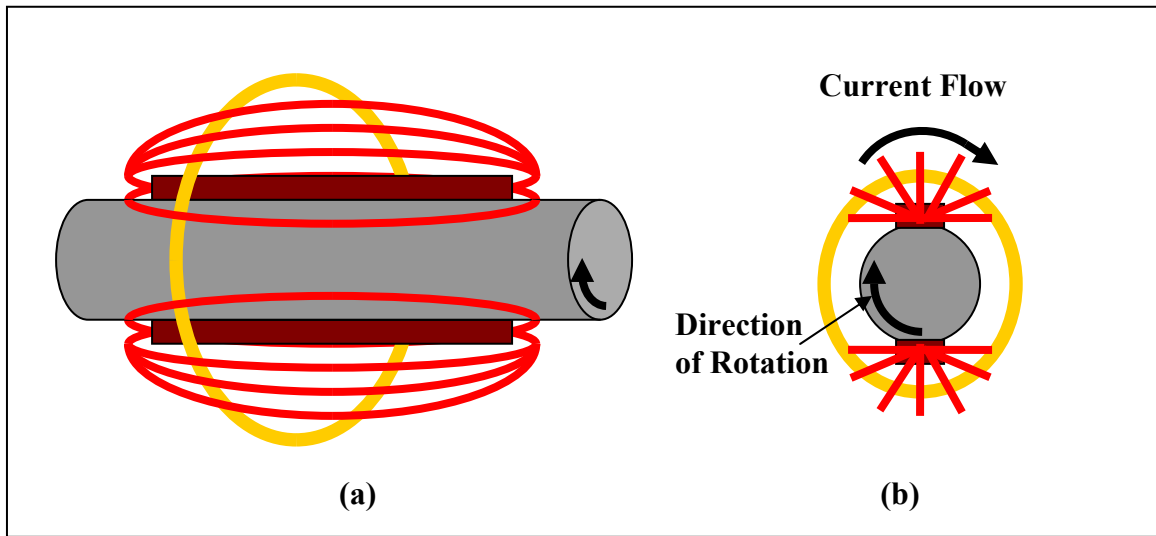


Figure 4.5: Side view (a) and end view (b) illustration of Ampere-Maxwell current induction in a loop of wire (gold) due to a time-changing magnetic field (red).

This method of power generation is the basis for most of today's energy production. All modern power plants, with the exception of solar plants, either superheat a liquid or use the force of gravity acting on water to turn a turbine, which in turn, turns an array of large permanent magnets. These arrays induce a current flow in thousands of coils of wire surrounding them, thus producing the electricity that touches every aspect of human life today.

The Ampère-Maxwell Law is also the basic equation that describes the current produced by the MFPG device. Once magnetized, the nickel blocks on the stator will produce a constant magnetic field. Once the turbine and stator begin to move, the coil below the stator will no longer be sitting in a constant magnetic field, but will instead be immersed in a time-changing magnetic field. As an arm of the stator passes over a point on the coil, the coil will experience a relatively strong magnetic field due to an increased number of magnetic flux lines penetrating its surface. The coil will then experience a relatively weak magnetic field as a gap between the stator arms passes above it.

If the cross-sectional area of the loop and either the magnetic field (B) strength or the magnetic flux (Φ) is known, the remaining variable can be calculated using

$$\Phi_B = \int \mathbf{B} \cdot d\mathbf{A} \quad (9)$$

where dA is the cross-sectional area element in vector form. Equation 9 can be simplified to

$$\Phi_B = B A \cos(\Theta) \quad (10)$$

where Θ is the angle between the magnetic field and the cross-sectional area. This is maximized when $\Theta = 0^\circ$ (the field is perpendicular to the area, Figure 4.6a) and minimized when $\Theta = 90^\circ$ (the field is parallel to the area, Figure 4.6b). Using Equation 10, the maximum theoretical value for the magnetic flux density, and the dimensions of both the stator magnets (580x80x20 μm) and the cross-sectional area of the coil ($2 \times 10^{-11} \text{ m}^2$), each of the magnets can produce a field of 32 Teslas.

Given this magnetic field strength, the theoretical current can then be calculated using a simplified version of Equation 8.

$$\nabla \times \mathbf{B} = \mu_0 \mathbf{J} \quad (11)$$

Equation 11 assumes that the displacement current component ($\partial \mathbf{E} / \partial t$) from Equation 8 is negligible compared to the current density (\mathbf{J}). While this is not strictly accurate, it is sufficient for these rough calculations. Given the above conditions, the stator and coil could generate approximately $0.85 \mu\text{A}$.

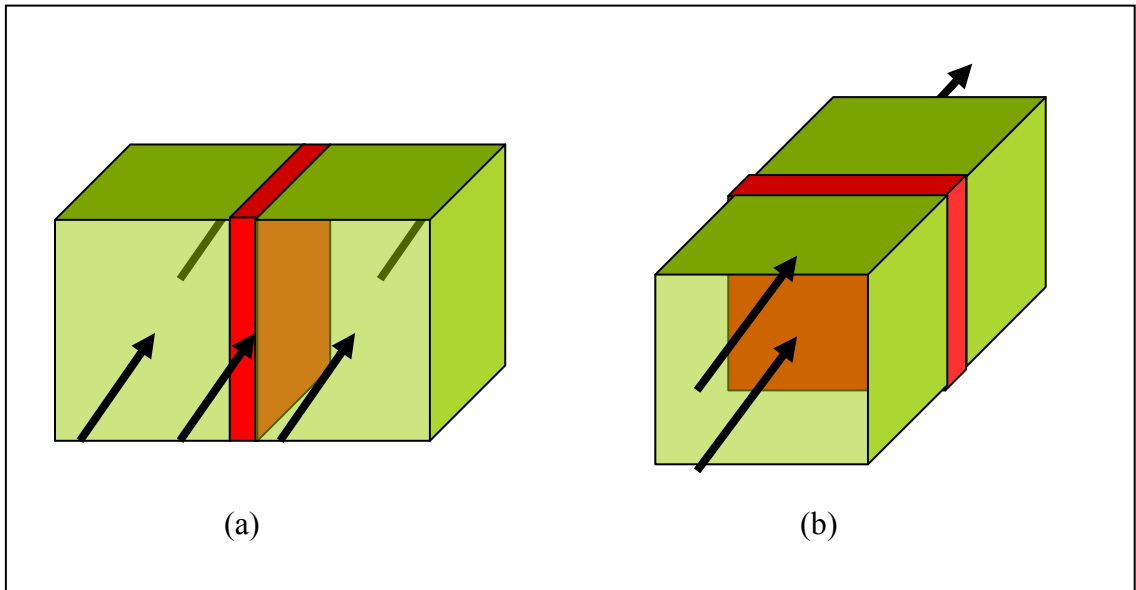


Figure 4.6: Magnetic field lines shown perpendicular (a) and parallel (b) to the cross-sectional area.

Current flowing through the coil will generate a voltage difference between the ends of the coil due to the resistance of the coil material. Equation 12 shows that the resistance in a wire is due to the resistivity (ρ) of the material and the dimensions of the

wire, where L is the length of the wire and A is the cross-sectional area of the wire. This equation is sufficient for the given coil dimensions, because quantum scale effects such as electron-electron collisions do not have any significant effects for thicknesses above 15nm [40].

$$R = \rho L/A \quad (12)$$

At room temperature (20 °C), gold has a resistivity of $2.44 \times 10^{-8} \Omega\text{-m}$. The fabricated coil will have a length of 46.18 mm and be $10 \times 2 \mu\text{m}$, for a cross-sectional area of $20 \times 10^{-12} \text{m}^2$. This will give the coil a resistance value of 56.34 Ω .

Using this resistance value, Equations 13 and 14 give a maximum voltage of 382 μV and an output power of 2.6 nW.

$$V = IR \quad (13)$$

$$P = VI \quad (14)$$

The dimensions of the stator magnets and the coil can be adjusted, however, to increase the power output from the same design, as shown in Figure A.13 - 17 Figure A.17. The initial design has the stator magnets at 80 μm wide. The height of the magnet can be changed during fabrication by electroplating additional nickel onto the magnet. The output current of the device is given as a function of the magnet height (X) by

$$I_{T1} = (8 \Phi_{\text{NI-g}} W_M X) / (\mu_0 \kappa_m) \quad (15)$$

where $\Phi_{\text{NI-g}}$ is the magnetic flux density of the nickel, W_M is the width of the magnet, μ_0 is the magnetic permeability of freespace, and κ_m is the ratio of the permeability of the material to the permeability of freespace (μ/μ_0).

By changing only the height of the magnets, Figure 4.7 shows that the output current of the device increases linearly to 27 μA , when the stator is 80 μm x 80 μm . This is an increase in the output current of two orders of magnitude over the 20 μm thick stator magnets.

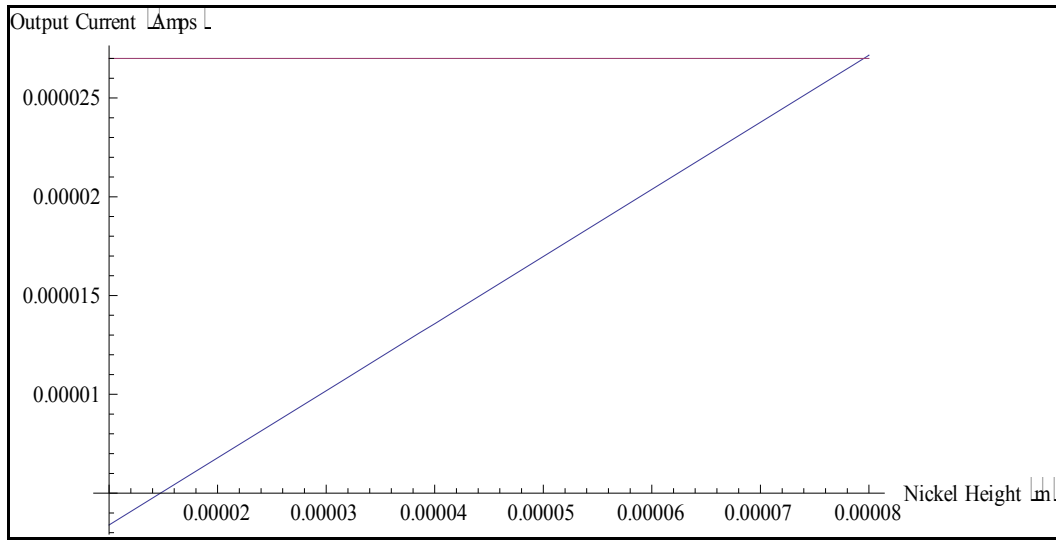


Figure 4.7: Output current as a function of the stator magnet height, or thickness. The current increases linearly with the height of the magnets.

The voltage generated in the coil and the total power output can also be changed by altering the dimensions of the coil. Equation 16 shows the voltage generated by current flowing through the coil and Equation 17 shows the output power of the device, both as functions of the cross-sectional area of the coil (A_{C1}). The length of the coil was measured through the center of the coil.

$$V_{C1} = (I_{Th} \rho_{Au} L_C) / A_{C1} \quad (16)$$

$$P_1 = (I_{Th}^2 \rho_{Au} L_C) / A_{C1} \quad (17)$$

Figure 4.8 shows the output voltage curve for the coil cross-sectional area between $2.5 \times 10^{-12} \text{ m}^2$ and $20 \times 10^{-12} \text{ m}^2$. The voltage increases as the cross-sectional area of the coil decreases for a maximum value of 12.2 mV when the cross-sectional area is $2.5 \times 10^{-12} \text{ m}^2$. If both the height and width of the stator magnets are changed simultaneously, the output voltage curve becomes parabolic.

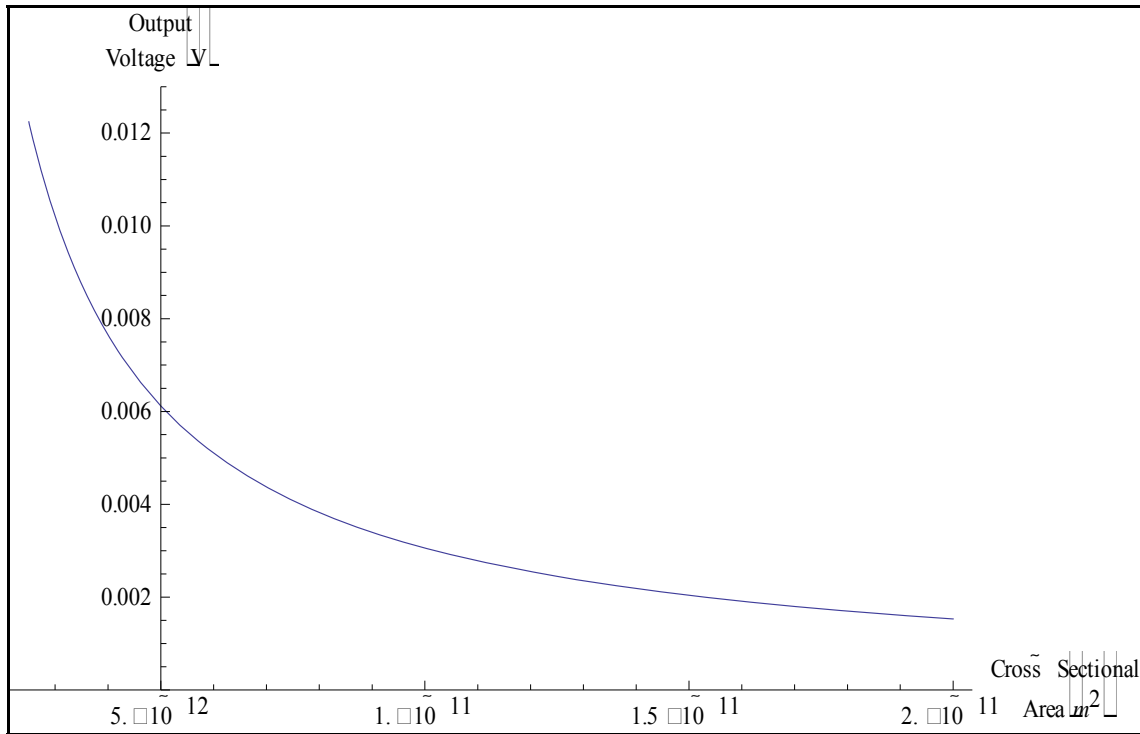


Figure 4.8: Output voltage as a function of the cross-sectional area of the coil. Voltage is maximum when the cross-sectional area is minimum.

Since power can be found by multiplying voltage by current, Equation 17 generates a curve that is very similar to the voltage curve from Figure 4.8. Indeed, Figure 4.9 looks very similar, and again is maximized for a minimum value of the cross-sectional area of the coil.

The maximum theoretical power output from this device, given the stator magnet dimensions of $580 \times 80 \times 80 \mu\text{m}$, the coil dimensions of $46,200 \times 10 \times 0.25 \mu\text{m}$, and the maximum flux density for nickel of 600 gauss, is approximately $0.3325 \mu\text{W}$.

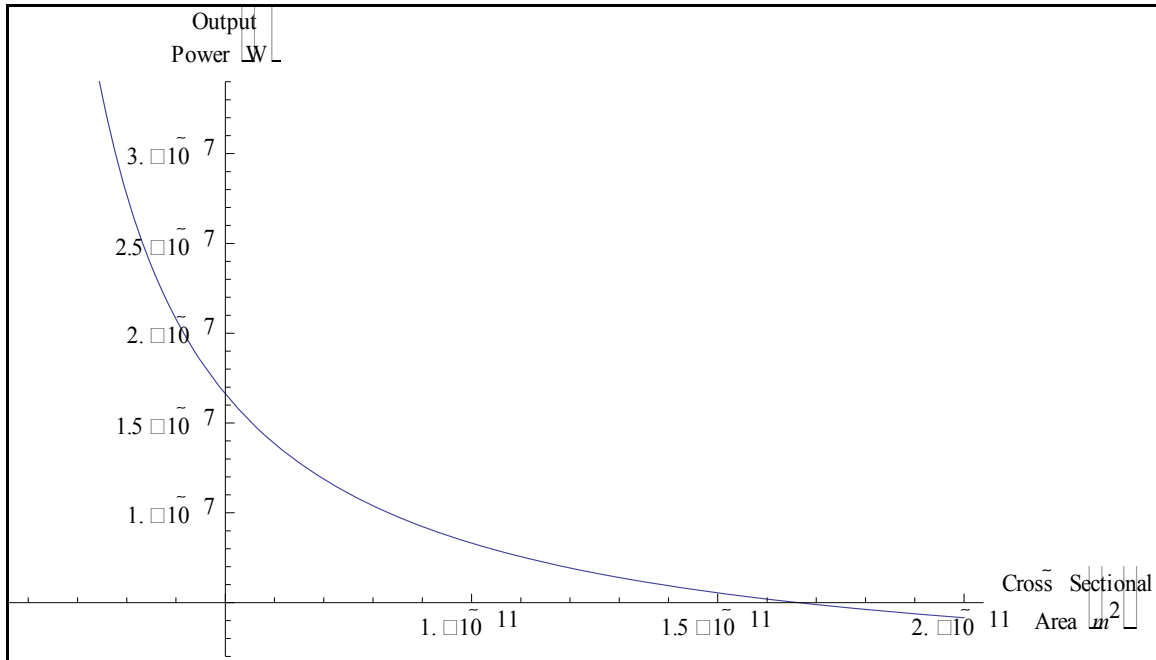


Figure 4.9: Power output of the device as a function of the cross-sectional area of the coil. Like the output voltage, output power is maximized when the coil cross-section is minimized.

4.3. Chapter Summary

These calculations, while small, represent the possibilities inherent in this design. Small changes in any of the four sections of the device have great effects on the overall output power of the device. Also, total power output may be increased by connecting two or more of the devices in series or parallel, depending on the need for either increased current or voltage.

One possible problem that these calculations do not illustrate is the danger of overloading the coil. While the voltage and therefore the power is maximized as the cross-sectional area of the coil decreases, trying to push too many electrons, too quickly through that small of a wire may cause the wire to melt or deform. Keeping the coil several times wider than the height of the coil may help to alleviate this possibility by providing increased contact area to the substrate, which acts as an infinite heat sink.

V. Designs

5.1. Chapter Overview

Engineering design is an iterative process, often taking numerous design modifications before a working design is finalized. Nowhere is this truer than when designing MEMS structures. Because of the shift in material behavior when going from a macro scale to a micro scale, devices often behave differently than a macro model would predict. This means that a novel MEMS design must often be created, analyzed, and redesigned several times before the desired results are achieved. This chapter provides details concerning the origins of the MFPG device designs and the effects of each design element on the overall performance of the device.

5.2. Design Inspiration

As with any good design, the inspiration for the MFPG designs came both from nature and from previous technological marvels. The design for the microchannels came directly from basic human physiology, namely the circulatory system. Designs for the generator, however, came from hydroelectric power plants like the ones operating at the Hoover Dam.

5.2.1. Inspiration From Human Physiology

In order to harvest energy from within the body, the different potential sources must first be identified. The human body utilizes several forms of energy, including chemical, electrical, thermal, mechanical and magnetic.

Since electrical energy is the desired output, the electrical energy in the body would be an ideal source. The only problem with this is that the electrical energy is only

present in the nervous system. Attempting to harvest this energy directly could have negative repercussions on the person, ranging from minor loss of feeling to permanent systemic damage to the nervous system.

Magnetic energy is commonly used to generate electrical energy. Attempts to harvest this energy from the body should not have any lasting effects as the bio-magnetic field is present everywhere in the body and harvesting tools tend to be static. The major drawback to this is the relative weakness of the bio-magnetic field. As Figure 5.1 shows, the biomagnetic field, at its strongest point surrounding the heart, has a strength of only ~ 10 picoTeslas, roughly $1/100,000^{\text{th}}$ the strength of the Earth's magnetic field and twelve orders of magnitude less than a Magnetic Resonance Imaging (MRI) scan [41]. As such, it is extremely difficult to measure and would be even more difficult to extract energy from the field.

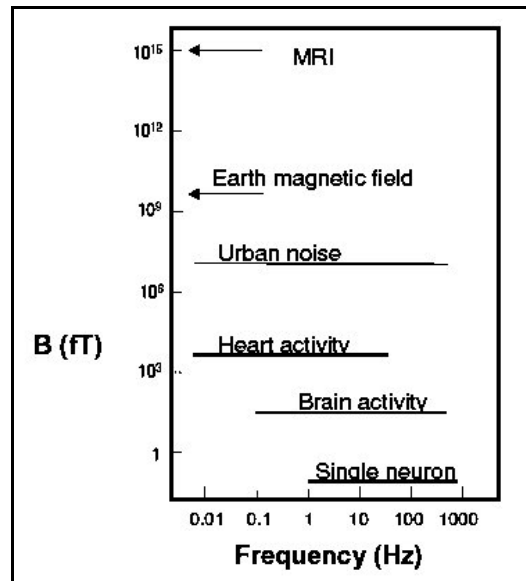


Figure 5.1: Typical amplitudes and frequency ranges for various biomagnetic fields and reference fields. Field strength is in $\text{fT} = 10^{-15} \text{ T}$ [41].

The components for an electrochemical cell are abundant within the human body. Zinc and copper, the two most common metals used in simple electrochemical cells are minerals that the human body must have to function properly [42]. The problem arises from the need to extract the minerals from the body, store them in a usable fashion, like the simple voltaic cell shown in Figure 5.2, and return the ionized waste to the body for disposal. Again, this is a complex, but potentially feasible method for harvesting energy from the human body.

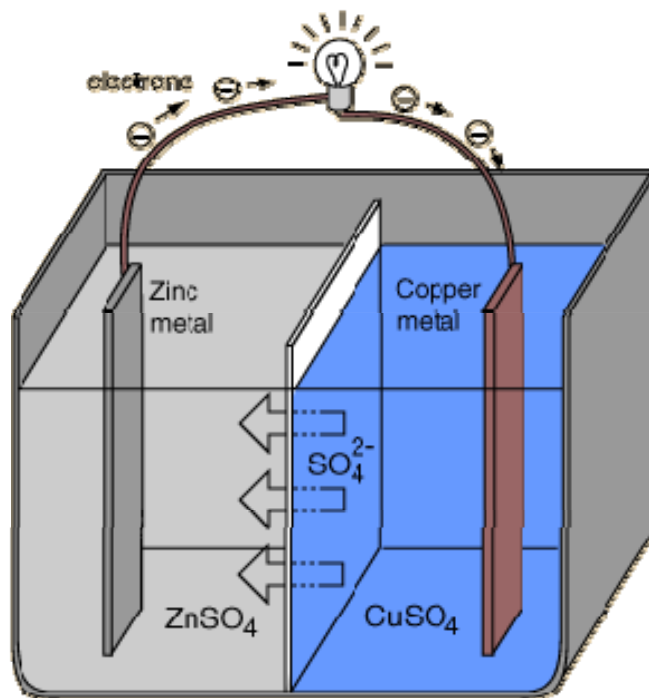


Figure 5.2: Simple zinc/copper voltaic cell with 1.1V potential under standard conditions [43]

Thermal energy systems are an efficient method of doing work. They rely on the expansion and contraction of molecules due to the application of hot and cold temperatures, respectively. These principles have been applied on a large scale in both

the Ocean Thermal Energy Conversion (OTEC) process [44] and geothermal heat pumps which are commonly used to heat and cool residential housing [45]. The OTEC process uses a low-boiling-point fluid such as ammonia to turn an electromagnetic turbine. Warm ocean water is used to vaporize the ammonia and the resulting expansion of the vapor turns the turbine. Cool ocean water is then used to condense the ammonia so that it may be used again. One potential problem with using thermal energy for generating electricity within the human body is the lack of a temperature variation over small distances. Without the ability to cool the low-boiling-point fluid, the device would only operate during the initial vaporization.

This leaves only mechanical energy as a potential source. There are two primary sources of mechanical energy within the body, the first being the expansion and contraction of muscle tissue and the second being the flow of fluids through the body. Energy could be harvested from the expansion and contraction of muscle tissue using implanted piezoelectric materials. Energy flow from these implants, however, would be dependent upon the level of activity of the muscles into which they were implanted. Also, a secondary means of collecting and analyzing the patient's blood would still be necessary.

Fluid flow in the human body occurs in two systems: the digestive system and the circulatory system. There is potential use for such a device in the digestive tract, but not for analyzing blood. Since the circulatory system is the primary means of moving blood throughout the body, has a constant flow rate through the capillaries, and transports the very substance that is to be analyzed, it is an ideal source of energy for this device.

5.2.2. Inspiration From Hydro-Electric Dam

Once the circulatory system was identified as a likely source for energy harvesting, how to extract the energy from the fluid flow efficiently, became the question. The most likely answer came from a device that has been employed as long as humans have used electricity and who's predecessors have been employed by humans for hundreds of years: the hydroelectric generator, shown in Figure 5.3.

The basic operating principles for a hydroelectric generator are simple. The fluid flow turns a large paddle wheel, known as the turbine, which is attached to a shaft. The shaft translates the motion of the wheel to a set of magnets, known as the stator. The stator is surrounded by numerous coils of wire, usually made of copper. As the stator turns, the flux generated by the magnets induces a current in the copper wire, thus producing electricity.

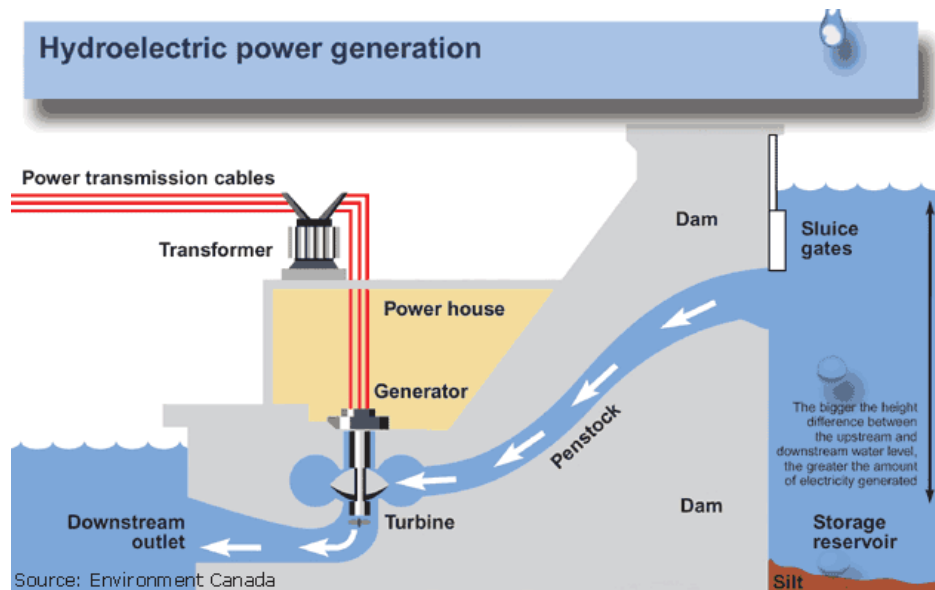


Figure 5.3: Standard hydroelectric power plant model using an impulse turbine [46].

5.3. Design Details

From these two sources of inspiration, three designs were created: one for the microfluidic channels and two for the generator design. The dimensions for the designs were given previously in Section 4.1.

5.3.1. Microfluidic Channel Design

The primary concern when creating the microfluidic channel design was to mimic human capillaries in order to minimize disruption in the blood flow. This was done by matching the diameter of the channels to the average size of human capillaries, roughly $10\text{ }\mu\text{m}$. By doing this, changes in pressure associated with switching from a diameter of one size to another are minimized.

The second concern was to allow sufficient spacing between detection devices. This is why the original channel design, shown in Figure 5.4, shows winding channels.

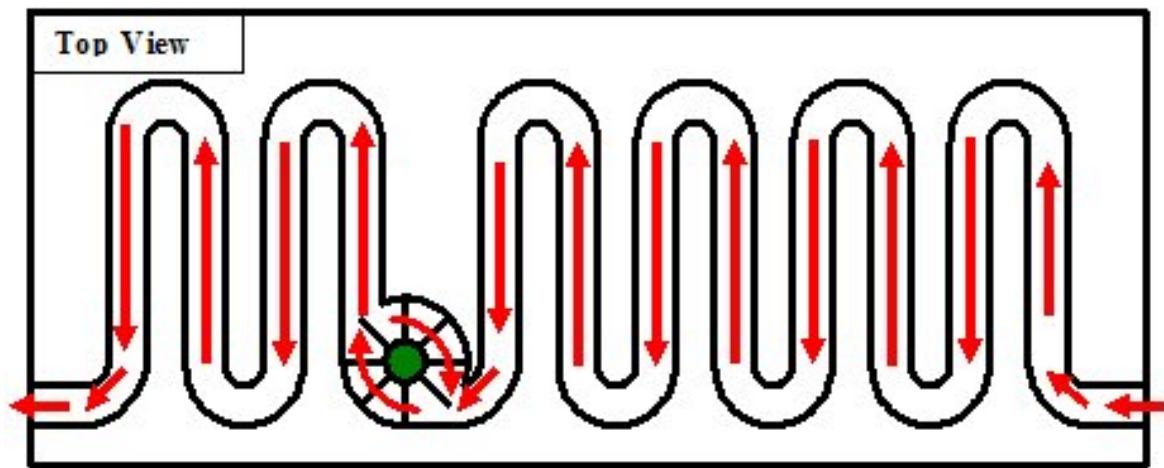


Figure 5.4: Top view of original microfluidic channel design with winding microchannels.

The specific material that is being monitored in the fluid can be detected through two methods. The first method, impedance spectroscopy, measures the resistance change between a set of voltage probes, operating at a given frequency. The probes are coated with a protein specific to the protein or molecule that they are monitoring for and would operate by measuring the voltage difference between the positive and negative probes [47]. This change in the resistance would be due to the presence or absence of the target in the fluid. Sufficient space would be required between probe pairs to prevent voltage from one pair interfering with the next. The second method, refractive index detection, has recently been shown to be a sensitive, universal detection scheme for identifying the composition of a microfluid flow for several lab-on-a-chip applications. A low-powered laser is directed through the fluid channel and detected on the other side. A deflection of the laser beam or a shift in its intensity can be used to identify the composition of the fluid [48].

Since this is a proof-of-concept design, the microchannels and the turbine were designed roughly four times the size of the ideal device described above. This alleviated some difficulties associated with handling and measuring such a small fluid flow.

5.3.2. Original Generator Design (Gear Ratio Design)

Figure 5.5 shows the original design for the generator portion of this project. It consists of a vertical turbine shaft linked by gears to a horizontal stator shaft, all sandwiched between three layers of glass wafers. The key advantage to this design is the ability to change the rate of rotation of the stator shaft. This can be done by changing the relative sizes of the two gears shown in Figure 5.6. The gear ratio will determine the

frequency of the output current and can be adjusted to match the demands of the application.

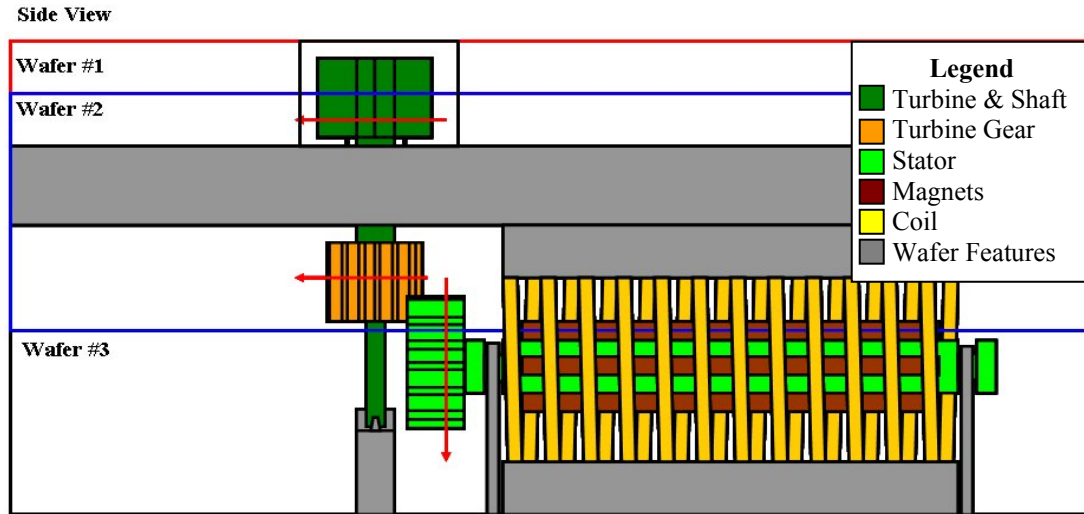


Figure 5.5: Original generator design with horizontal stator shaft.

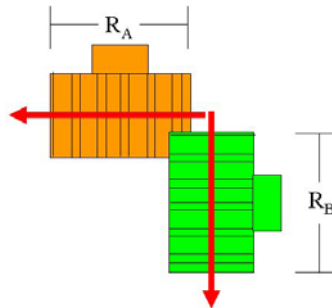


Figure 5.6: Gears used for original generator design with respective radii: Gear A - Turbine shaft gear, Gear B - Stator shaft gear.

The primary drawback to this design is the difficulty associated with trying to deposit nickel along the length of the stator. Since nickel requires a seed layer to adhere to silicon, the stator shaft would have to be fabricated horizontally. This would require the shaft to be hinged, as shown in Figure 5.7, either in four sections attached along the

length of the shaft (1) that could be folded together, or in two long sections hinged in the middle (2) that could be folded together and fused.

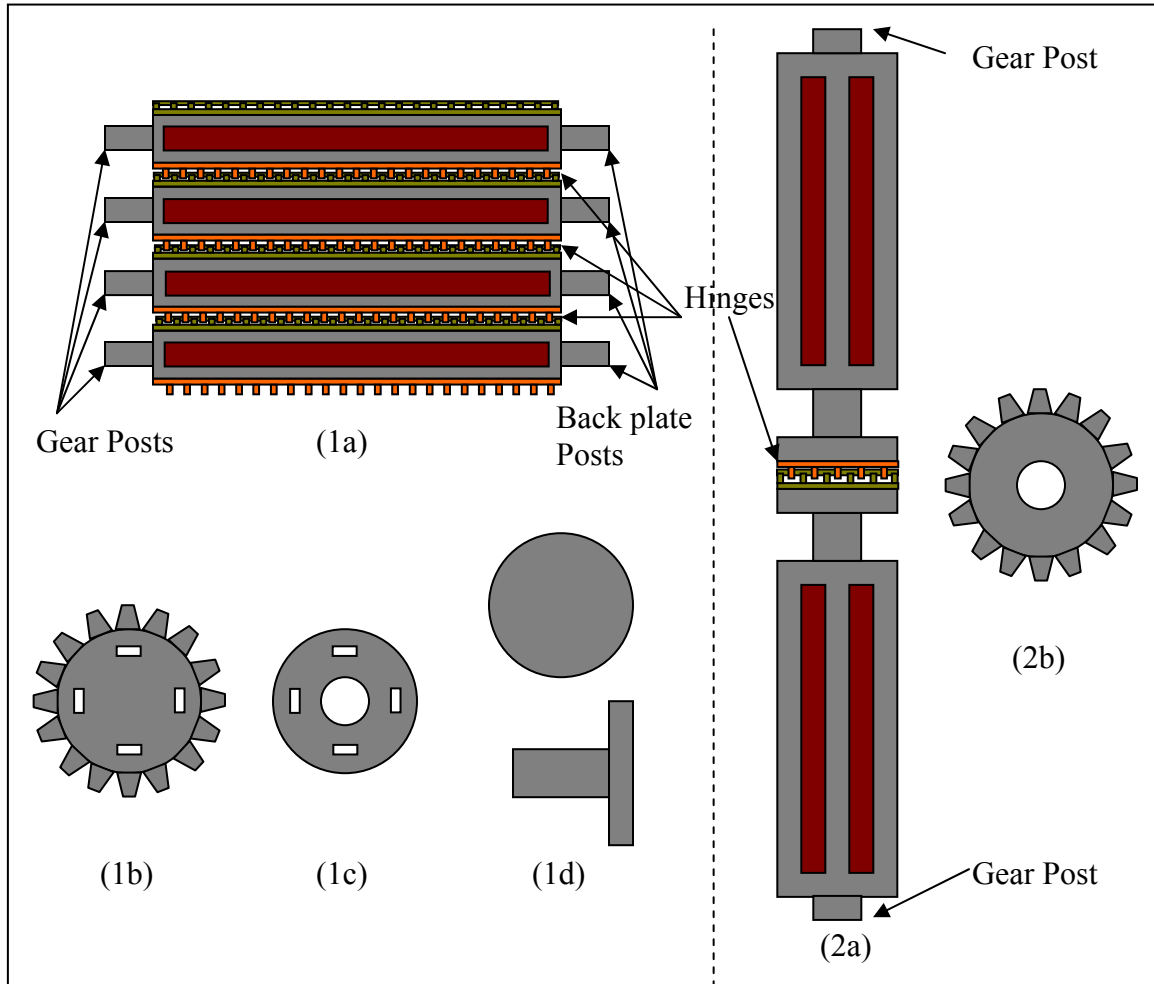


Figure 5.7: Hinged designs for the stator shaft (a) with stator gears (b) and back plate components (c and d).

Because of limitations in the methods that could be used to create the hinged designs (i.e. – PolyMUMPS, SU-8 reflow, micromolding, etc.), the hinges may not be thick enough or robust enough to withstand the constant motion of the device for an

appreciable length of time. Also, these micron-sized parts would need to be assembled by hand, using tweezers and a microscope.

5.3.3. Revised Generator Design (Flat Coil Design)

Given the limitations in fabricating the first design, a simpler design was created for the express purpose of removing the horizontal stator shaft. The design shown in Figure 5.8 was named the “Flat-coil Design” because the gold wires lay flat on the bottom wafer in an expanding coil, as shown in Figure 5.9a.

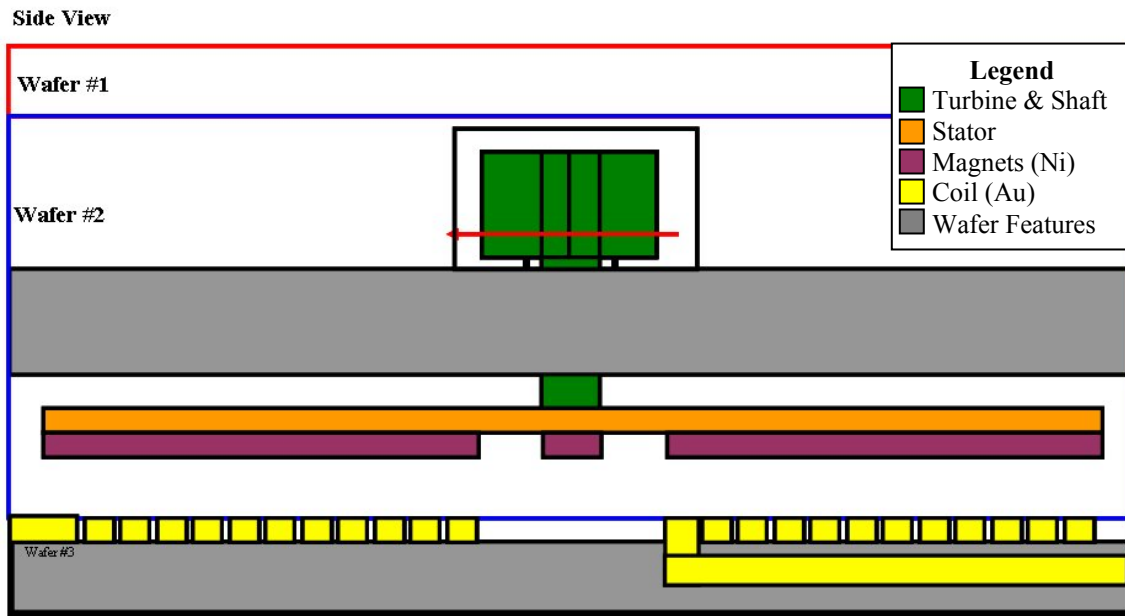


Figure 5.8: Side view of the flat-coil design illustrating the horizontal stator with magnetized nickel suspended above a gold coil.

The magnetic induction in this design comes from the flat stator, shown in Figure 5.9b, which now attaches directly to the turbine shaft and is suspended above the induction coil. This greatly reduces the difficulties associated with fabrication and nickel

deposition and also simplifies the assembly of the device, as only two pieces must be inserted into the glass wafers and fused together.

Like the previous design, the frequency of the output current can be designed. For this design, however, the frequency of the output current is dependant on the diameter of the outer gold coil. As the electrons are pushed through the gold coil, the spacing between peaks becomes larger. This is due to the increasing distance between the magnets on the stator arms in the radial direction. Once the electrons leave the coil and the presence of the magnets, the frequency should remain constant.

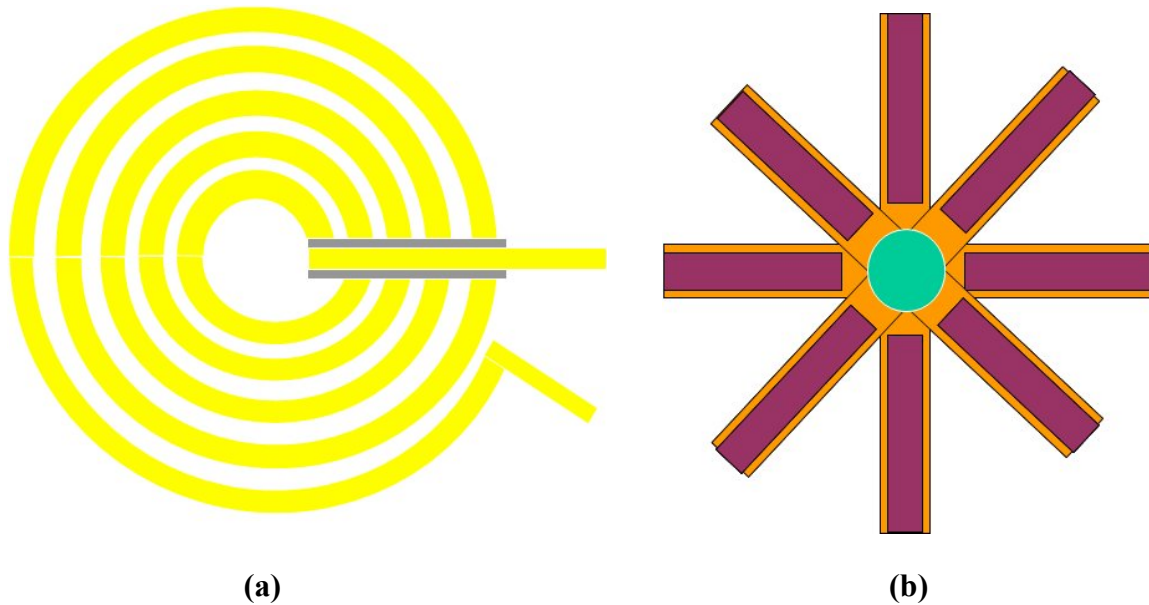


Figure 5.9: Bottom view of gold induction coil with partial nitride layer (grey) shown where the wires cross (a) and stator arms with nickel (purple) (b) in the flat-coil design.

One possible problem with this design is the potential for overheating the gold at the return junction of the coil. The frequency difference between the current returning to the coil and the current in the innermost loop may cause an electron vacuum, forcing the

returning electrons to accelerate. This will cause an increase in electron collisions and, by extension, an increase of thermal energy being given off.

5.4. Dominant Design Elements

For both of the designs, there are four main factors that will determine the level of power output from this device. They are, 1) the rate of fluid flow in the microchannels, 2) the speed with which the turbine rotates, 3) the size and magnetic properties of the stator magnets, and 4) the dimensions and number of loops in the induction coil. Because of the nature of transduction from mechanical to electrical energy, all four of these factors are inter-connected and a change in any one will result in a change of the overall power output.

5.4.1. Fluid Flow Rate

Since this device is meant to interface with human capillaries, the fluid flow through the device should mimic the flow of blood in the body. Given the precautionary measures necessary for dealing with blood, however, the designs will be tested using water as the fluid flowing through the microchannel. As discussed in Section 4.2.1, the critical variable for flow through the ideal MFPG device is the head pressure, or the pressure at the opening to the turbine cavity. This dictates the force that the fluid will have as it strikes the turbine and, by extension, the speed with which the turbine will rotate. Once the ideal head pressure was calculated, the microchannel dimensions for the fabricated MFPG device could be determined to match the head pressure of the ideal MFPG device and to determine the flow rate of the water through the fabricated

microchannels. The fabricated microchannels were lengthened to accommodate the design of the Lab-on-a-chip microfluidic analysis kit. This was done to simplify testing of the devices.

5.4.2. Turbine Size (Rate of Rotation)

Once the flow rate for water in the fabricated microchannels was calculated, the dimensions for the turbine were determined. Since the microchannels were designed roughly four times larger than the ideal design, the turbine also had to be roughly four times its ideal size. The critical dimensions for the turbine are the size and shape of the blades and the distance from the axis of rotation to the point of impact of the fluid on the blades [49]. Because of the difficulty in fabrication, the turbine blades were designed to be straight vertical paddles. Their dimensions roughly match the size of the microchannels, with the height being slightly less to prevent friction and the width being slightly larger to allow extra space for the fluid.

5.4.3. Dimensions and Material for Stator Magnets

The primary concern with the design for the stator was having sufficient mass of the ferromagnetic material to generate an appreciable magnetic field. Since no relevant documentation exists on the strength of a magnetic field given a small volume of material, the stator was designed to maximize the volume of the ferromagnetic material while not being overly heavy.

The second concern for the design of the stator was the composition of the ferromagnetic material itself. Table 5.1 shows the magnetic properties of various commonly used ferromagnetic materials and how each is obtained. The strongest

magnetic fields are generated by pure iron [50], like the iron core of the earth. However, iron is not typically used in MEMS processes. It can however be deposited with nickel in a nickel-iron electroplating bath that is commonly used in the LIGA process [51]. The same cannot be said of permalloys and cobalt, which are not used for MEMS. Nickel, the material with the fifth highest flux density, is more commonly used in the MEMS process and can be easily and inexpensively deposited in the necessary shape and size. When nickel is 99% pure and has been annealed to remove crystalline defects it has a maximum relative permeability of 600 and a remanent flux density of 0.4 Teslas.

Table 5.1: Magnetic properties of ferromagnetic materials [43].

Material	Treatment	Initial Relative Permeability (H/cm ²)	Maximum Relative Permeability (H/cm ²)	Coercive Force (oersteds)	Remanent Flux Density (gauss)
Iron, 99.8% pure	Annealed	150	5000	1.0	13,000
Iron, 99.95% pure	Annealed in hydrogen	10,000	200,000	0.05	13,000
78 Permalloy	Annealed, quenched	8,000	100,000	0.05	7,000
Superpermalloy	Annealed in hydrogen, controlled cooling	100,000	1,000,000	0.002	7,000
Cobalt, 99% pure	Annealed	70	250	10	5,000
Nickel, 99% pure	Annealed	110	600	0.7	4,000
Steel, 0.9% C	Quenched	50	100	70	10,300
Steel, 30% Co	Quenched	---	---	240	9,500
Alnico 5	Cooled in magnetic field	4	---	575	12,500
Silmanal	Baked	---	---	6,000	550
Iron, fine powder	Pressed	---	---	470	6,000

5.4.4. Coil Size and Number of Loops

The final design element that will determine the power output of the device is the coil. Three variables affect the coil's ability to convert magnetic flux lines into current: position of the coil relative to the flux, size of the coil, and composition of the coil. In order to maximize the number of flux lines that pass through the surface of the coil, the cross-sectional area of the coil must be positioned perpendicular to the magnetic flux lines emanating from the stator magnets. Both the cross-sectional area and the length of the coil also affect the coil's ability to conduct. Again, the surface area must be maximized, while minimizing the cross-sectional area to allow for maximum current flow (Equation 10). Finally, the coil should be composed of a metal with low resistivity (ρ). Table 5.2 gives some common materials and their associated resistivity values at 0 °C. Copper is most commonly used in large electromagnetic generators because of its low resistivity, low cost and abundance. Given the application, however, the resistivity value becomes the driving factor for selecting a material for the coil. Since both copper and gold are commonly used in MEMS devices and gold has a slightly lower resistivity, a coil made of gold should allow more current to flow.

Table 5.2: Resistivity values for common materials at 0 °C [24].

Material	Resistivity ρ (Ω -m)
Gold	1.47×10^{-8}
Copper	1.54×10^{-8}
Aluminum	2.43×10^{-8}
Beryllium	2.71×10^{-8}
Tungsten	4.82×10^{-8}
Zinc	5.59×10^{-8}

5.5. Chapter Summary

This final MFPG design combines human physiology, standard hydroelectric power generation systems, electromagnetic field theory, and MEMS fabrication techniques. It is a basic hydroelectric power system miniaturized to use a microfluid flow and modified to allow for fabrication methods and materials. It has the flexibility to allow each of the four elements of the design to be altered independently, changing the power output characteristics to meet the requirements of the device, without requiring a complete redesign.

VI. Fabrication

6.1. Chapter Overview

The process of fabricating a new device is often more difficult and time consuming than any other step in the chain. Materials must be selected, photoresist recipes must be perfected, deposition methods selected, etch rates discovered; and, with each step during the fabrication process, the probability of error increases. Out of a hundred initial test devices, only a handful might actually survive the fabrication process intact and as designed.

The fabrication of this device was no different. This chapter discusses the process of fabricating various parts of the device, the difficulties associated with the processes, and the proposed methods for fabricating the remaining portions of the device.

6.2. Glass Slides

Four packages of glass cover slides with dimensions of 22x50 mm and between 0.17 and 0.25 mm thick. These slides were chosen because they are slightly larger than the dimensions of the testing apparatus shown in Figure 2.5, and were diced to approximately 15 x 45 mm so they would fit. They were also chosen because they are sufficiently thin to make etching relatively quick, but thick enough to reduce the risk of breakage during handling. The thickness was measured on several slides and an average thickness of 0.2 mm was found, with a variance of ± 0.01 mm.

These slides were to have formed the three layers in which the microchannels, the turbine, the stator and the coil would be housed. To obtain the required depth and vertical sidewalls, an RIE etch or DRIE etch would be required, as a wet etch would etch

isotropically. Therefore, an RIE etch test was performed, using standard AFRL silicon dioxide etch recipes, to determine the etch rate of the slide using a Freon-14/O₂ gas mix. The slide was coated with 3350 photoresist approximately 4.3 μm thick, which was then removed from one end using acetone. Two Kapton photoresist dots were then applied, one to the blank slide and one to the photoresist, to help determine the total etch depth. The slide was etched for 27 minutes producing a depth of $\sim 4000\text{\AA}$ on the glass and 1.5 μm on the photoresist. This etch rate of 184 $\mu\text{m}/\text{min}$ would require an etch time of two and a half hours to etch 2 μm down.

Given this, an RIE etch of the full 200 μm slide thickness would take several days. Despite the ability to see through the slides to the rotating turbine and stator within, this makes the glass slides an impractical choice for the structural layers of the device. A cryoflourine gas mix is commonly used for DRIE etches of silicon and would easily etch through silicon structural layers at a rate of $\sim 10\text{ }\mu\text{m}/\text{min}$.

6.3. Turbine and Shaft

The turbine and shaft were to be fabricated from the backside of some available Silicon-On-Insulator (SOI) wafers. SOI was chosen because different etchants are used for silicon and silicon dioxide and the silicon dioxide would prevent the fabricated parts from being released after etching. The backside of the wafer was originally 350 μm thick, but was thinned to approximately 143 μm thick using a lapping process. Lapping a wafer is done by placing a liquid suspension on the sample and using a flat plate to apply pressure and rotate in a circular motion. These wafers were lapped at 30 rpm on a 15

inch platter using a suspension containing 5 μm aluminum oxide particles in water at a concentration of 150 g/l. The target thickness for the backside silicon layer was between 100 and 200 μm . This would allow for the thickness of the turbine, the length of the primary shaft through the structural layer and the secondary shaft that the stator will attach to.

The three steps necessary to fabricate the turbine and shaft using a cryoflourine DRIE process are shown below in Figure 6.1. The first step (a) would be to pattern the backside of the SOI wafer using the turbine mask and etch the full thickness of the silicon layer. The second step (b) would be to re-pattern the wafer using the primary turbine shaft pattern. This pattern must be etched the thickness of the silicon layer minus the required 40 μm for the turbine. Finally, the wafer must be re-patterned using the secondary turbine shaft pattern. The depth of this etch (c) is dependant upon the thickness of the coil and the stator.

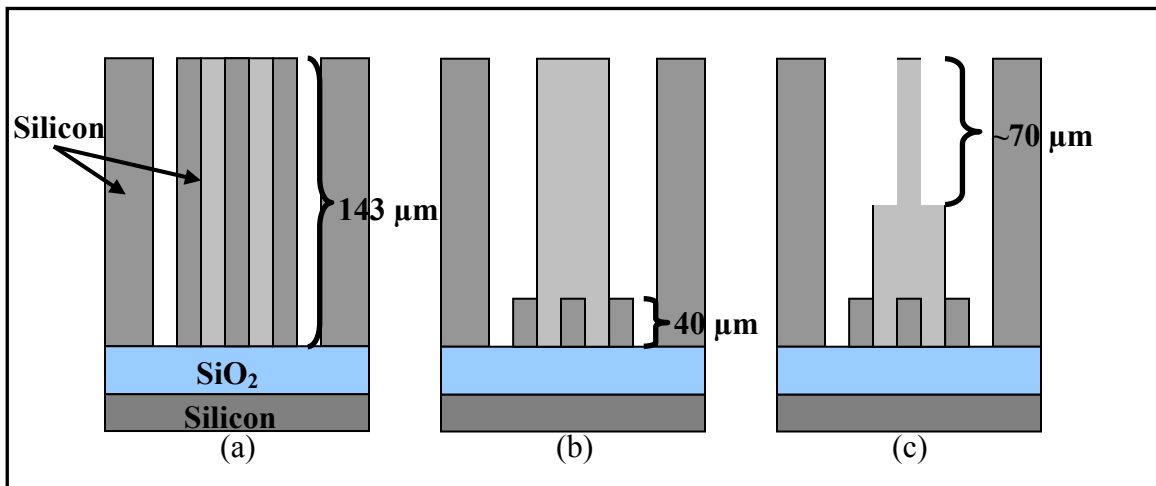


Figure 6.1: Completed fabrication steps showing the turbine etch (a), the primary shaft etch (b), and the secondary shaft etch (c).

Once the turbines were fabricated, they would need to be encapsulated to prevent them from floating away in the release etch. Figure 6.2 illustrates the steps necessary to accomplish this. First, a thick layer of photoresist was to be deposited over the turbines (a). The photoresist would be patterned to open 1 mm wide channels in a grid pattern around the turbines, exposing the silicon below (b). Si_3N_4 would then be deposited across the wafer and patterned with small 1 μm square etch holes (c). This would allow for the removal of the photoresist and the SiO_2 to release the turbines without allowing them to float away (d). Each turbine could then be accessed individually as needed by using a probe tip to peel away the Si_3N_4 above it.

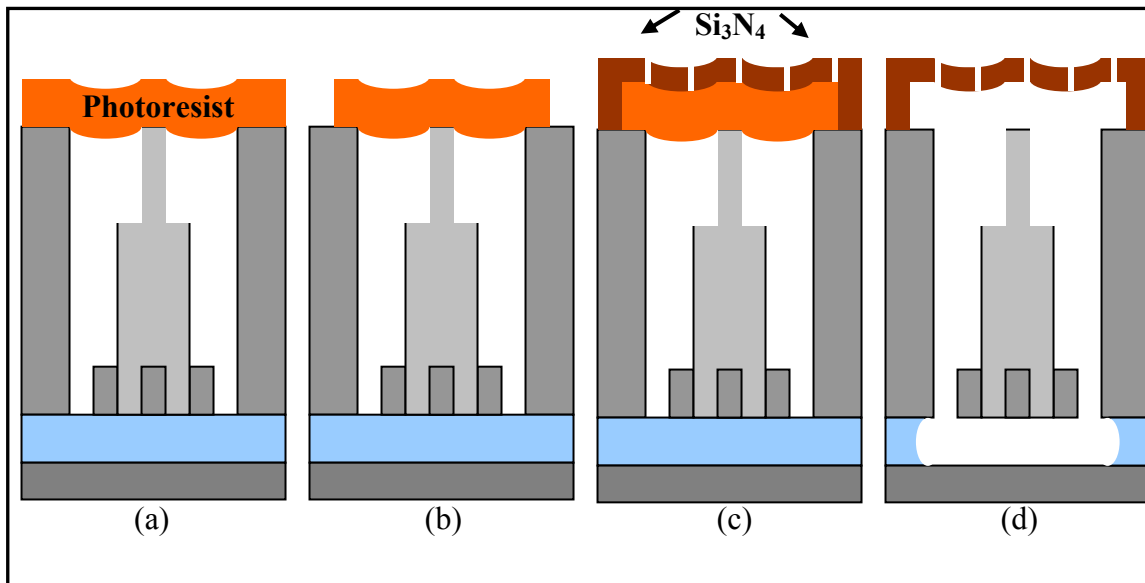


Figure 6.2: Fabrication steps necessary to encapsulate and release the fabricated turbine and shaft.

6.4. Coil

The coils were fabricated on the glass cover slips mentioned in Section 6.2. Prior to patterning, the slides underwent an initial cleaning with acetone and methanol to remove any excess material or residue and a dehydration bake for one minute at 110 °C to remove any remaining moisture that would disrupt the photoresist application process. Once they had cooled, a liberal amount of SF-11 photoresist was applied to four slides, before being spun for 30 seconds at 4000 rpm. NanoEBR was then applied to the back and sides of the slides via a cotton swab to remove any photoresist edge beading. The slides were again baked on a hotplate for two minutes at 200 °C to remove moisture and solvents from the photoresist. This spin rate and length provides an approximate photoresist thickness of 1.1 μm .

Once the SF-11 layer has been prepared, a layer of AZ5214 negative photoresist was applied to all twelve slides. The slides were again spun at 4000 rpm for 30 seconds and baked at 110 °C for 60 seconds, providing a 1.4 μm thick layer. The slides were then placed on the Karl Suss MA6 Mask Aligner and exposed to 16 mJ/cm^2 of ultraviolet light (UV). This transferred the mask image onto the AZ5214. Following the initial exposure, a post-exposure bake (PEB) was done on the slides to reverse the image. When exposed AZ5214 is baked at ~ 125 °C for two minutes, it loses its photosensitivity and effectively becomes neutral. This recipe, however, is for a standard wafer thickness of ~ 500 μm . As these substrates were only 200 μm thick, it was necessary to reduce the PEB to 110 °C for 90 seconds to ensure sufficient pattern development.

Following the PEB, a flood exposure was performed, subjecting the previously unexposed photoresist to approximately 500 mJ/cm^2 . This causes the previously unexposed areas of photoresist to become exposed and therefore vulnerable to developer. The slides were developed in a 1:5 mixture of 351 developer and deionized water (DI). A microscope and profilometer were used to examine the features to verify the designs were sharp and free of photoresist. The initial four slides then underwent a deep UV flood exposure for 300 seconds to pattern the SF-11, development in SAL101 developer for 120 seconds, six rinse cycles with DI in an automatic rinse tank, and drying with Nitrogen (N_2).

Once the slides were patterned, they were fixed to a blank silicon wafer using 1813 photoresist. This was done to facilitate the metallization process, as the slides were to be metalized in sets of four. The 1813 was spun onto the wafer at 4000 rpm for only a few seconds and the slides were immediately placed patterned-side up on the wafer. After four of the slides had been positioned on the wafer, the wafer was softbaked to remove the remaining solvent and solidify the photoresist, thus anchoring the slides to the wafer. This process was repeated for the remaining eight slides. Finally, the slides were placed in the LFE Barrel Asher for two minutes to remove any remaining photoresist within the developed pattern, leaving the finished photoresist patterns shown in Figure 6.3.

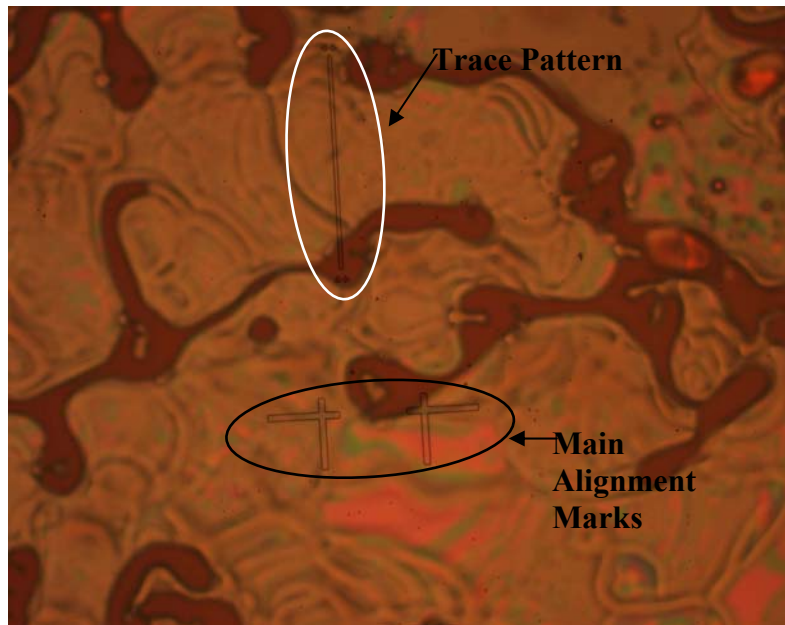


Figure 6.3: Slide pattern after ashing. Dried 1813 photoresist can be seen through the slide.

Following the initial metal deposition on the 0.25 μm and 0.5 μm thick center coil traces, the excess metal was removed via acetone bath. This also released the slides from the blank Si wafers. Some gold remained outside of the patterned areas after the initial acetone bath. The slides were then placed in an ultrasonic bath in an attempt to remove the remaining gold. Figure 6.4 shows the excess gold remaining between the coil trace on the left and the alignment marks on the right. This was a common appearance among the 0.25 μm and 0.5 μm thick traces and may have been due to insufficient photoresist thickness and over baking of the photoresist that was present.



Figure 6.4: 0.25 μm thick gold coil trace with excess gold remaining between the trace and the small alignment marks.

Following metallization of the 1.0 μm thick traces, the excess metal was removed via metal liftoff. The slides were then cleaned with acetone and placed in heated 1165 striper for two minutes to remove the SF-11 and rinsed for six cycles in an automatic rinse tank. These traces had much smoother edges than the 0.25 μm and 0.5 μm thick traces and no excess metal between the traces and the small alignment marks because of the added photoresist thickness. Figure 6.5 shows a 1.0 μm thick trace with smooth edges and sharper corners than the other thicknesses.



Figure 6.5: 1.0 μm thick coil trace with good resolution. Outline is sharp and free of excess gold.

Once the center coil traces were fabricated, a 1000 Å thick layer of silicon nitride (Si_3N_4) was deposited on all of the glass slides. This acts as a dielectric to prevent current leakage between the two layers of the coil. Once nitride was deposited on all of the slides, they were patterned using 1813 photoresist (Table C.2) and etched using a Freon-14/ O_2 RIE process.

Once the nitride was patterned, resistance measurements were taken to ensure all of the nitride had been removed from the surface of the coil traces and the window in the center of the nitride was clear. Figure 6.6 shows a profilometer measurement across the window in the nitride perpendicular to the center coil trace. It shows the full thickness of the nitride on either side of the window, the thickness of the center coil trace and the opening around the center coil trace in the nitride.

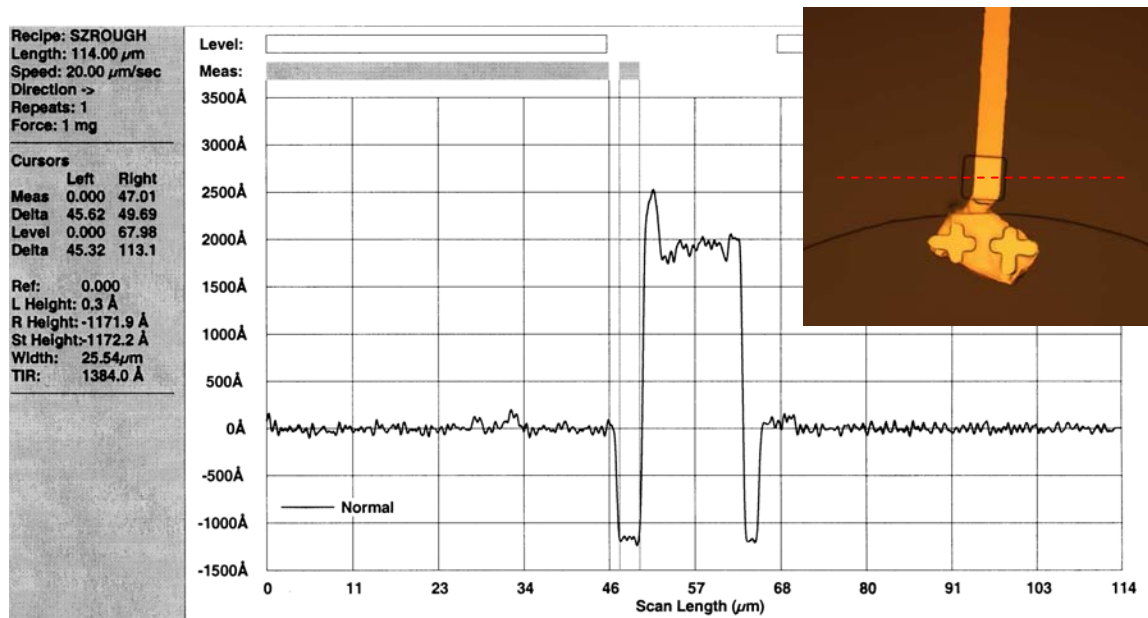


Figure 6.6: Profilometer measurement showing the profile of a 0.25 μm center coil trace through the window opened in the Si_3N_4 .

Following the resistance testing, the slides were again patterned with SF-11 and AZ5214 to pattern the gold deposition for the main coil and the contact pads. This layer of gold was deposited to thicknesses corresponding to the thicknesses of the center coil traces so that, once completed, the gold thickness would be constant on each slide from one contact pad to the other. Again, a seed layer of 200 Å of titanium was deposited to allow for adhesion to the glass and the nitride. This seed layer will affect the resistance measurements of the coil and will be discussed further in Section 7.2.1.

After the main coils were fabricated, they were again measured under the profilometer to gauge the thickness of the coils. Figure 6.7 shows the difference in thickness between the two coil layers on a 0.5 µm slide. The difference of 380 Å is due to the ion beam digging holes in the gold target during longer evaporation runs, requiring a readjustment. The beam had to be adjusted twice during this run.

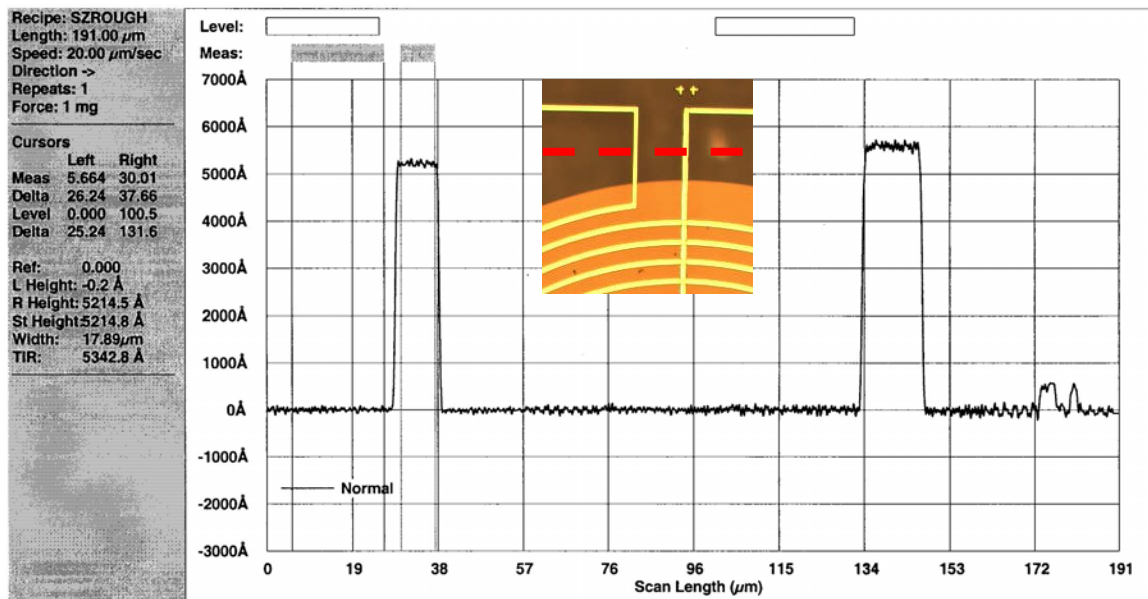


Figure 6.7: Profilometer measurement of the main and center coil traces leading to the probe pads of a coil on slide #12. Target coil thickness was 0.5 µm.

6.5. Stator

The stator was also to be fabricated from the SOI wafers described above, however they were to be fabricated from the device side of the wafer, which was 50 μm thick. This thickness was not ideal because of the resulting increased mass of the stator arms and the necessity to etch deeper into the second glass layer. Several attempts were made to reduce the thickness of the silicon layer to approximately 20 μm using the lapping process previously addressed. This proved ineffective, however, because the lapping process could not be accurately controlled over such a small thickness. After just a few rotations, grooves could clearly be seen in the silicon exposing the silicon dioxide below.

The decision was therefore made to use the full 50 μm thick layer. However, before the SOI wafers were used, a blank three inch silicon wafer was electroplated as a test, because the Ni electroplating bath being used had not been characterized. Figure 6.8 shows the setup of a typical Ni electroplating bath with the sample attached to either the anode or cathode depending on whether the sample is being added to or subtracted from.

A seed layer of 200 \AA thick chromium and 700 \AA thick copper were evaporated onto the wafer, to allow for electrical conductivity. One Kapton photoresist dot was placed on the copper seedlayer half way to the edge of the wafer. This would prevent adhesion of the nickel to this section of the wafer in the electroplating bath and, once removed after the electroplating, would allow for measurement of the electroplated nickel thickness. The wafer was then placed into the electroplating bath with a current density of 10 mA/cm^2 and an average current of 0.456 A.

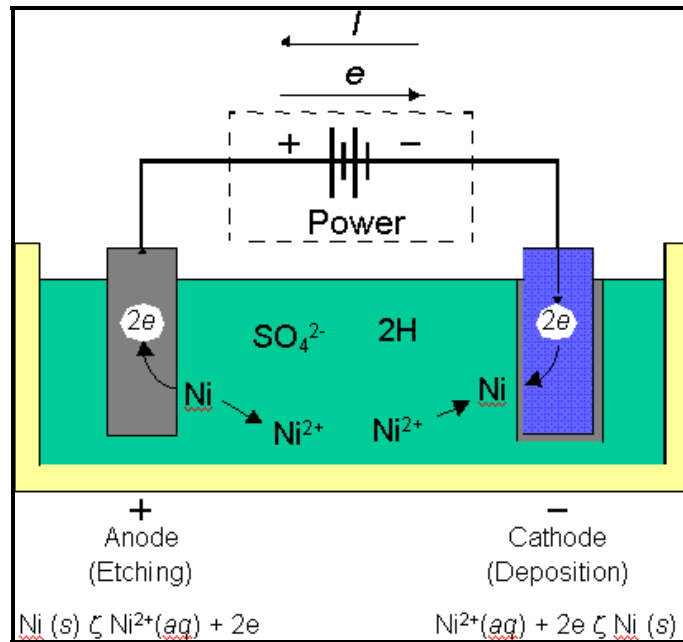


Figure 6.8: Nickel electroplating bath setup [52].

After 39.5 minutes, the wafer was removed from the electroplating bath and rinsed with DI. Delamination was clearly visible in several areas around the edge of the wafer. After the Kapton dot was removed, the wafer was dried and tested under the profilometer. The electroplated nickel was a dull brownish-grey and measured $8\text{ }\mu\text{m}$ thick from the copper seed layer where the Kapton dot was located during electroplating. The delaminated areas around the edge were shiny grey and the height difference was measured to be approximately $7\text{ }\mu\text{m}$, indicating that the seed layer and approximately $1\text{ }\mu\text{m}$ of the electroplated nickel remained. Metal lift-off methods were then applied to test the adhesion of the nickel. The nickel did not come off the wafer by this method, however, over the course of several days, the nickel continued to delaminate until only the nickel visible in Figure 6.9 remained. The nickel that delaminated over the course of

the week removed sections of substrate as it delaminated, giving the streaked, cratered appearance that now characterizes much of the wafer.

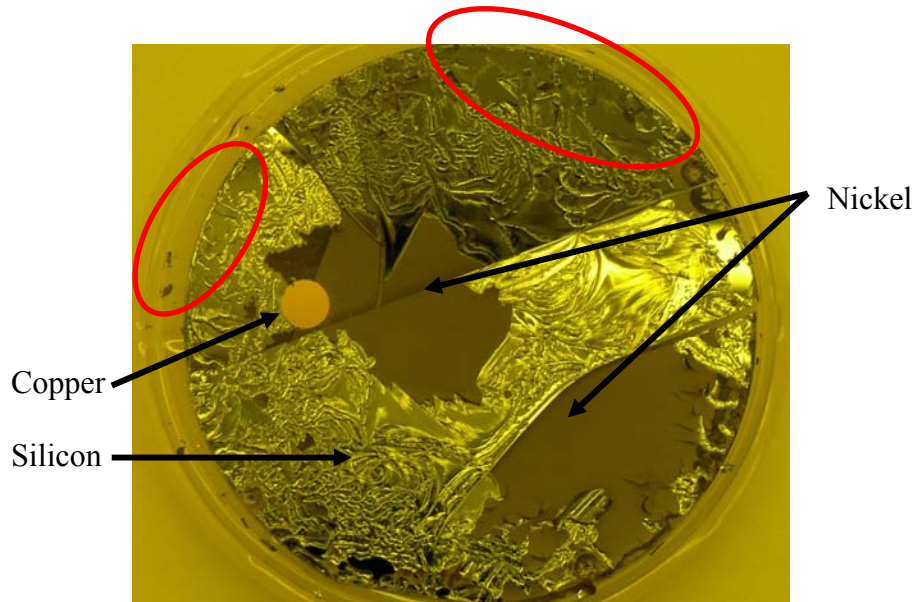


Figure 6.9: First nickel electroplating test wafer five days after electroplating. Dot on the left side of the wafer was the location of the Kapton dot and shows the copper seed layer. Circled areas show sites of initial delamination.

A second electroplating test was performed to determine if rapid cooling of the wafer caused additional tensile stress and therefore delamination of the electroplated nickel. The electroplating bath operates at 50 °C and the DI water used to rinse the wafer after electroplating is approximately 20 °C. Instead of rinsing this wafer after removal from the electroplating bath, it was placed in a beaker of DI that was maintained at 50 °C on a hotplate. The temperature was lowered at a rate of ½ °C/minute until it reached room temperature. The delamination on this wafer occurred more rapidly and more severely than with the previous test. Figure 6.10 shows the second electroplated test

wafer three days after electroplating. Again, the surface of the wafer is streaked and cratered because of delamination.

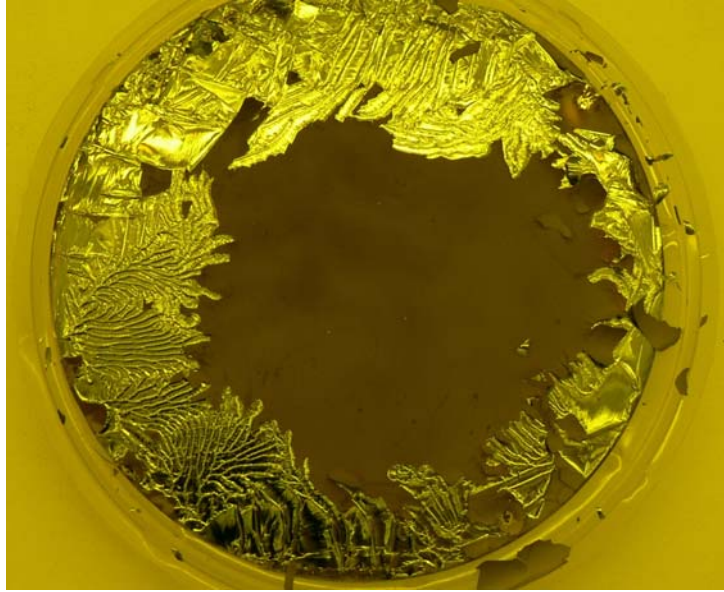


Figure 6.10: Second nickel electroplating test three days after electroplating. Slow cooling of the nickel from 50 °C caused more severe delamination.

Following the second electroplating test, it was determined that the electroplating bath did not contain any additives that are normally added to an electroplating bath to reduce the tensile stress of the nickel. Saccharin is the most common and is usually added at a concentration of 0.4 oz/gallon. Table 6.1 shows the composition of the electroplating bath with the added saccharin.

Table 6.1: Chemical composition of standard Nickel electroplating bath [53].

Chemical	Formula	Composition (oz/gal)
Nickel Sulfamate	$\text{Ni}(\text{SO}_3\text{NH}_2)_2$	11.50
Nickel Bromide	Ni Br_2	1.60
Boric Acid	H_3BO_3	5.00
Saccharin	$\text{C}_7\text{H}_5\text{NO}_3\text{S}$	0.40

6.6. Chapter Summary

Of the four portions of the device, the coil was fully fabricated, experiments were conducted for the fabrication of the stator and the microchannels and the proposed fabrication method was explained for the turbine.

At the beginning of the coil fabrication process, there were twelve slides, each with five coils, for a total of sixty coils. There were four slides, twenty coils, designated for each of the three thicknesses. Of those, only twenty-one survived the complete fabrication process to be fully tested.

The nickel electroplating tests showed that saccharin was a necessary additive to reduce the tensile stress of the electroplated nickel. It would need to be added to the bath before further fabrication of the stators could be done. Finally, etch tests showed that borosilicate glass slide covers did not make good structural layers for the device because of the slow etch rate.

VII. Analysis and Results

7.1. Chapter Overview

The most interesting part of any experiment is the data that is gathered from it, whether it validates a hypothesis or brings a new puzzle to light. Just as the fabrication process is an iterative process, so too are the results from experimentation used to refine the initial design. The results from these experiments are detailed below. They show great promise for this design, but also show where the design can be improved.

7.2. Coil

The coils were measured after each step in the fabrication process for dimensions and resistance. The dimensions of the coil traces were determined using a Tencor profilometer. Table 7.1 shows the average thickness and width of the center coil traces, grouped by target thickness, after they were fabricated. In each case, the average measured thickness was 2 - 7% thicker than the target thickness. While this does not grossly affect the characteristics of the coil, it will have a small affect on the overall resistance. The average measured width of the center coil traces was also greater than the target width, by as much as 29%. This too will have an affect on the resistance of the trace.

Table 7.1: Average thickness and width of the center coil traces after fabrication.

Center Trace Thickness (Å)	Average Measured Thickness (Å)	Average Measured Width (μm)
2500	2674	12.62
5000	5099	12.85
10,000	10375	12.88

Once the center coil traces were analyzed, the silicon nitride was deposited. After deposition, the silicon nitride was analyzed using ellipsometry and determined to be 1099 Å thick. Although this is 10% thicker than the target thickness, the additional material will only serve to increase the dielectric properties of the thin-film. The only reason to limit the thickness of the nitride layer is a potential for the gold traces deposited on top of the nitride to lose continuity as they pass over the center coil trace. Since the gold is being evaporated onto the slides, the sidewalls may become significantly thinner than the main portion of the trace, therefore increasing the resistance or even breaking the connection, as illustrated in Figure 7.1.

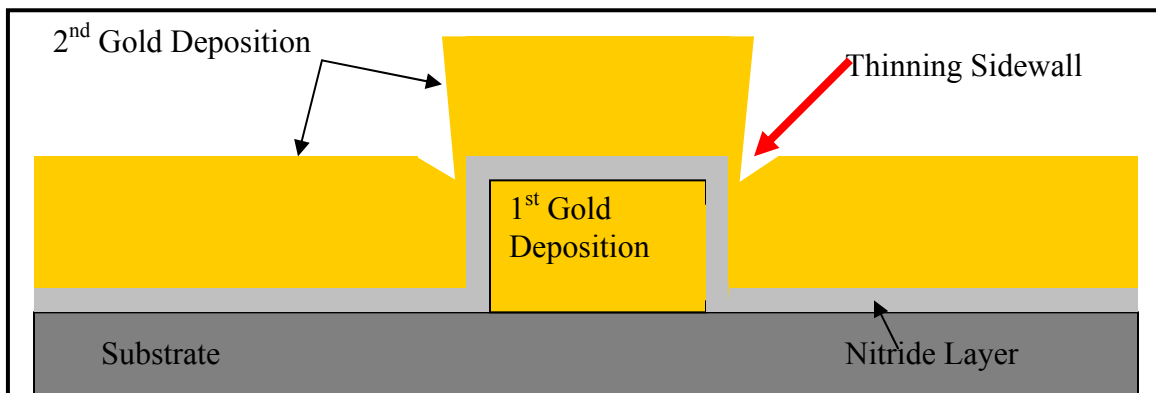


Figure 7.1: Potential thinning sidewalls created as a result of metal deposition method.

The main coil traces were characterized after deposition in the same manor as the center coil traces. Table 7.2 shows the average thickness and width of the main coil. The thickness of the coils was again greater than the target thickness in all cases, but the average width of the coils was much closer to the target width of 10 μm . This improvement may have been due to a slightly longer PEB time during patterning of the AZ5214 photoresist. Again, this will affect the overall resistance of the complete coil.

Table 7.2: Average thickness and width of the main coil traces after fabrication.

Coil Thickness (\AA)	Average Measured Thickness (\AA)	Average Measured Width (μm)
2500	2736	10.32
5000	5215	10.43
10,000	10,491	10.47

7.2.1. Coil Resistance

The resistance of each of the gold layers was measured following the profilometer measurements. Table 7.3 shows both the calculated resistance using the actual fabricated dimensions and the measured resistance of the center coil traces. The measured values for the resistance are roughly twice that of the calculated values. This is most likely due to impedance mismatch between the probes and the measuring device because the current flowing from the ohmmeter is partially reflected back to the machine, allowing less total current to flow and increasing the resistance measurement.

Table 7.3: Calculated and measured resistance of the center coil trace for each of the three thicknesses.

Center Trace Thickness (μm)	Calculated Resistance (Ω)	Measured Resistance (Ω)
0.25	5.49	10.0
0.50	2.83	5.0
1.00	1.39	3.5

Measuring the resistance of the center coils was difficult because of the relative size difference between the traces and the probe tips. Some of the traces were damaged during measurement, because it was necessary to adjust the height of the probe tips to ensure good contact with the metal. Figure 7.2 shows a 1 μm trace that was damaged during the resistance measurements.

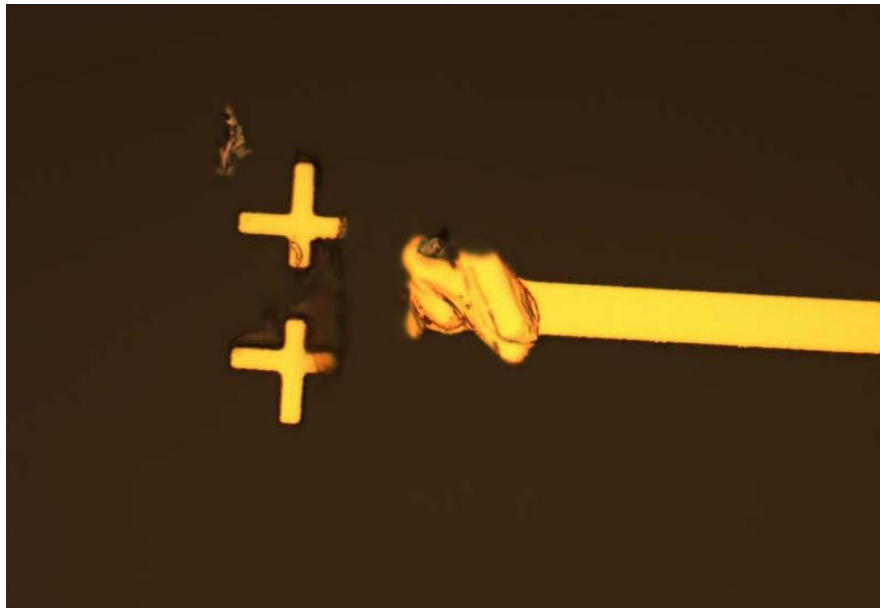


Figure 7.2: Center coil trace damaged by probe contact during resistance measurements.

Once both layers of gold were deposited, the completed coils, shown in Figure 7.3 were again measured for resistance. Table 7.4 shows both the calculated resistance values for the completed coils and the average measured values. The layer with the smaller cross-sectional area will have the higher resistance, and as the two layers of gold act like resistors in series, the dimensions of the smaller one were used to calculate the resistance. The calculated values also take into account the 200 Å thick 10 μm square layer of titanium that sits between the two gold layers where they overlap. Given that the conductivity of titanium is roughly 5% that of gold, each 10 μm square adds about 20 Ω of resistance to the overall coil resistance [54]. Combining this with the total calculated resistance of the coil made completely of gold gives the values shown below. The impedance mismatch between the ohmmeter and the probes is less significant for these measurements because of the increased length of the coil traces and therefore significantly increased overall resistance.

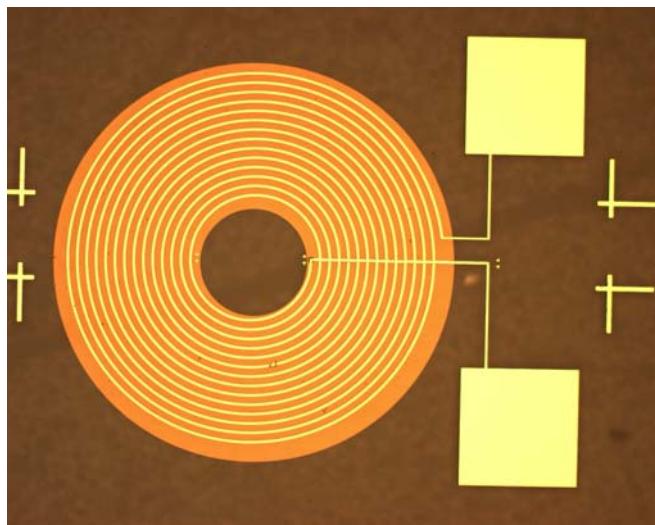


Figure 7.3: Fully fabricated coil with gold traces shown in yellow and nitride in orange.

Table 7.4: Calculated and measured resistance of the full coil trace for each of the three thicknesses.

Trace Thickness (μm)	Calculated Resistance (Ω)	Measured Resistance (Ω)
0.25	445	517.9
0.50	250	275.2
1.00	138	139.4

As predicted, the 1 μm coils have the least resistance, but they are also the closest to the calculated resistance value. This is potentially due to the sidewall thinning mentioned above. Scanning Electron Microscope (SEM) pictures of the overlap were attempted, but resolution was too poor to determine whether sidewall thinning was present. This lack of resolution was due to electrical charging of the coil and caused the electron beam to continually drift and jump at settings as low as 2 kV and 1 μA . At higher energy settings, the image was completely distorted by the electrical field generated by the interaction of the coil and the electron beam.

Table 7.5 shows the measured dimensions of the coil traces on slide #5 with the calculated cross-sectional area and the measured resistance values for each coil. Resistance should be inversely proportional to the cross-sectional area, so as the cross-sectional area decreases, the resistance should increase. The values do not strictly follow this behavior. Trace 5 has the largest cross-sectional area, but has the second largest resistance, and Trace 4, which has the smallest cross-sectional area, should have the largest resistance but has one of the smallest. Rather, their behavior seems more dependant on the thickness of the traces and almost independent of the width. Trace 3,

for instance, is the thinnest trace and has the largest resistance value. Similarly, Trace 2 is the thickest of the traces and has the lowest measured resistance. The measured resistance values shown below would be more consistent with traces between 2350 and 2450 Å, given the measured widths. This is consistent with the theory regarding thinning sidewalls of the main traces.

Table 7.5: Cross-sectional area and resistance values for the coils on slide #5.

	Trace 1	Trace 2	Trace 3	Trace 4	Trace 5
Height (Å)	--	2728.4	2672.8	2721.5	2688.0
Width (µm)	--	10.54	10.54	10.04	11.03
Cross-Sectional Area (µm ²)	--	2.876	2.817	2.732	2.965
Measured Resistance (Ω)	--	488	506	496	500

One method to alleviate this potential problem would be to etch the substrate the exact size, shape, and thickness of the center coil trace prior to any deposition. Once the etch is accomplished, the center coil trace can be deposited. A quick dip in a Buffered Oxide Etch (BOE) solution should remove any excess gold that remains above the plane of the substrate creating a relatively smooth surface for the nitride and the second gold layer to be deposited on.

7.2.2. Current Carrying Capacity

Voltage was applied to each coil to determine the amount of current flow through the device and to determine if the current flow had detrimental effects on the structure of

the coil. The voltage was increased from 1 to 6 V in 1-V increments. The coils behaved as predicted, with no burnouts or glowing. The 1 μm traces allowed an average of 40 mA to flow given a 6-V bias, significantly higher than any theoretical voltage or current that the final device could produce. Similar results were seen with the 0.5 μm and 0.25 μm traces, each flowing an average of 21 mA and 12 mA, respectively. Exact data points and graphs are located in Table D.7-12 and Figure D.1-6.

7.3. Stator

7.3.1. Deformation Due to Strain

As previously stated, the nickel electroplating bath that was used for these experiments was not in common use and had not been properly characterized. As such, it was not determined until after the initial two test runs that the bath did not contain the necessary additive to reduce the tensile strain of the nickel as it was being deposited.

The second test wafer was measured with a profilometer to determine the thickness of any remaining nickel on the substrate. Figure 7.4 shows the second electroplated test wafer and Figure 7.5 shows the resulting trace, which indicates that as the nickel delaminated, it removed large sections of the silicon substrate more than 40 μm deep. The red dashed line indicates the original surface of the silicon wafer. These results indicate that slow cooling of the nickel seems to have the opposite effect of that which was expected.

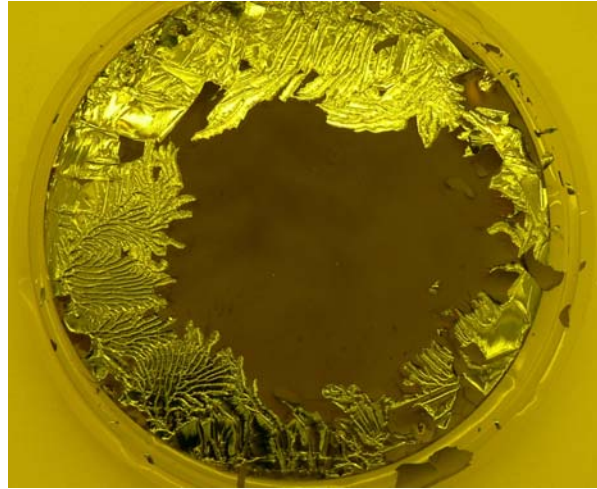


Figure 7.4: Second attempt at nickel electroplating. Tensile strain caused the nickel delamination to remove sections of substrate up to 30 μm deep.

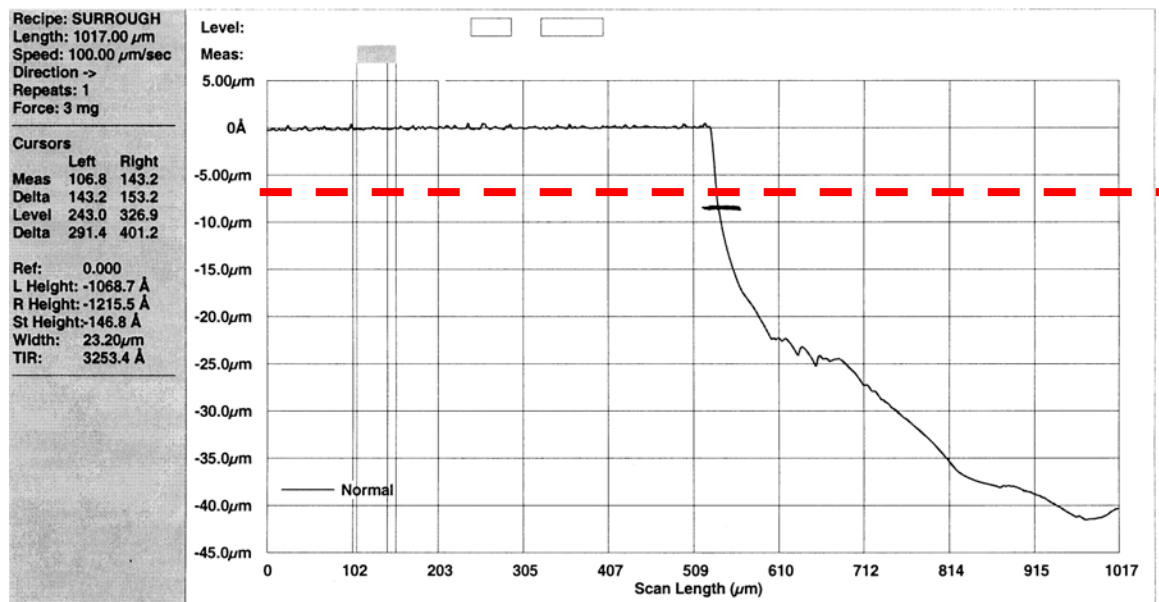


Figure 7.5: Profilometer measurement of second electroplating test wafer after cooling. Ni layer was 8 μm thick, seed layers comprised 0.1 μm in thickness. Red dashed line indicates original surface of the silicon substrate.

7.3.2. Magnetization

After the nickel was electroplated onto the second test wafer, it continued to delaminate until only about 1/3 of the nickel remained on the substrate. To test for basic magnetization, a magnet was placed in contact with the remaining nickel, as shown in Figure 7.6a. This caused the remaining nickel to become magnetically polarized. Once polarized, it would require a magnetic field strength in the opposite alignment of 55.7 H or a temperature increase above the Curie temperature of 627 K to return the net magnetization of the nickel to zero. When the magnet was removed, and again placed in proximity to the nickel, the behavior was very similar to the behavior of two magnets. If the magnet was aligned with the nickel as it had been when initially placed on the nickel, it caused the nickel to move slightly. However, if it was aligned opposite, the attraction between the nickel and the magnet would cause the 500 μm thick, 3" wafer to lift off of the desk, as shown in Figure 7.6b.

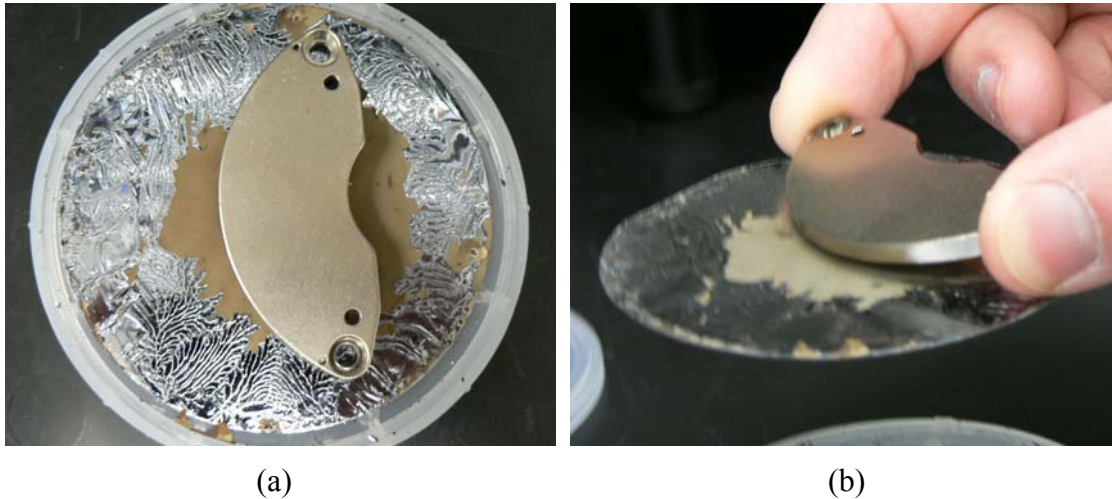


Figure 7.6: Magnetization (a) of the electroplated nickel and magnetic attraction (b) lifting the substrate.

7.4. Chapter Summary

The results presented in this chapter have helped to validate the theoretical calculations put forth in Chapter 4. The coil behaves as predicted, with the exception of the additional resistance caused by the titanium seed layer that is a necessary fabrication step. This seed layer should be taken into consideration for the next design. Sidewall thinning must also be considered before the next design revision.

The experiments with the nickel electroplating have validated the ability of the electroplated nickel to become magnetized and maintain a strong magnetic field. They also showed that tensile stress must be compensated in the electroplating bath or the nickel will destroy the substrate it is deposited on.

Finally, the test results for the etch tests of the borosilicate glass slide covers have shown that it can be done, but a different choice of substrate, such as silicon or sapphire would allow for faster and easier etching of the deep channels and the through-substrate holes.

VIII. Conclusions and Recommendations

8.1. Chapter Overview

No great project is ever truly finished, only abandoned. Improvements can be made even to the pinnacle of perfection, because the purpose of the project can change. This chapter will provide a final review of the progress of this project, along with a synopsis of the scientific contributions from this research in the areas of BioMEMS and electromagnetics. Finally, recommendations for future research in this area will also be summarized.

8.2. Thesis Review

Chapter one of this thesis reviewed the need for a self-sustaining power source that could be implanted within the human body to power life-sustaining medical devices. It briefly described the current capabilities in the areas of MEMS, microfluidics and BioMEMS and proposed a solution for the need of a power source.

Chapter two reviewed current research into microfluidics and electromagnetic power generation in MEMS devices and compared them with this proposed research. It showed that although research has been done in this area, the devices theorized were several orders of magnitude too large to be used in the proposed manor.

Chapter three reviewed the underlying theory behind the proposed device, including basic fluid flow mechanics, the behavior of fluid flows in microchannels, and energy transfer from mechanical to electrical.

Chapter four mathematically verified that it is possible to extract usable amounts of electrical energy by using the blood flow through human capillaries to rotate a micron scale turbine generator. The calculations for pressure in human capillaries was used to

determine the dimensions for the microchannels and the turbine, while the calculations for the magnetic field generated for a give sample of nickel helped determine the dimensions of the stator and the coil.

Chapter five described the designs that were created and why they were refined down to a single design with four independent parts that could be fabricated using conventional MEMS fabrication techniques and assembled.

Chapter six described the fabrication process for the induction coils. It also described the experiments that were begun on fabrication techniques for the stators and the structural layers and theoretically explained the fabrication process for the turbine, as the process is routinely done during MEMS fabrication.

Chapter seven described the results of the experiments run on the coils and the electroplated nickel, and describes how they compared to the predicted results.

8.3. Scientific Contributions

Although small electromagnetic generators have been theorized and fabricated, none has been as small as the MFPG device and all contain pieces of naturally occurring magnetite (Fe_3O_4) which must be physically inserted into the device after fabrication. As such, this is the first device of its size, and the first to use nickel, deposited during device fabrication, as the source of the magnetic field.

8.4. Recommendations

As this part of the project comes to a close, I would like to leave some parting thoughts to any who may continue in this research. Below are my thoughts on what can be done to improve the current device and additional projects that could be integrated with the MFPG device to provide a complete system.

8.4.1. Continuation of Power Generation Evaluation

The results of the calculations and experiments undertaken as part of this thesis, show great potential for the device. The continuation of research in this area should focus on fabrication methods and modifications to the design. Since each of the critical parameters of this device effects the overall power output of the device, there are a myriad of potential modifications that can be made to the design to alter the frequency, voltage, and current of the output. Continued experimentation using different dimensions would help to determine the limits of the output characteristics.

8.4.1.1. Variations in Turbine Shape and Position

As discussed in Section 2.3, impulse turbines have a W-shaped bucket to more effectively capture the energy of the fluid flow. It is unknown whether this modification would have any effect on the microturbine, both because of the scale and because the turbine is submersed in the fluid.

One potential method for creating these W-shaped buckets on this scale would be to isotropically etch pits into the top of a wafer to form the buckets. A thin strip of gold could then be deposited on one half of the collar leading from the buckets to the main body of the turbine. Figure 8.1 shows this design both before and after the release. Once the device is released, the stress differential between the half of the collar with gold and the half of the collar without should cause the collar to twist, leaving the buckets at an angle to the main body of the turbine. The specific dimensions of the deposited gold would determine the exact angle.

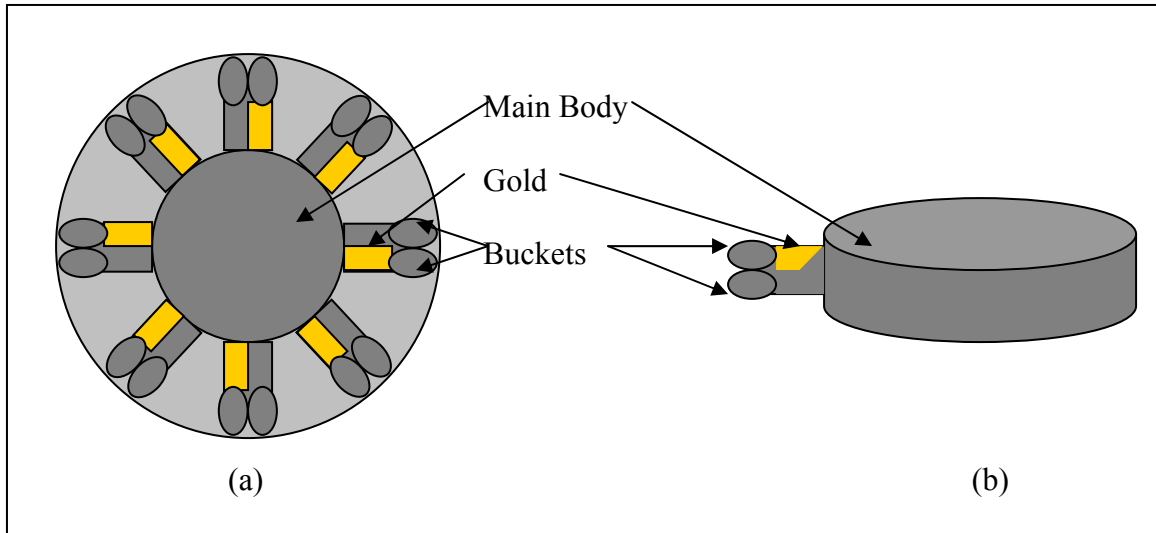


Figure 8.1: Potential design of microturbine with w-shaped buckets before release (a) and after release (b).

Also, as the calculations in Chapter 4 indicated, the closer the turbine is to the source of the microfluidic flow, the more pressure the fluid will have, and thus the faster the turbine should spin. Placement within the microchannel is therefore crucial to determining the frequency of the power generated by this device.

8.4.1.2. Variations of coil and stator dimensions

As the calculations in Section 4.2.3 show, the two critical factors that determine the magnitude of the power output from this device are the dimensions of the coil and the stator. The coil is responsible for allowing current to flow while the stator is responsible for generating the magnetic field that causes the current to flow. The smaller the cross-sectional area of the coil, the less resistance it will offer and therefore the more current will flow. The length of the coil acts just the opposite; the longer the coil, the higher the resistance. For the stator, the magnetic field generated by several atoms of a material is larger than the sum of the individual fields. This means the more mass, the larger the

magnetic field will be. Again, these should be adjusted to fit the requirements of the device that is being powered.

8.4.2. Examination of Alternate Power Generation Designs

This design uses an internal turbine to turn the stator and thus generate power. Other designs could be created to make use of a fluid flow outside of the device, more like a water wheel at an old mill. This would preclude the need for microchannels and could be used in larger areas such as inside the heart or the larger blood vessels.

Another alternative to either of these designs may be to use the same design for the power generation, but have several coil/stator sets tied together in series or parallel to alter the power output beyond the values attainable by simply altering the dimensions of a single coil/stator set.

8.4.3. Energy Storage Capabilities

Regardless of the design used to generate the power, there is still a need to regulate and store the power to ensure a constant level of output. Research needs to be done to design a system that could be integrated with the energy production system to provide a well regulated output for use in the rest of the system. This includes voltage and frequency regulation as well as energy storage, which may be feasible using arrays of micron-sized capacitors.

8.4.4. Integration of Probes and Control Circuitry

The probes used to monitor the contents of the fluid need to be designed such that they can be fabricated with the rest of the device. The same is true of the control circuitry that should be able to monitor the signals from the probes and convert it to a

transmittable signal. The design of this circuitry will depend greatly on the power available and the desired output signal characteristics.

8.5. Conclusions

With so many applications and the potential to increase the quality of life for so many people, it is only logical to conclude that additional research must be done in this area. In addition, the scientific knowledge gained by research into the properties of electromagnetic fields on this scale may increase our understanding of electromagnetic field theory.

Appendix A: Mathematica Code

This appendix contains the Mathematica code used for the calculations in Chapter IV. It includes calculations for fluid flow rates, both for blood through human capillaries and water through the MFPG microchannels, fluid pressure in the microchannels and the rate of rotation of the turbine for various pressures.

```

Fluid Flow Calculations -- Blood in a Human Capillary

This Mathematica code calculates the fluid flow rate for blood in an
average size human capillary

Basic equation and parameters :


$$Q = \frac{\pi r^4}{8 \eta L} \Delta P$$
 (*Basic Fluid Flow Calculation for Microfluidics*)

 $\eta = 0.0027;$  (*N-s/m2*) (*Viscosity of Blood*)
 $r = 5;$  (* $\mu m$ *) (*Standard Capillary Radius*)
 $L = 500;$  (* $\mu m$ *) (*Length of Capillary*)
 $\Delta P = 3333.05;$  (*N/m2*) (*Change in Pressure over Capillary Length*)

Calculations :


$$Q_m = \frac{\pi r^4}{8 \eta L} \Delta P$$

605.966.


$$Q_m = 6.05966 \times 10^{-5} \text{ (}\mu m^3 / s\text{)}$$



$$Q_1 = Q_m \times 10^{-12}$$


$$6.05966 \times 10^{-7}$$



$$Q_1 = 6.06 \times 10^{-7} \text{ mL / s}$$



$$Q = Q_1 \times 60$$

0.0000363579


$$Q = 0.0000364 \text{ mL / min}$$


The flow rate for blood through an average human capillary should be
0.0000364 mL / min.

```

Figure A.1: Mathematica code used to determine the flow rate of blood through human capillaries.


```

Pressure Calculations -- Blood in Ideal MFPG device

This Mathematica code calculates the pressure of blood at the opening to
the turbine cavity in an ideal (implantable) MFPG device

Basic equation and parameters :


$$Q = \frac{\pi r^4}{8 \eta L} \Delta P$$
 (*Basic Fluid Flow Calculation for Microfluidics*)


$$P_{\text{Outlet}} - P_{\text{Inlet}} = \frac{Q 8 \eta L}{\pi r^4}$$
 (*Pressure Calculation for Microfluidics*)

 $\eta = 0.0027;$  (*N-s/m2*) (*Viscosity of Blood*)
 $r = 5;$  (* $\mu\text{m}$ *) (*Standard Capillary Radius*)
 $L = 500;$  (* $\mu\text{m}$ *) (*Length of Capillary*)
 $P_{\text{Inlet}} = 5332.9;$  (*N/m2*) (*Pressure at the Arteriolla end*)
 $Q = 6.05966 \times 10^5;$  (* $\mu\text{m}^3/\text{s}$ *) (*Flow Rate from Capillary Blood Calc*)

Calculations :


$$\Delta P = \frac{8 \eta L}{\pi r^4} Q$$


3333.05

 $\Delta P = P_{\text{Inlet}} - P_{\text{Outlet}}$ 

 $P_{\text{Outlet}} = P_{\text{Inlet}} - \Delta P$ 

1999.85

 $P_{\text{Outlet}} = 2000 \text{ N/m}^2$ 

```

Figure A.2: Mathematica code used to determine the pressure at the opening to the turbine cavity in the ideal MFPG device using blood as the fluid.

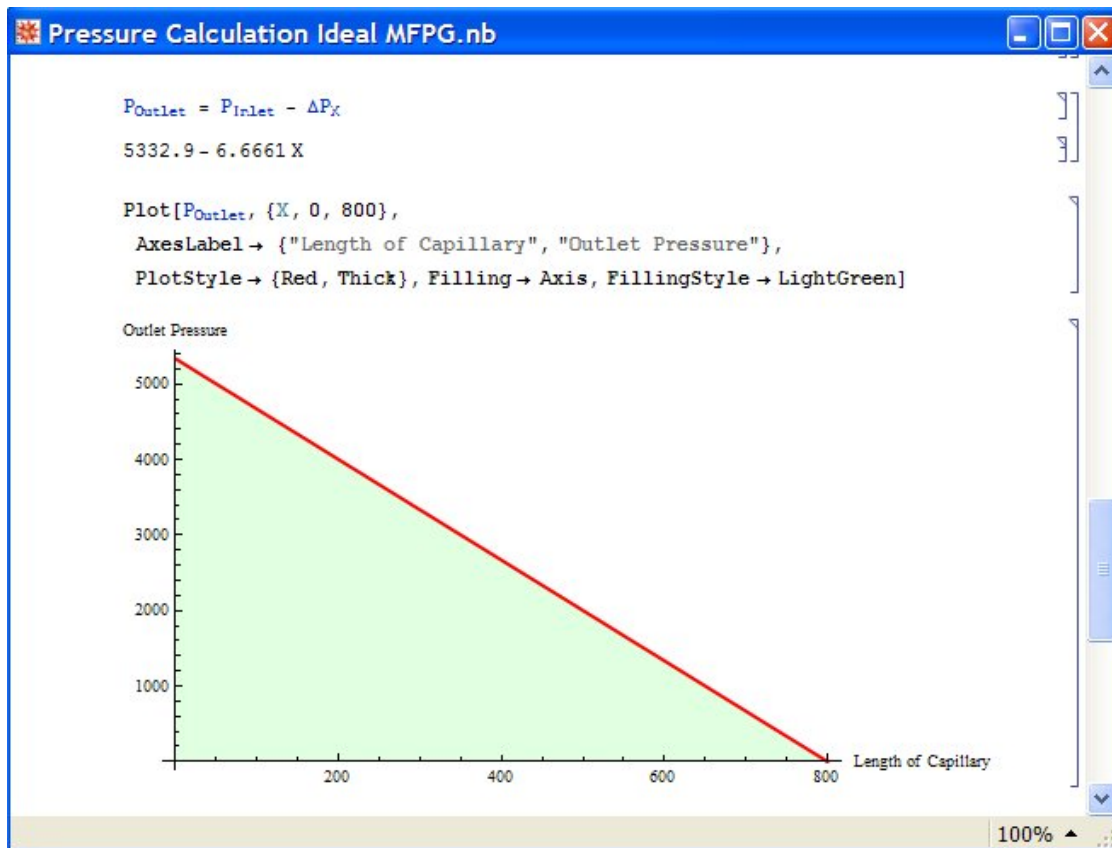


Figure A.3: Mathematica code and graph illustrating the relation between capillary length and outlet pressure. Note that for blood flowing through a capillary with a 5 μm radius and an initial pressure of 5332.9 N-m, the cut-off length is 800 μm . Beyond this length, adhesive and cohesive forces within the blood will counteract the initial pressure and the blood will not flow.

```

Fluid Flow Calculations -- Water in Fabricated MFPG Device

This Mathematica code calculates the fluid flow rate for water in the
microchannels of the fabricated MFPG device

Basic equation and parameters :


$$Q = \frac{\pi r^4}{8 \eta L} \Delta P$$
 (*Basic Fluid Flow Calculation for Microfluidics*)


$$Q_r = \frac{h^2 w^2}{8 \eta L} \Delta P$$
 (*Fluid Flow Calculation for rectangular microchannel*)

 $\eta = 0.001;$  (*N-s/m2*) (*Viscosity of water*)
 $h = 40;$  (* $\mu m$ *) (*height of microchannel*)
 $w = 40;$  (* $\mu m$ *) (*width of microchannel*)
 $L = 20000;$  (* $\mu m$ *) (*Length of Capillary*)
 $P_{Inlet} = 5332.9;$  (*N/m2*) (*Pressure at the Arteriollle end*)
 $P_{Outlet} = 2000;$  (*N/m2*) (*Pressure at the turbine end*)

Calculations :

 $\Delta P = P_{Inlet} - P_{Outlet}$ 
3332.9


$$Q_r = \frac{h^2 w^2}{8 \eta L} \Delta P$$

 $5.33264 \times 10^7$ 

 $Q_r = 5.333 \times 10^7 (\mu m^3 / s)$ 

 $Q_1 = Q_r \times 10^{-12}$ 
0.0000533264

 $Q_1 = 5.333 \times 10^{-5} mL / s$ 

 $Q_w = Q_1 \times 60$ 
0.00319958

 $Q = 0.0032 mL / min$ 

```

Figure A.4: Mathematica code used to calculate the rate of water flowing through the microchannels of the fabricated MFPG device. The pressure at the inlet is matched to human capillary arteriollle pressure and the outlet pressure is matched to that calculated for the ideal MFPG device.

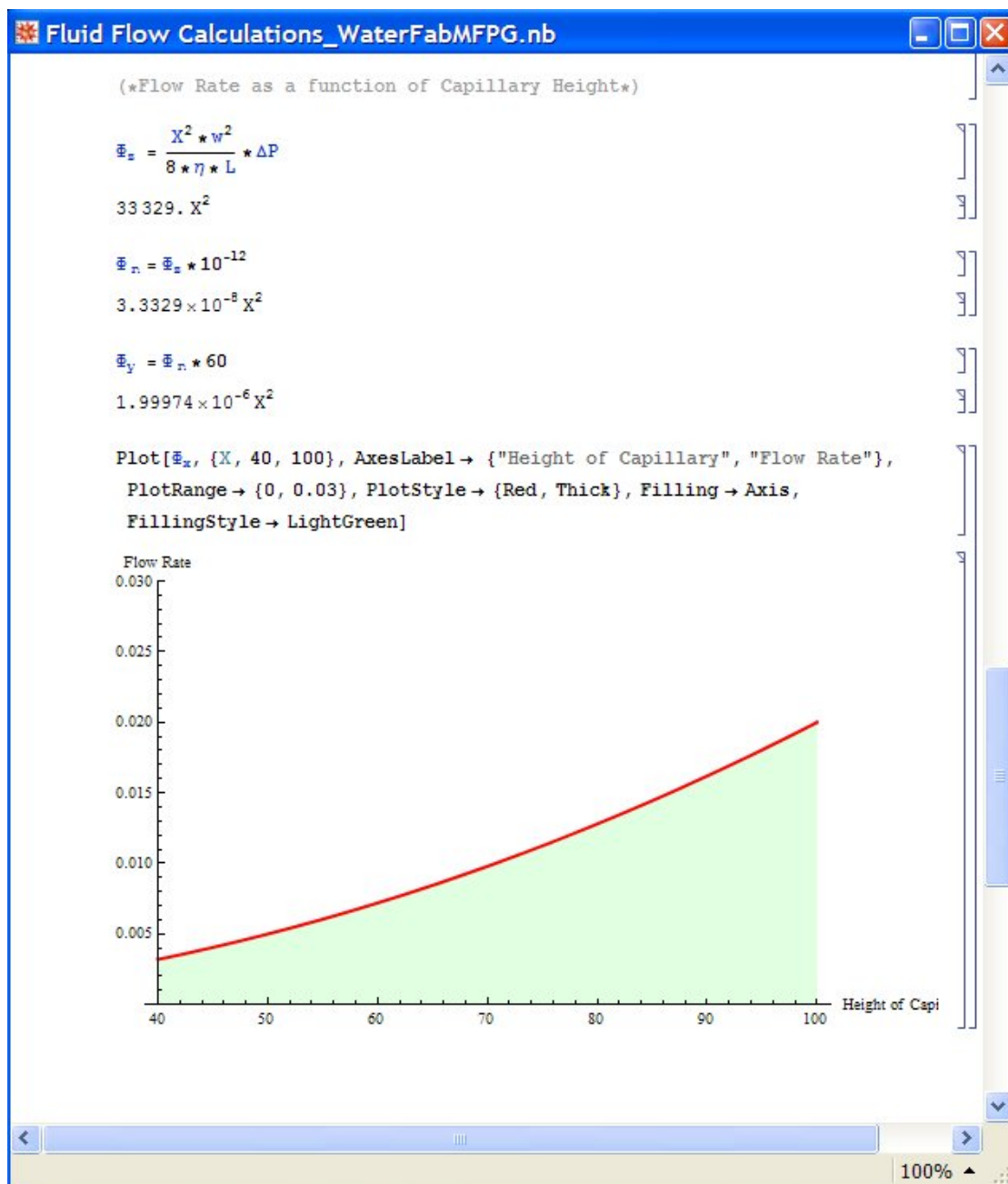


Figure A.5: Mathematica code and graph used to illustrate the rate of water flow through the fabricated MFPG microchannels as a function of capillary height.

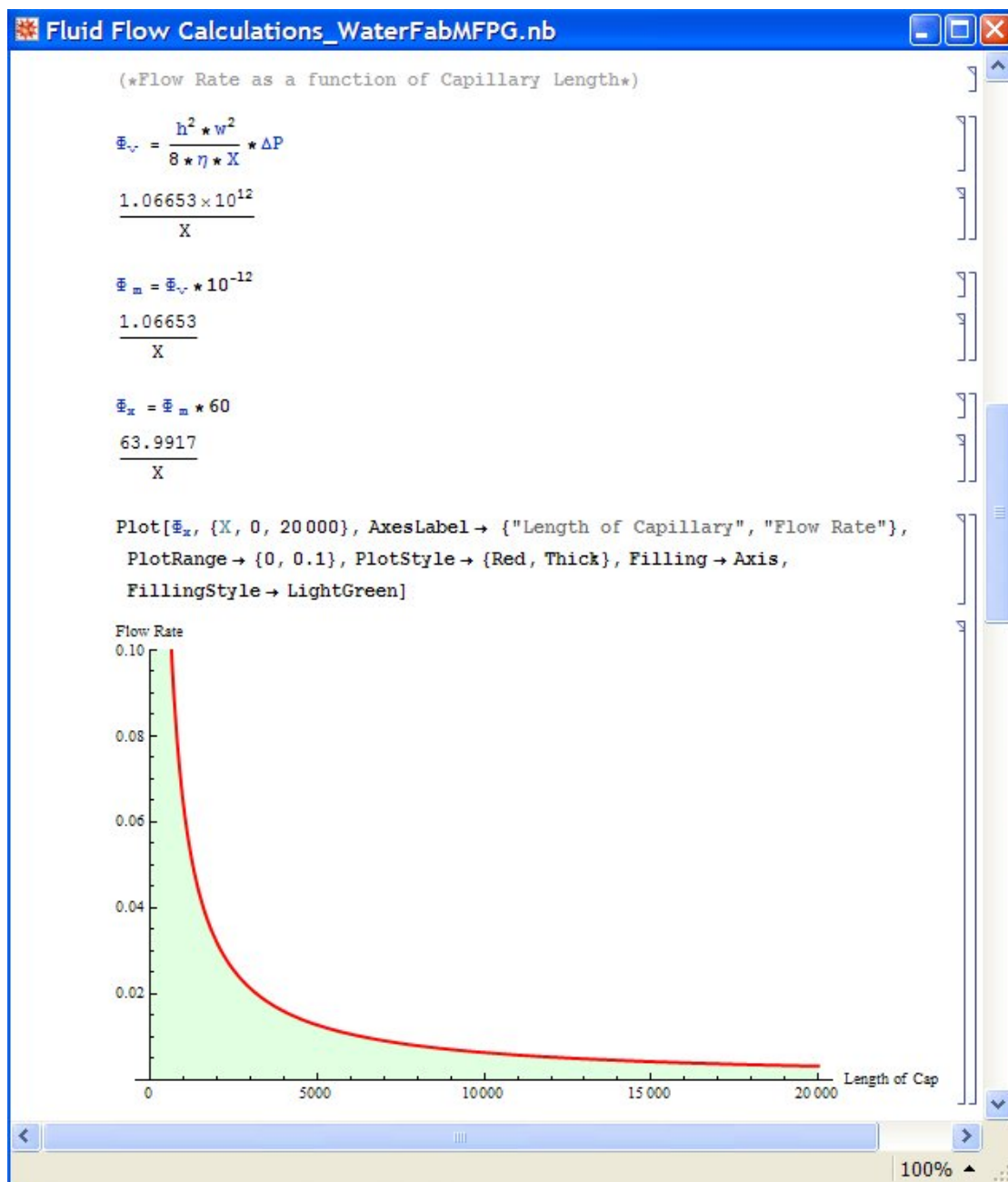
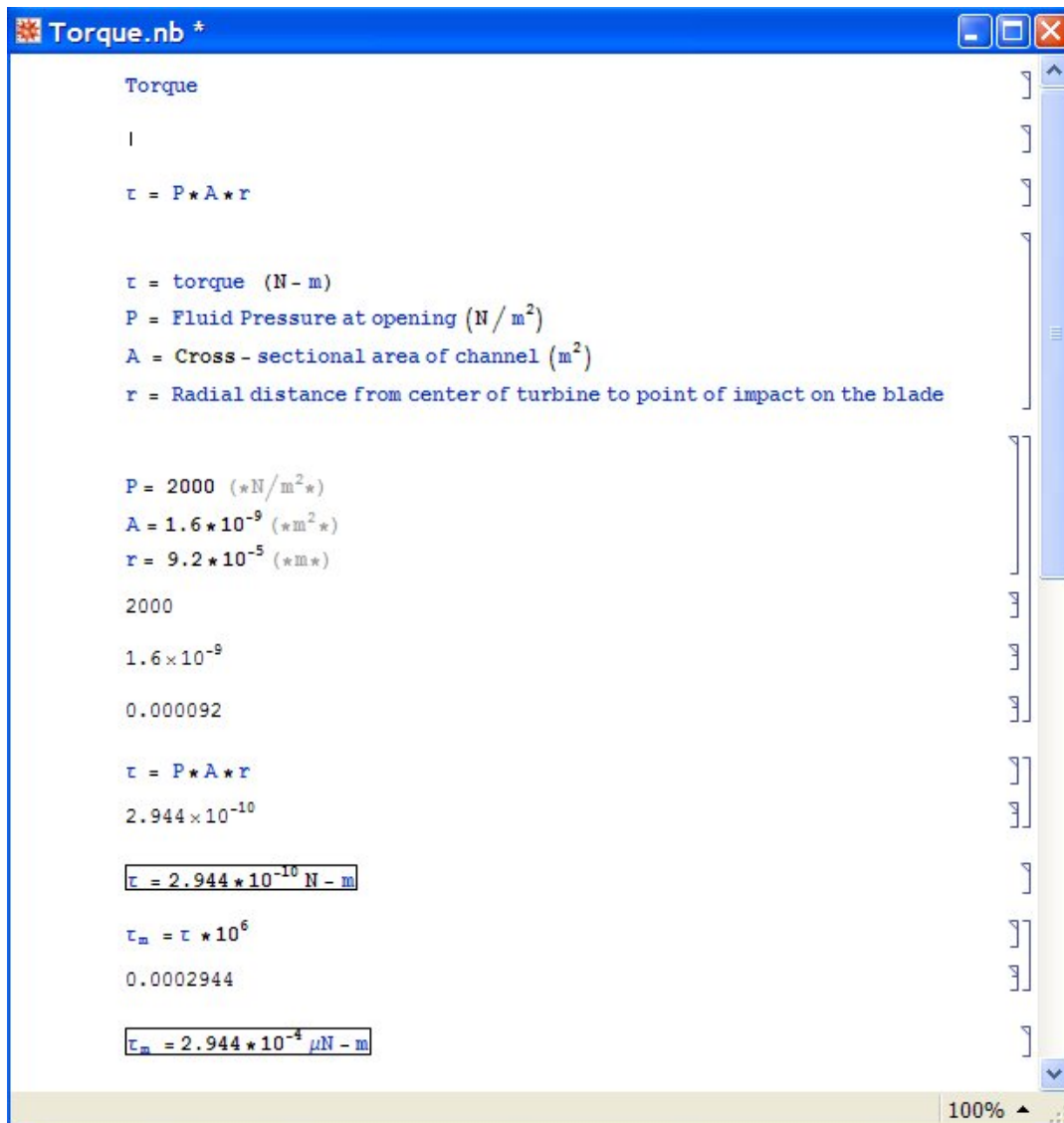


Figure A.6: Mathematica code and graph used to illustrate the rate of water flow through the fabricated MFPG microchannels as a function of capillary length.



```

Torque

|

τ = P*A*r

τ = torque (N-m)
P = Fluid Pressure at opening (N/m²)
A = Cross-sectional area of channel (m²)
r = Radial distance from center of turbine to point of impact on the blade

P = 2000 (*N/m²*)
A = 1.6*10⁻⁹ (*m²*)
r = 9.2*10⁻⁵ (*m*)

2000

1.6*10⁻⁹

0.000092

τ = P*A*r

2.944*10⁻¹⁰

τ = 2.944*10⁻¹⁰ N-m

τ_m = τ * 10⁶

0.0002944

τ_m = 2.944*10⁻⁴ μN-m

```

Figure A.7: Mathematica code used to calculate the torque applied to the turbine, by the fluid pressure at the opening to the turbine cavity, in the fabricated MFPG device.

```

Angular Velocity RPM.nb

Angular Velocity and RPM


$$\omega = \frac{V_{\text{Perp}}}{r}$$


 $\omega$  = Angular Velocity
 $V_{\text{Perp}}$  = Velocity of fluid perpendicular to the radius of rotation
r = radius

|

r = 9.2 * 10-5; (*m*)
 $\Phi$  = 6.05966 * 105; (* $\mu\text{m}^3/\text{s}$ *) (*Flow Rate from Capillary Blood Calc*)
A = 1.6 * 10-9; (*m2*)
(*Cross-sectional Area of channel*)

 $V_{\text{Perp}} = \Phi / (A * 10^{12})$ 
378.729

 $V_{\text{Perp}} = 378.729 \mu\text{m} / \text{s}$ 

 $\omega = \frac{V_{\text{Perp}}}{r * 10^6}$ 
4.11662

 $\omega = 4.12 \text{ Rad} / \text{s}$ 

 $f = \frac{\omega}{2 \pi}$ 

0.65518

RPM = f * 60
39.3108

RPM = 39.3 Revolutions per minute

```

Figure A.8: Mathematica code used to calculate the angular velocity of the turbine in the fabricated MFPG device as a function of the ideal fluid flow rate.

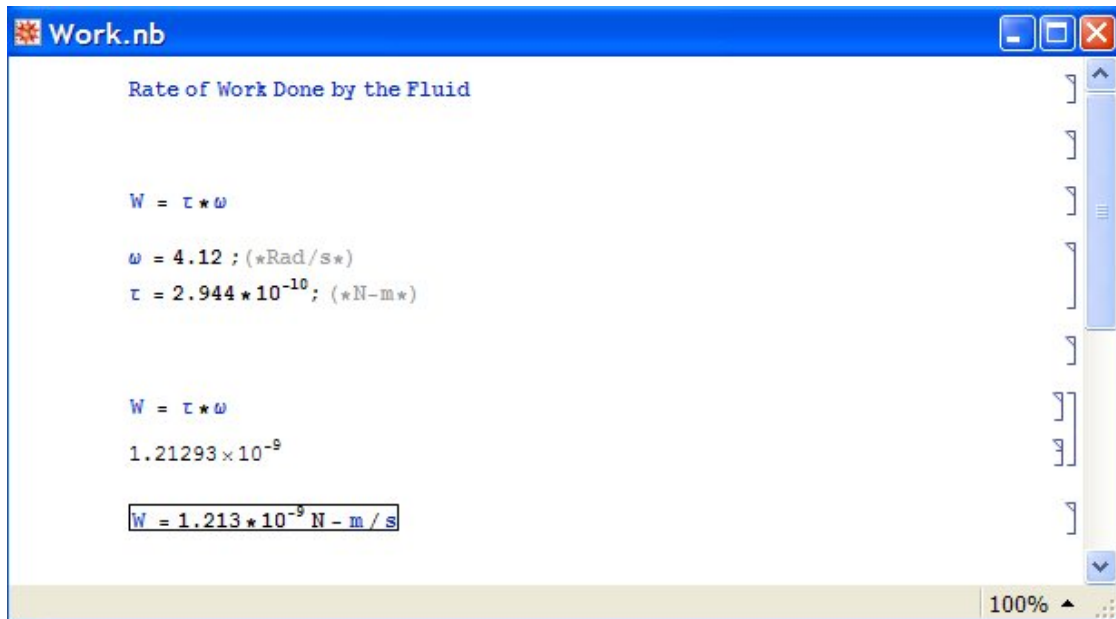


Figure A.9: Mathematica code used to calculate the rate of work done on the turbine by the fluid in the fabricated MFPG device.


```

Magnetic field strength

1 gauss = 0.0001 Wb / m2 (Teslas)
1 Wb = 1 T * m2

Flux Density of Nickel

Φ = B * A
(*Assuming Cross-sectional area is perpendicular to the
magnetic field*)

ΦNi-g = 0.40; (*Wb / m2*)
WM = 80 * 10-6; (*m*)
HM = 20 * 10-6; (*m*)
WC = 10 * 10-6; (*m*)
HC = 2 * 10-6; (*m*)

ΦNi = ΦNi-g * WM * HM
6.4 * 10-10

ΦNi = 6.4 * 10-10 Wb

BA =  $\frac{\Phi_{Ni}}{W_C * H_C}$ 
32.

B = 32 Teslas

Using the maximum theoretical magnetic flux density,
the magnetic field produced by each stator arm should be 32 Teslas.

```

Figure A.10: Mathematic code used to calculate the magnetic field strength produced by the stator arms on the coil. Note that the magnetic field strength was calculated for stator magnet height of 20μm.

```

Current Flow.nb

Theoretical Current

|

This calculation uses the Ampere -
Maxwell Law to determine the theoretical current that can be
generated by the MFPG device.

μ₀ = 1.25664 * 10⁻⁶; (*H/m = Wb/A-m*)
κₘ = 600; (*μ/μ₀*)
| B | = 32 (*T=Wb/m²*)
Wc = 10 * 10⁻⁶; (*m*)
Hc = 2 * 10⁻⁶; (*m*)

∇ × B = μ₀ J

∇ × B = 
$$\begin{vmatrix} \hat{i} & \hat{j} & \hat{k} \\ \frac{\partial}{\partial x} & \frac{\partial}{\partial y} & \frac{\partial}{\partial z} \\ 0 & (-32 z) & 0 \end{vmatrix} = 32 \hat{i} \text{ (*Wb/m³*)}$$


J = 
$$\frac{32}{\mu_0 * \kappa_m}$$

42441.2

J = 2.54647 * 10⁷ (*A/m²*)

Ic = J * Wc * Hc
8.48824 * 10⁻⁷

Ic = 8.48824 * 10⁻⁷ A

Ir = Ic * 8
6.7906 * 10⁻⁶

Ir = 6.7906 * 10⁻⁶ A

```

Figure A.11: Mathematic code used to calculate the maximum theoretical current that can be produced by the MFPG device. This was calculated for stator magnet height of 20μm and coil height of 2μm.

```

Theoretical Voltage and Power


$$R = \frac{\rho L}{A}$$


 $\rho_{Au} = 2.44 \times 10^{-8};$  (*Resistivity of Gold at 20°C in Ohm-meters*)
 $L_C = 0.0461814;$  (*Length of the coil in meters*)
 $A_C = 20 \times 10^{-12};$ 
(*Cross-sectional area of the coil in square meters*)
 $I_{Th} = 6.7906 \times 10^{-6};$  (*Max theoretical current generated by
Stator in Amps*)


$$R_C = \frac{\rho_{Au} \star L_C}{A_C}$$


56.3413


$$V_C = I_{Th} \star R_C$$


0.000382591


$$P = V_C \star I_{Th}$$


 $2.59802 \times 10^{-9}$ 

Theoretical power output for this design would then be approximately
2.6 nW.

```

Figure A.12: Mathematica code used to calculate the voltage and maximum theoretical power output from this design. Again this is calculated for stator magnet height of 20 μ m and coil height of 2 μ m.

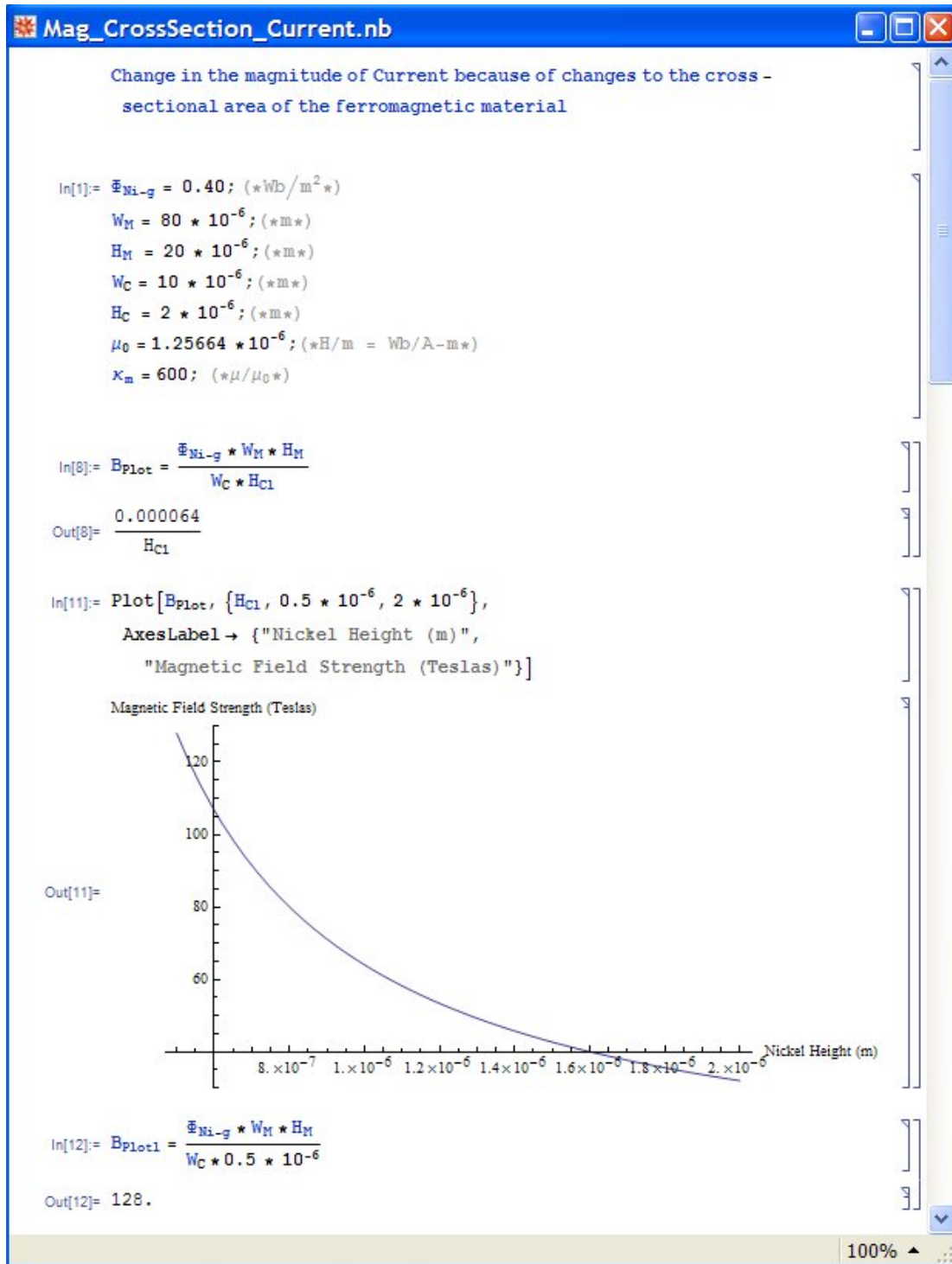


Figure A.13: Mathematica code used to calculate the magnetic field strength of the stator magnets with respect to the height of the coil. Note this calculation is for a magnet height of 20 μm . The field strength would be 512 Teslas for a magnet height of 80 μm .

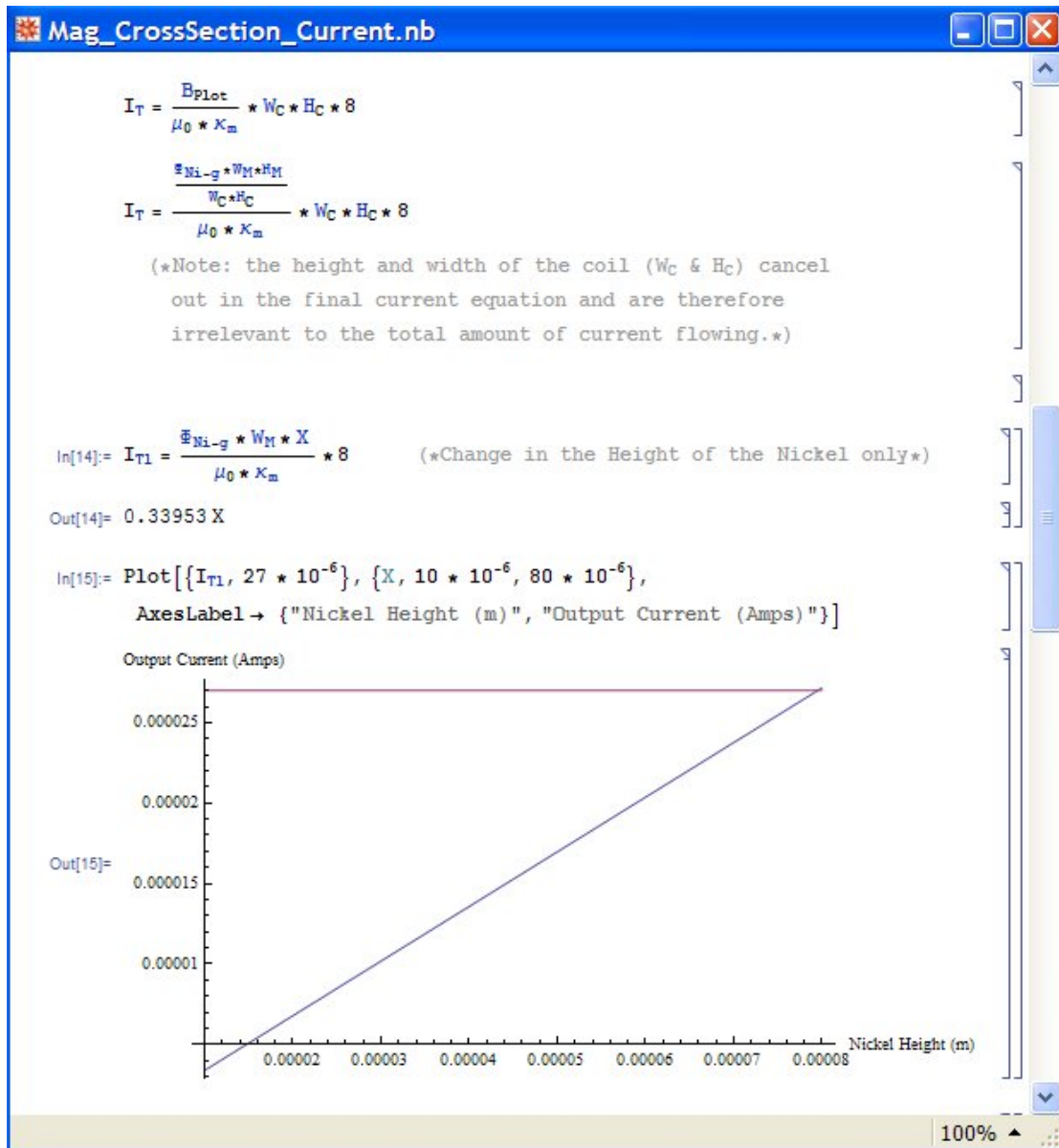


Figure A.14: Mathematica code used to calculate the total output current as a function of the magnet height. Note the output current for the device when the magnets are 80 μm in height is just over 27 μA .

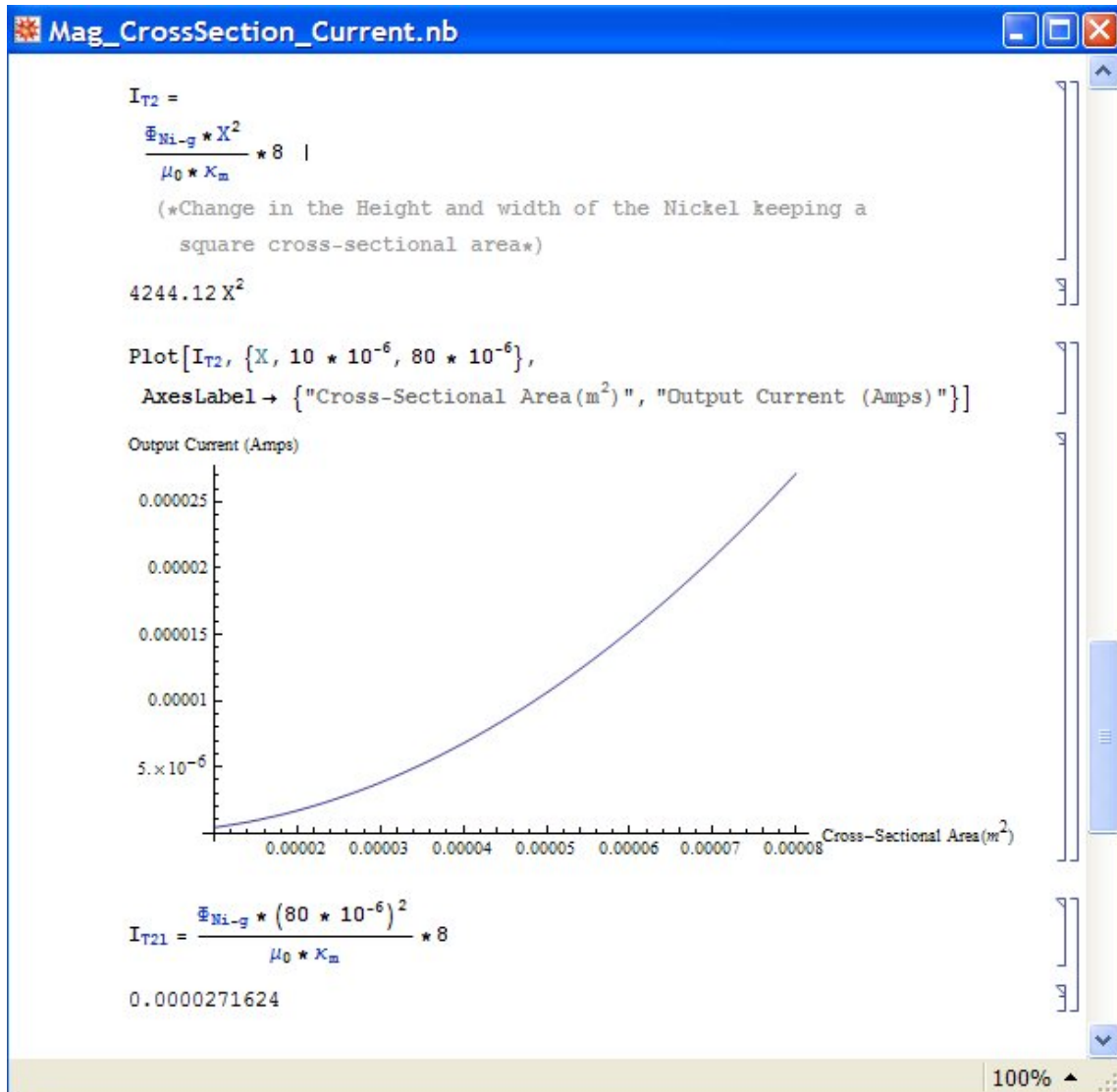


Figure A.15: Mathematica code used to calculate the total output current as a function of the magnets height and width. Both are changing at the same rate to keep a square cross-sectional area. The output current for the device when the magnets are 80 μm in height is approximately 27.16 μA .

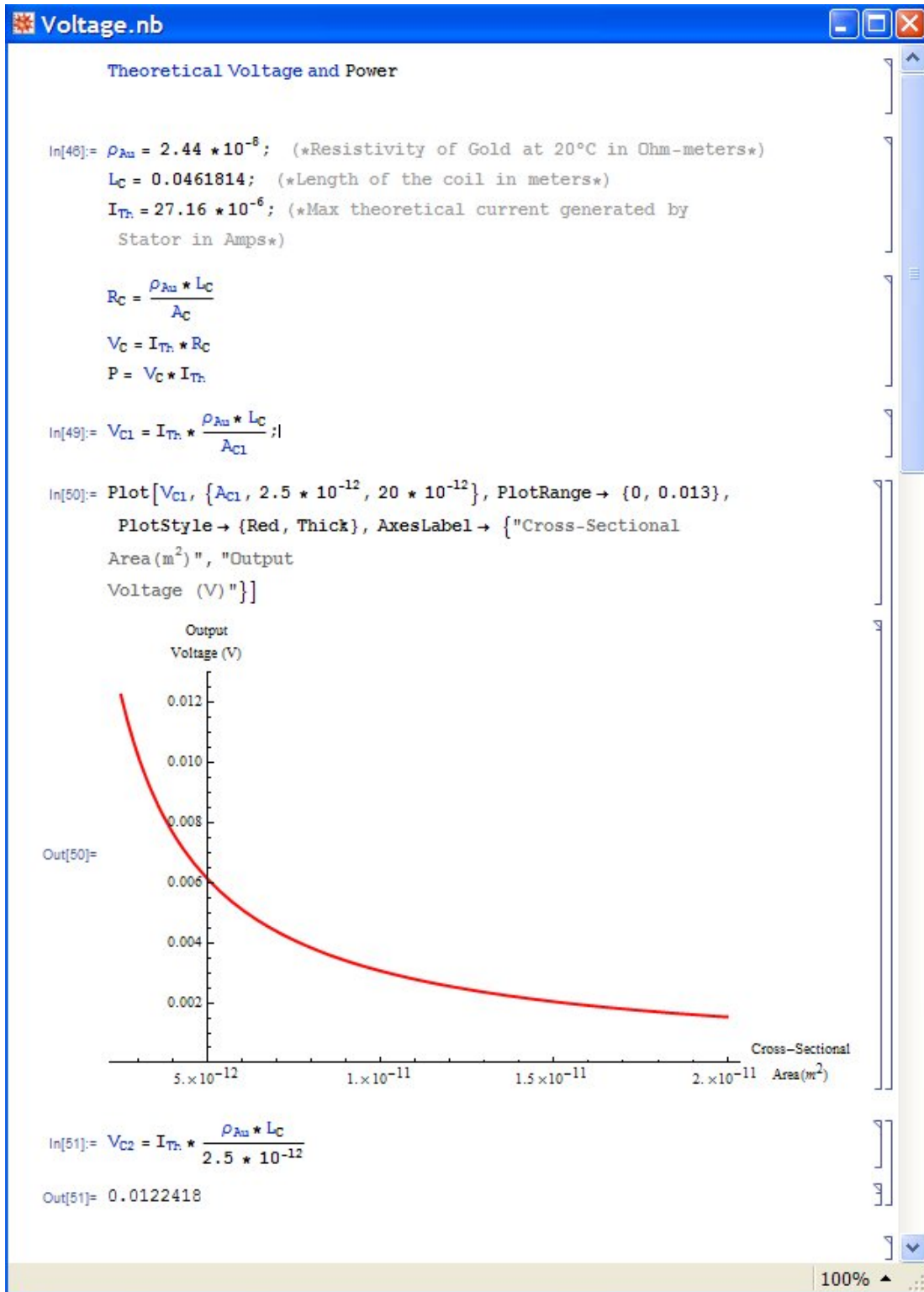


Figure A.16: Mathematica code used to calculate the voltage output of the device as a function of the coil's cross-sectional area. The voltage is maximum when the coil is thinnest, for a value of 12.24 mV when the coil's cross-section is $2.5 \times 10^{-12} \text{ m}^2$.

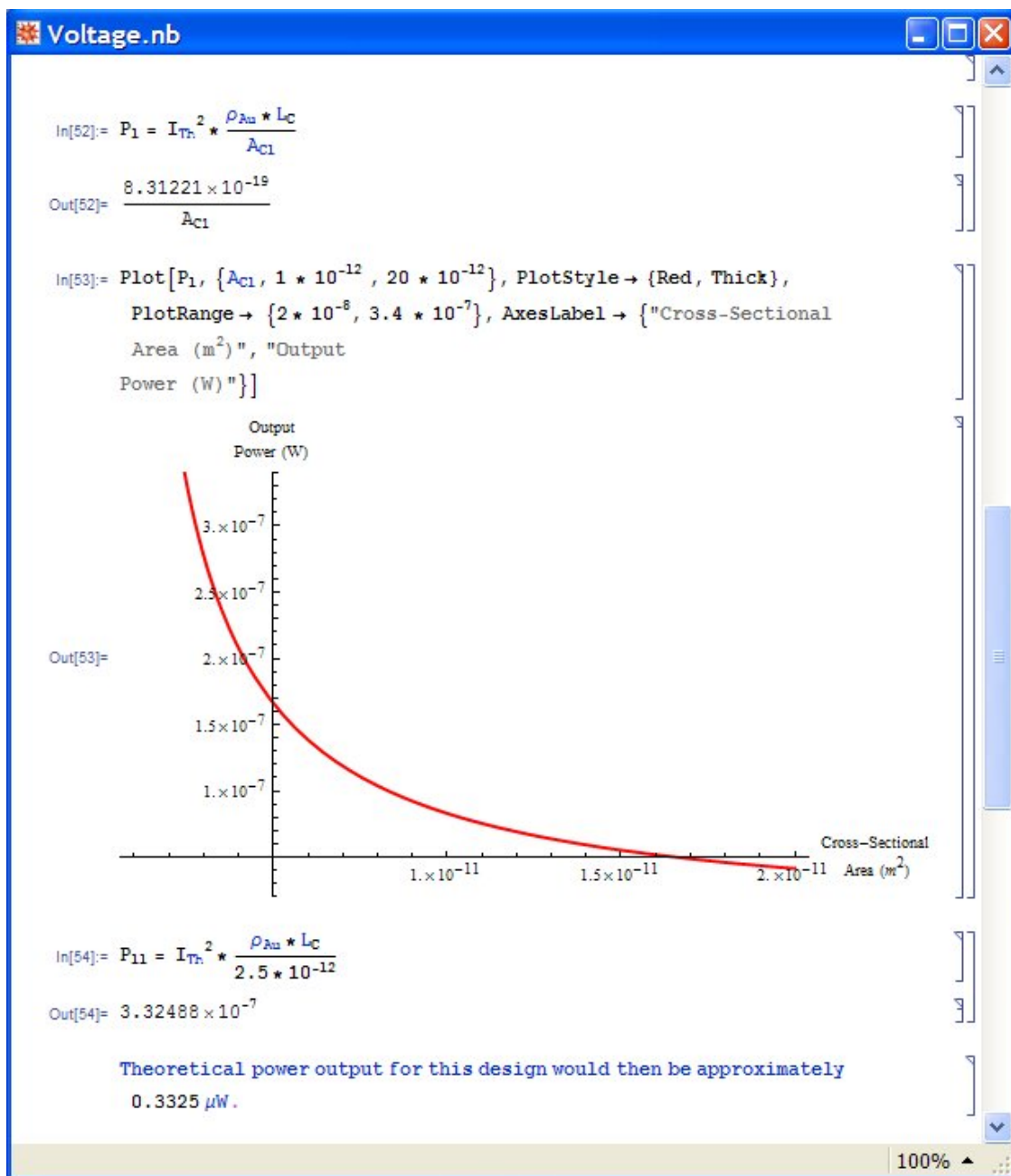


Figure A.17: Mathematica code used to calculate the theoretical maximum power output of this device as a function of the coil's cross-sectional area. The curve follows the same shape as the voltage curve and again is maximized when the cross-sectional area is minimum. The maximum theoretical power output from this calculation is 0.3325 μW when the stator magnets are 80 μm high and the cross-sectional area of the coil is $2.5 \times 10^{-12} \text{ m}^2$.


```

Resistance Calculations for Gold Coil Runner

ρAu = 2.44 * 10-8; (*Resistivity of Gold at 20°C in Ohm-meters*)
L = 760 * 10-6;
w1 = 12.62 * 10-6;
w2 = 12.85 * 10-6;
w3 = 12.88 * 10-6;
T1 = 0.2674 * 10-6;
T2 = 0.5099 * 10-6;
T3 = 1.0375 * 10-6;

A1 = w1 * T1
A2 = w2 * T2
A3 = w3 * T3

3.37459 × 10-12
6.55221 × 10-12
1.3363 × 10-11

R1 =  $\frac{\rho_{Au} * L}{A_1}$ 
R2 =  $\frac{\rho_{Au} * L}{A_2}$ 
R3 =  $\frac{\rho_{Au} * L}{A_3}$ 

5.49519
2.83019
1.38771

```

Figure A.18: Mathematica code used to calculate the theoretical resistance for the 0.25, 0.5 and 1.0 μm thick center coil traces using the average fabricated dimensions for each group.

```

Coil Complete Resistance.nb

Resistance Calculations for the Complete Gold Coil
Using approximate dimensions

In[71]:= rho_Au = 2.44 * 10^-8; (*Resistivity of Gold at 20°C in Ohm-meters*)
L = 0.04618;
w1 = 10 * 10^-6;
w2 = 10.43 * 10^-6;
w3 = 11 * 10^-6;
T1 = 0.2725 * 10^-6;
T2 = 0.52 * 10^-6;
T3 = 1.0375 * 10^-6;

In[79]:= A1 = w1 * T1
A2 = w2 * T2
A3 = w3 * T3

Out[79]= 2.725 * 10^-12
Out[80]= 5.4236 * 10^-12
Out[81]= 1.14125 * 10^-11

In[82]:= R1 = (rho_Au * L) / A1
R2 = (rho_Au * L) / A2
R3 = (rho_Au * L) / A3

Out[82]= 413.502
Out[83]= 207.757
Out[84]= 98.7331

```

Figure A.19: Mathematica code used to calculate the theoretical resistance for the complete 0.25, 0.5 and 1.0 μm thick coil traces using the average fabricated dimensions of each group.

```

Resistance Calculations for Titanium Seed Layer between the Gold
traces.

σTi = 2.381; (*Conductivity of Titanium at 20°C in 1/Ohm-micrometers*)
L = 10;
w1 = 10; (*Length, width, and thickness all in micrometers*)
T1 = 0.02;

ρTi =  $\frac{1}{\sigma_{Ti}}$ 
0.419992

A1 = w1 * T1
0.2

R1 =  $\frac{\rho_{Ti} * L}{A_1}$ 
20.9996

Resistance

```

Figure A.20: Mathematica code used to calculate the theoretical resistance of the 200 Å thick titanium seed layer between the two gold traces. Each section of titanium between the two layers of gold has an area of 100 μm².

Appendix B: Mask Designs

This appendix contains all of the designs used to fabricate the MFPG devices. The images on the following pages were created in the MEMSPRO L-edit® layout editor and sent to Photo Sciences, Inc. in Torrance, CA for mask fabrication using their Fast-Track photomask service. A total of four masks were used for the initial design, each containing separate portions of the designs for the complete device. All designs shown in this appendix constitute original work.

The designs were created using two L-edit layers: Poly-0 and Hole0. These correspond to GDSII layers 13 and 41, respectively. The Poly-0 layer was used to define the dark portions of the masks while the Hole0 layer was used to open holes in the Poly-0 layer, in essence, a subtractive process.

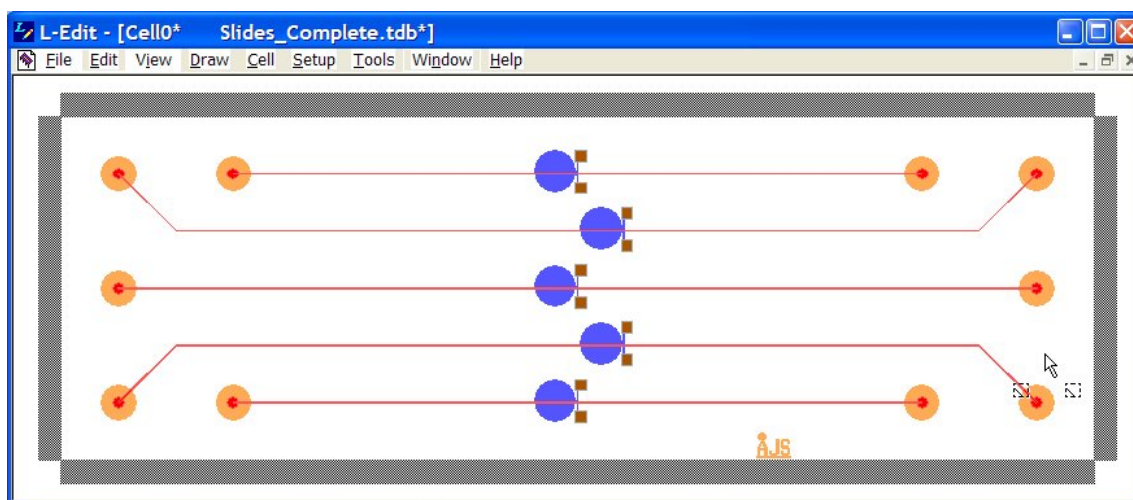


Figure B.1: L-edit layout showing all layers of the MFPG device.

This image represents a composite of all of the layers presented in Figure B.1 through Figure B.28. Image colors have been changed to fully illustrate the different layers.

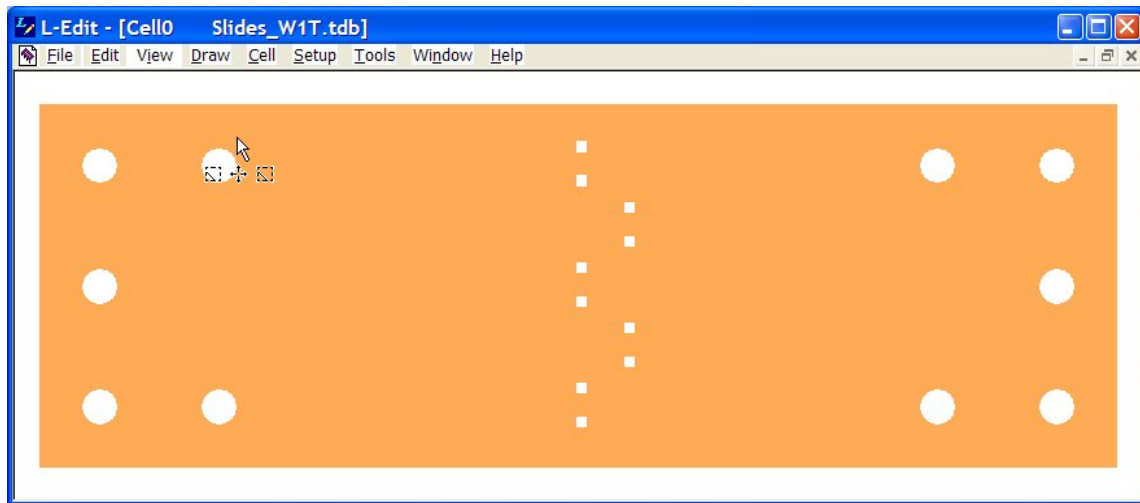


Figure B.2: L-edit layout for the top of first glass slide.

Features: 1000 μm diameter round holes, 500 μm x 500 μm square holes

Purpose: Round holes are the main fluid inlet/outlet holes. Square hole windows for the electrical contacts. All features on this mask will be etched completely through the wafer.

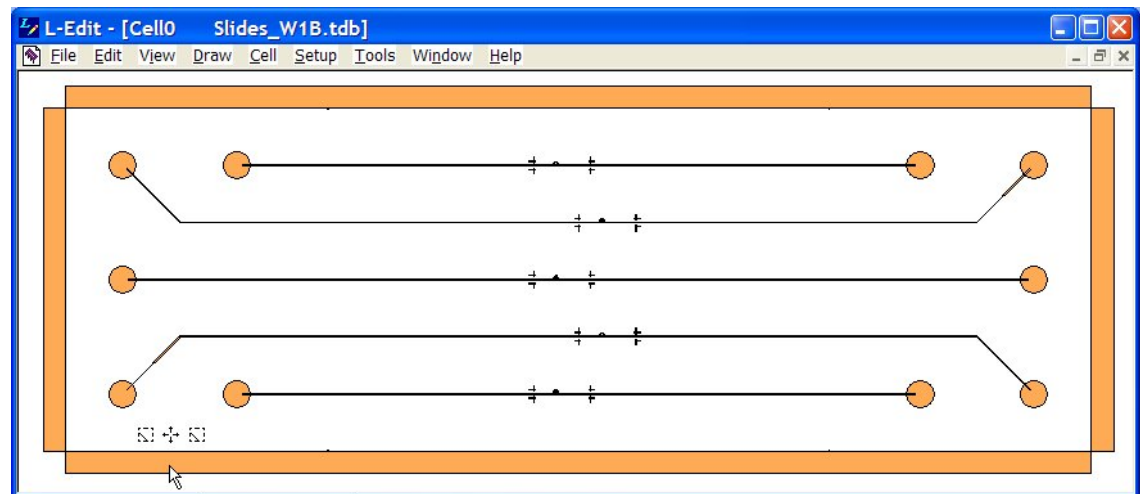


Figure B.3: L-edit layout for the bottom of the first glass slide.

Features: 900 μm diameter rounds, 40 μm wide lines, alignment marks.

Purpose: Rounds are purely for alignment purposes and will be etched through during the top etch for this wafer. The lines will be etched to a depth of 2 μm and will fit snugly into the microchannels on the top of wafer 2. This is for alignment and to prevent sealant from leaking into the microchannels.

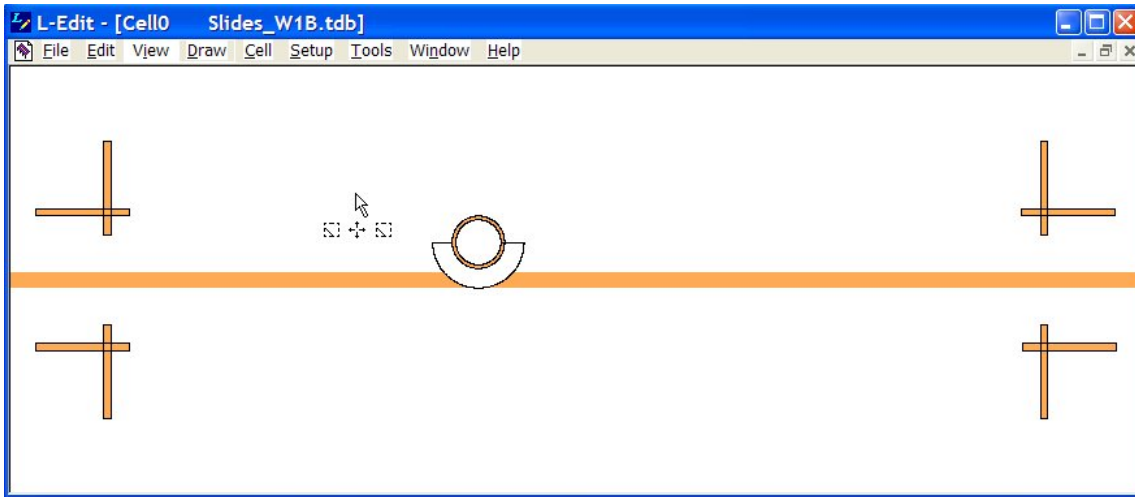


Figure B.4: Enlarged image of features on bottom of the first glass slide.

Features: 40 μ m wide lines, 10 μ m wide torus w/ inner radius of 60 μ m, alignment marks

Purpose: Lines are meant to fit snugly into the channels on the top of slide 2. This will help with alignment and prevent CrystalBond from leaking into the channels when the slides are bonded. The torus is meant to be an upper bumper for the turbine to reduce friction.

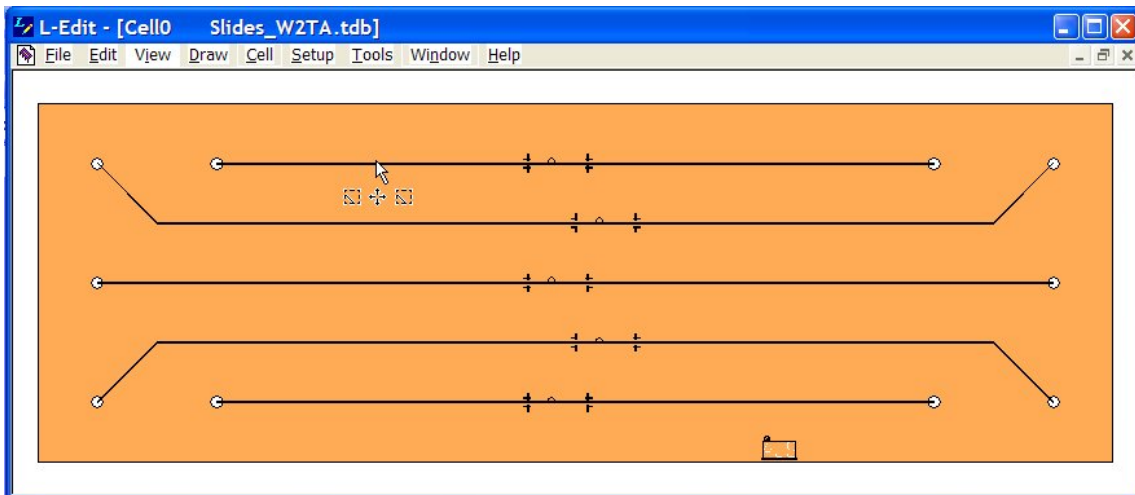


Figure B.5: L-edit layout of first etch design for top of second glass slide.

Features: 500 μ m diameter rounds, 40 μ m wide channels, alignment marks

Purpose: Round holes are the fluid inlet/outlet holes from the large holes in slide 1. The channels are for the actual fluid flow through the device.

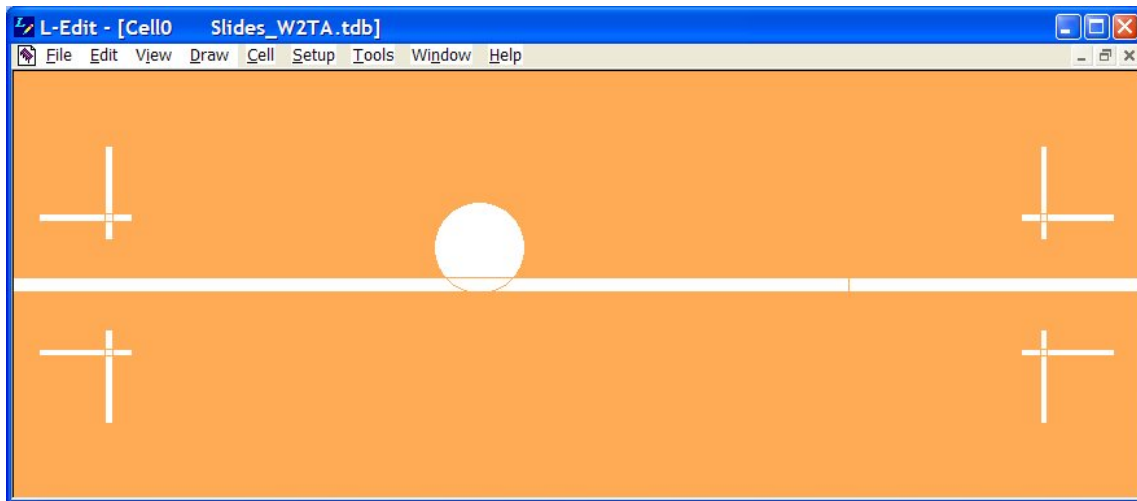


Figure B.6: Enlarged image of features on the first etch design for the top of the second glass slide.

Features: 244μm diameter round, 40μm wide channel, alignment marks

Purpose: The round is the cavity that the turbine will sit in and, again, the channel is for the fluid flow.

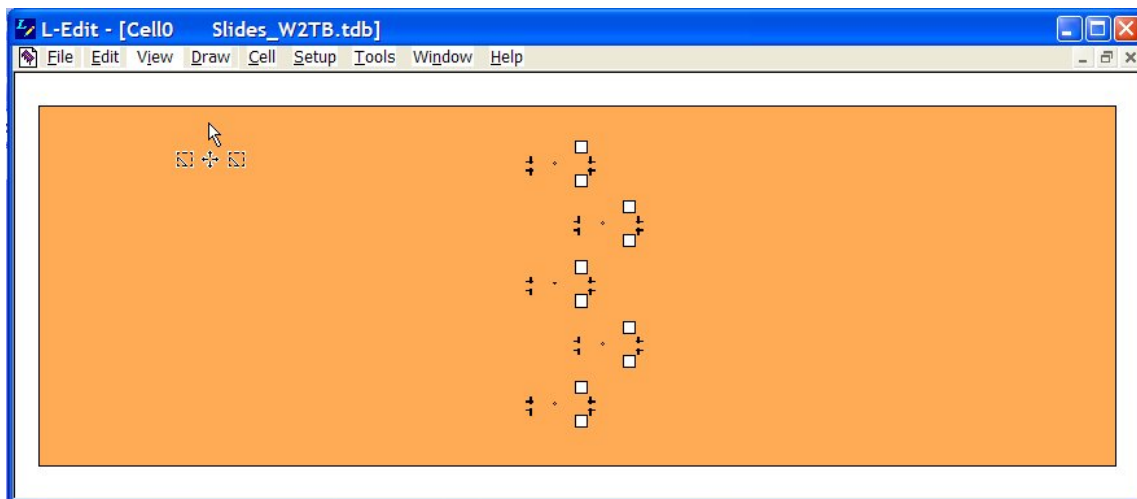


Figure B.7: L-edit layout of second etch design for top of second glass slide.

Features: 500μm x 500μm square holes, alignment marks

Purpose: The square holes are windows for the electrical contacts and will be etched completely through the wafer.

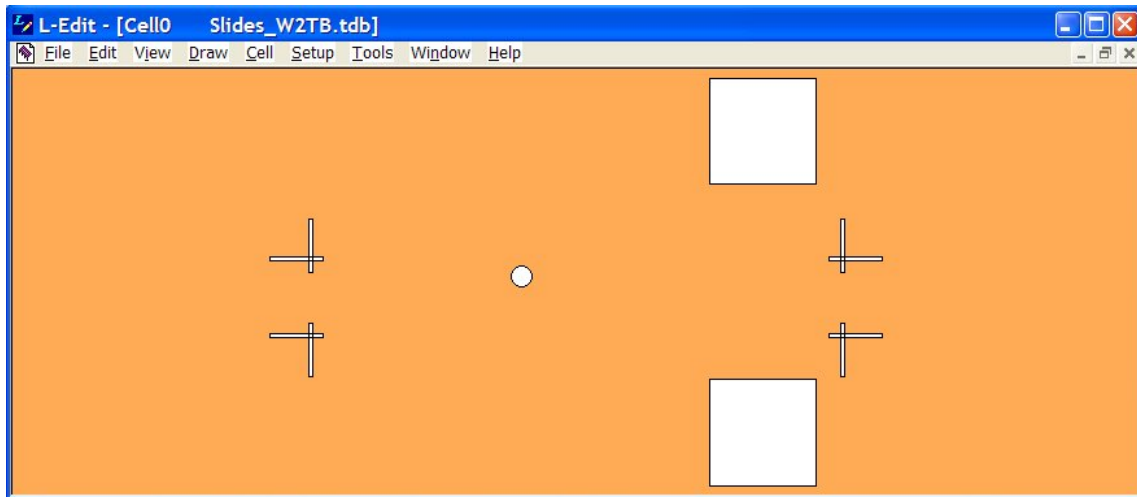


Figure B.8: Enlarged image of features on the second etch design for the top of the second glass slide.

Features: 100µm diameter round, 500µm x 500µm square holes, alignment marks

Purpose: The 100µm diameter round hole is the pass-through window for the turbine shaft. Again, the square holes are windows for the electrical contacts and all features on this mask will be etched completely through the wafer.

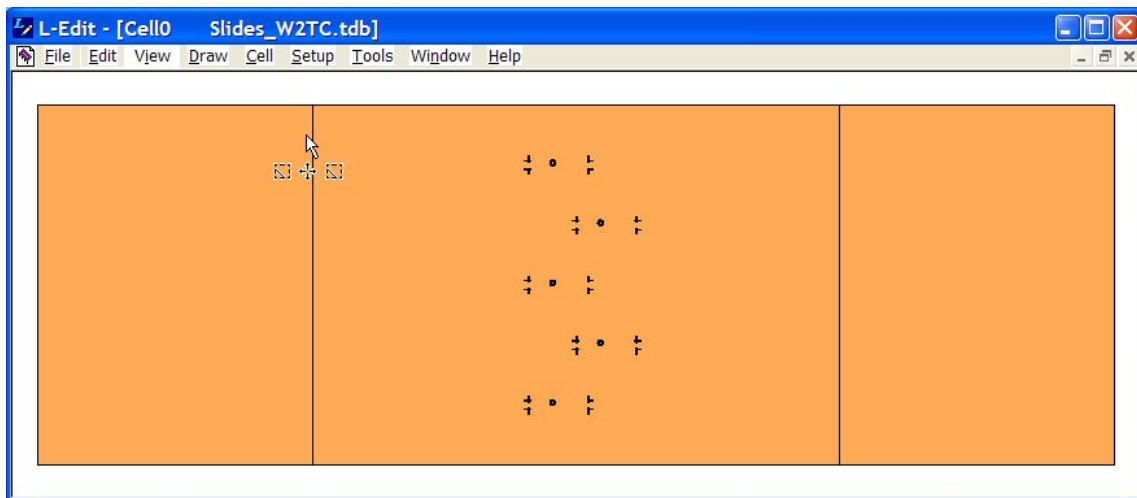


Figure B.9: L-edit layout of third etch design for top of second glass slide.

Features: 120µm diameter torus in center of a 240µm hole, alignment marks

Purpose: The torus is meant to be a bottom bumper for the turbine to reduce friction. It should mirror the torus on the bottom of the first slide.

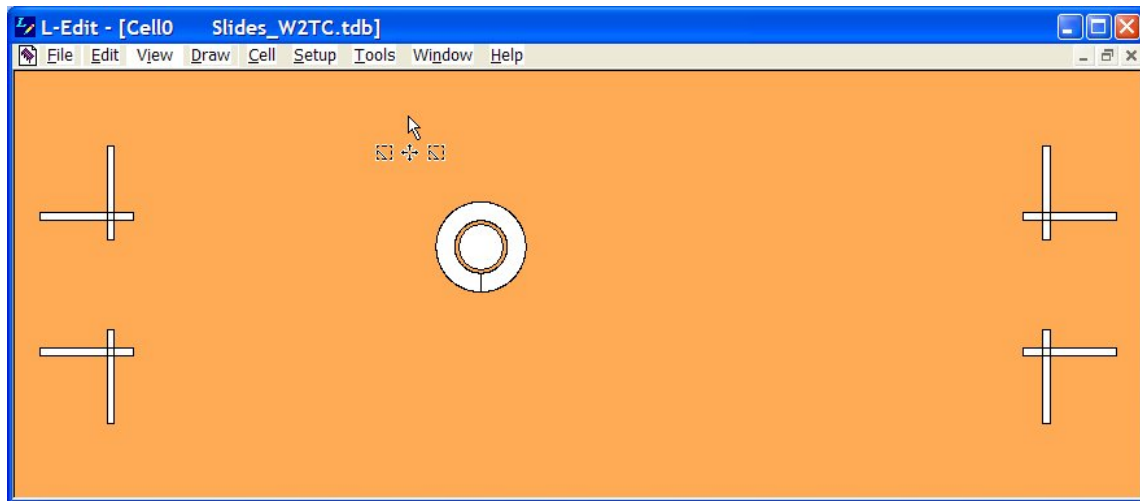


Figure B.10: Enlarged image of features on the third etch design for the top of the second glass slide.

Features: 120 μ m diameter torus in center of a 240 μ m hole, alignment marks

Purpose: The torus is meant to be a bottom bumper for the turbine to reduce friction. It should mirror the torus on the bottom of the first slide.

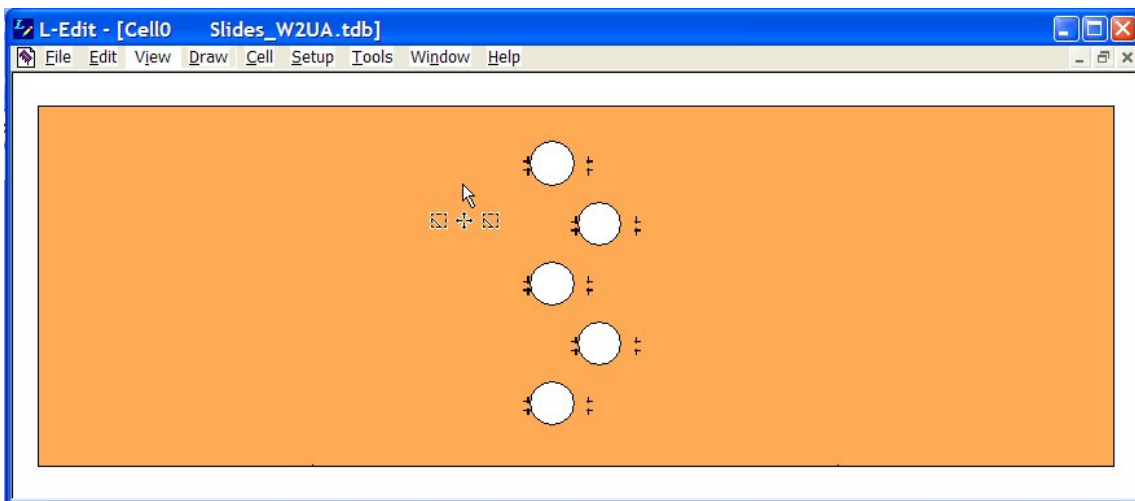


Figure B.11: L-edit layout of first etch design for the bottom of the second glass slide.

Features: 1800 μ m diameter round, alignment marks

Purpose: The 1800 μ m diameter round is the cavity for the stator. When completed, the stator will be recessed into the bottom of slide 2.

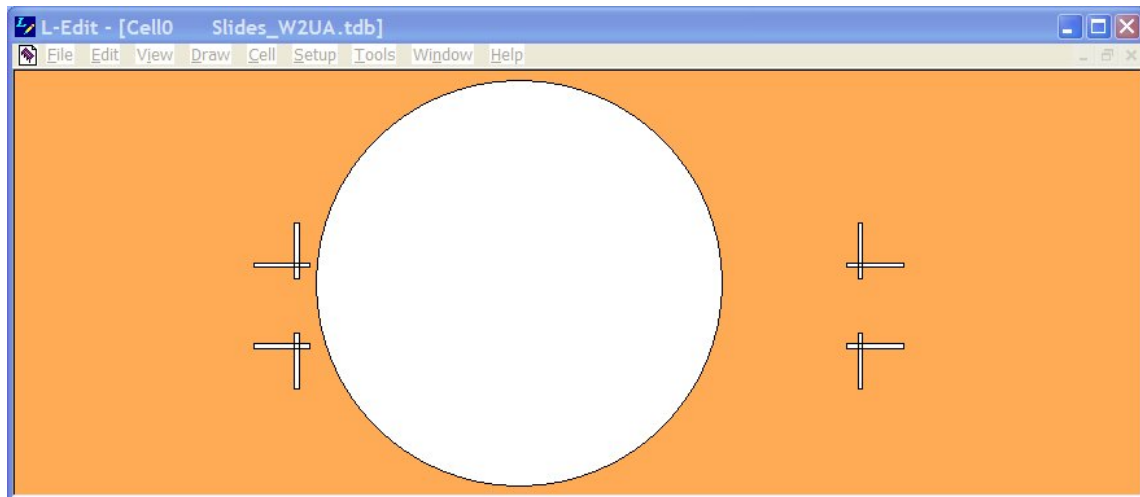


Figure B.12: Enlarged image of features on the first etch design for the bottom of the second glass slide.

Features: 1800μm diameter round, alignment marks

Purpose: The 1800μm diameter round is the cavity for the stator. When completed, the stator will be recessed into the bottom of slide 2.

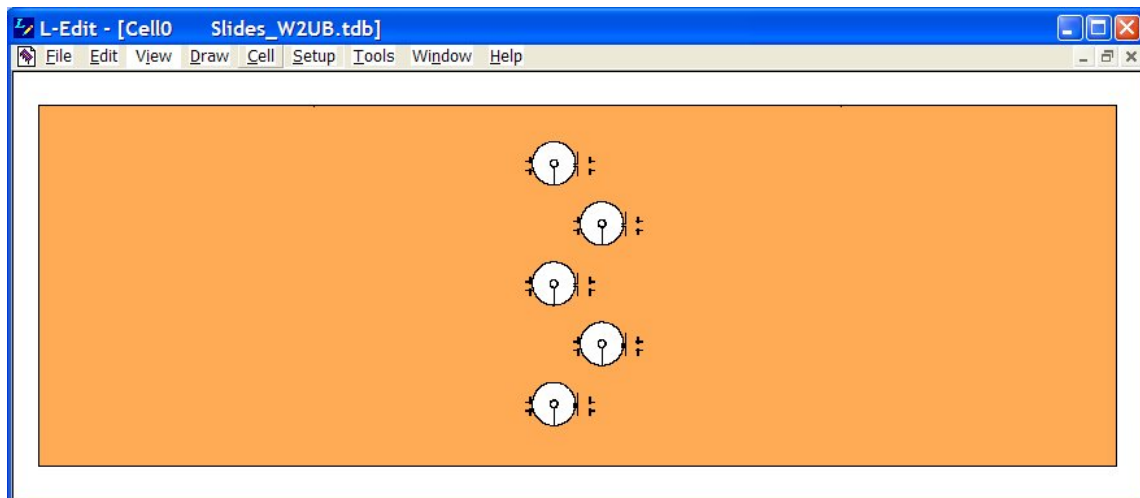


Figure B.13: L-edit layout of second etch design for the bottom of the second glass slide.

Features: 300μm diameter torus, 10μm wide, in center of an 1800μm wide hole, 30μm wide channels, alignment marks

Purpose: The torus is meant to be a bumper for the stator, similar to the ones used for the turbine. The channels are to allow room for the gold wires connecting the coil to the contact pads on the top of slide 3.

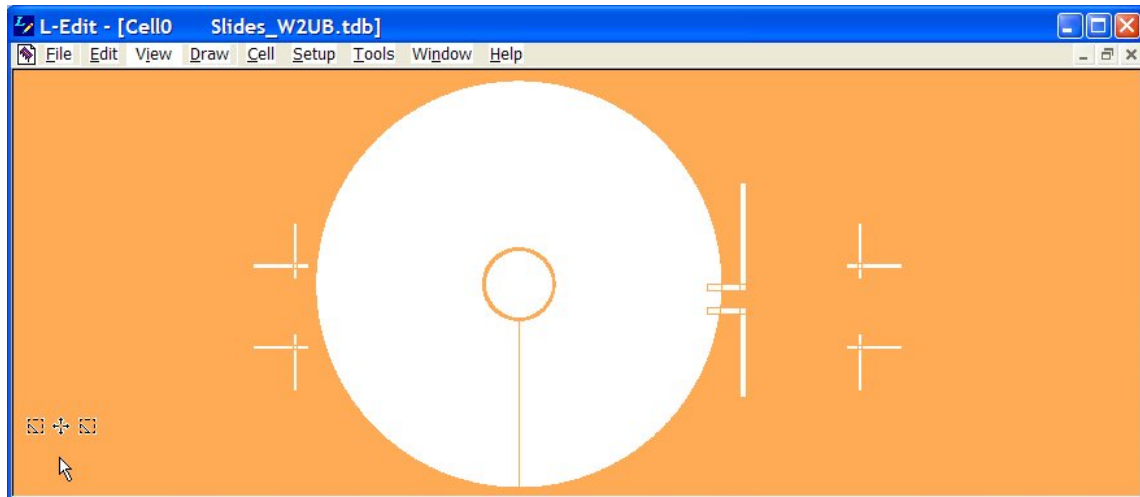


Figure B.14: Enlarged image of features on the second etch design for the bottom of the second glass slide.

Features: 300 μ m diameter torus, 10 μ m wide, in center of an 1800 μ m wide hole, 30 μ m wide channels, alignment marks

Purpose: The torus is meant to be a bumper for the stator, similar to the ones used for the turbine. The channels are to allow room for the gold wires connecting the coil to the contact pads on the top of slide 3.

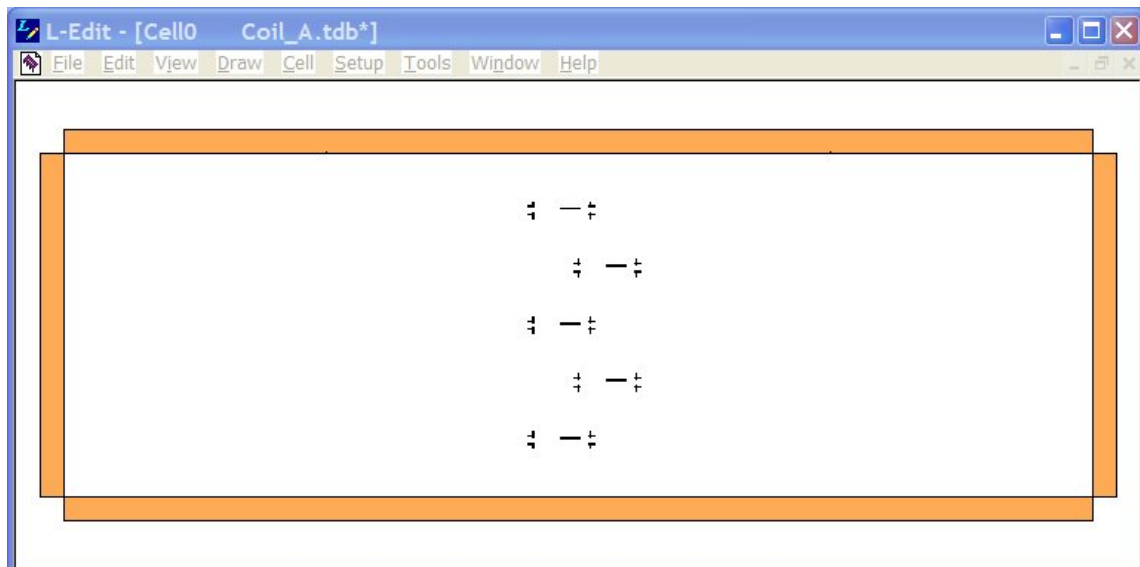


Figure B.15: L-edit layout of first deposition design for the top of the third glass slide.

Features: 10 μ m wide wire, alignment marks

Purpose: This is the wire running from the center of the coil to one of the contact pads.

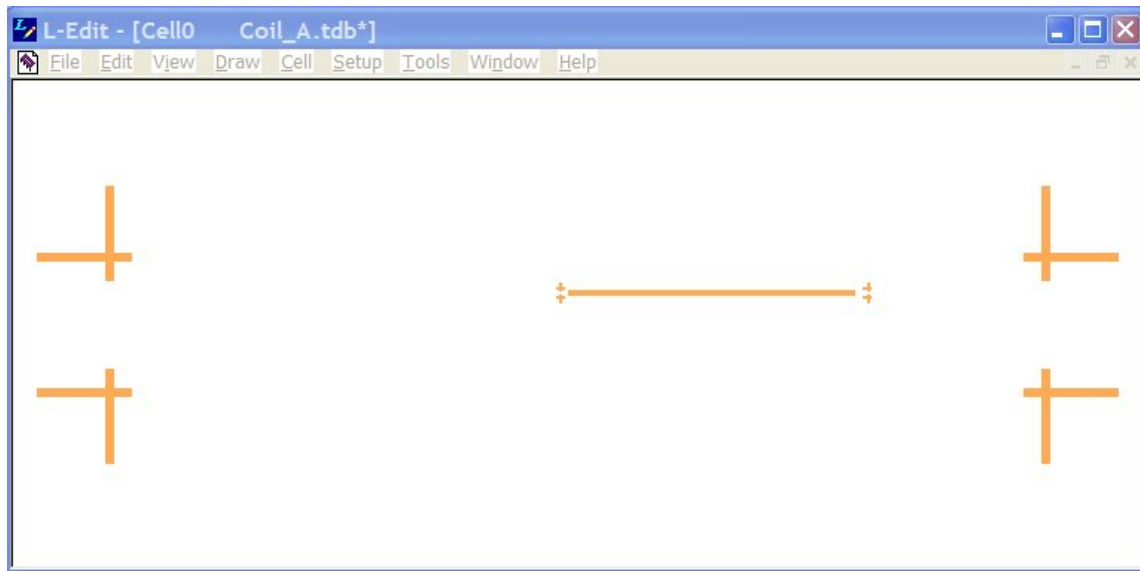


Figure B.16: Enlarged image of features on the first deposition design for the top of the third glass slide.

Features: 10 μ m wide wire, alignment marks

Purpose: This is the wire running from the center of the coil to one of the contact pads.

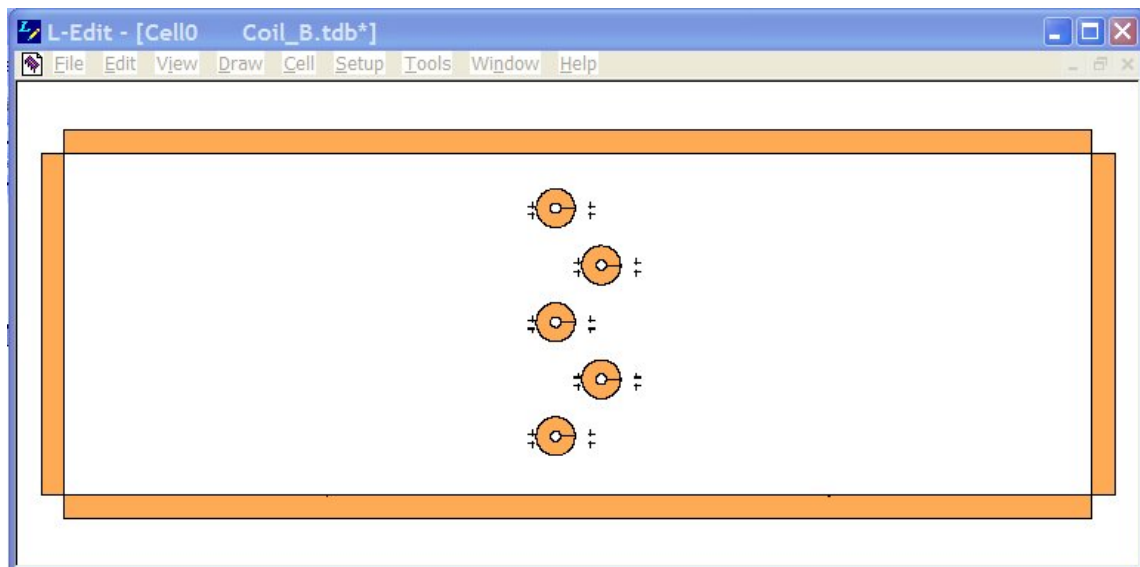


Figure B.17: L-edit layout of second deposition design for the top of the third glass slide.

Features: Torus with inner and outer radii of 225 μ m and 850 μ m, alignment marks

Purpose: Nitride insulating layer to prevent shorting between the coil and the inner lead from Figure B.16.

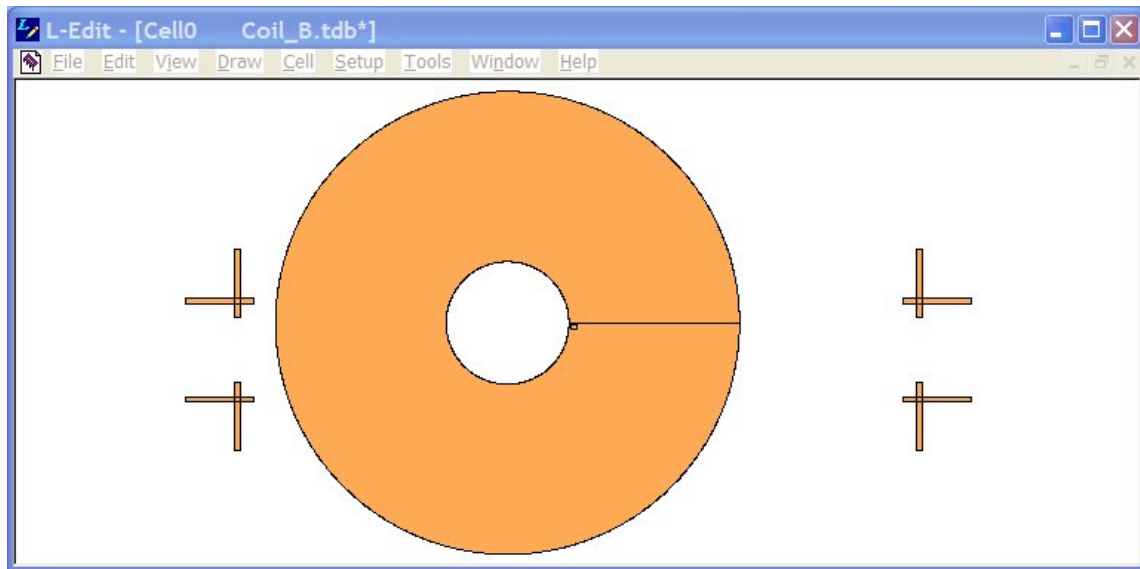


Figure B.18: Enlarged image of features of the second deposition design for the top of the third glass slide.

Features: Torus with inner and outer radii of 225 μm and 850 μm , alignment marks

Purpose: Nitride insulating layer to prevent shorting between the coil and the inner lead from Figure B.16.

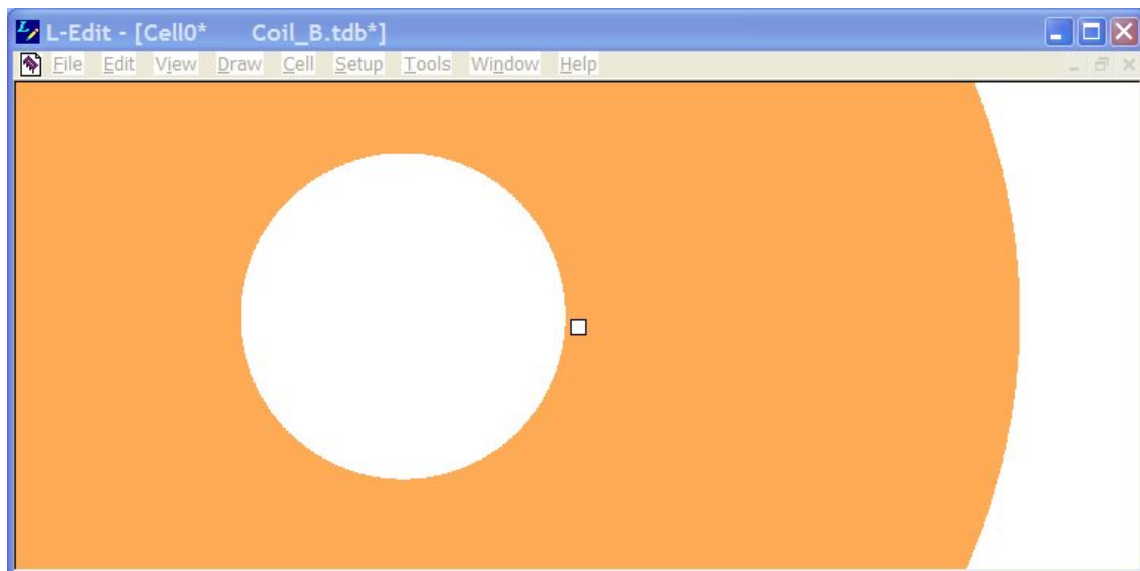


Figure B.19: 2X-enlarged image of features of the second deposition design for the top of the third glass slide.

Features: 20 μm wide square opening in torus

Purpose: Allow for contact between the inner lead and the coil.

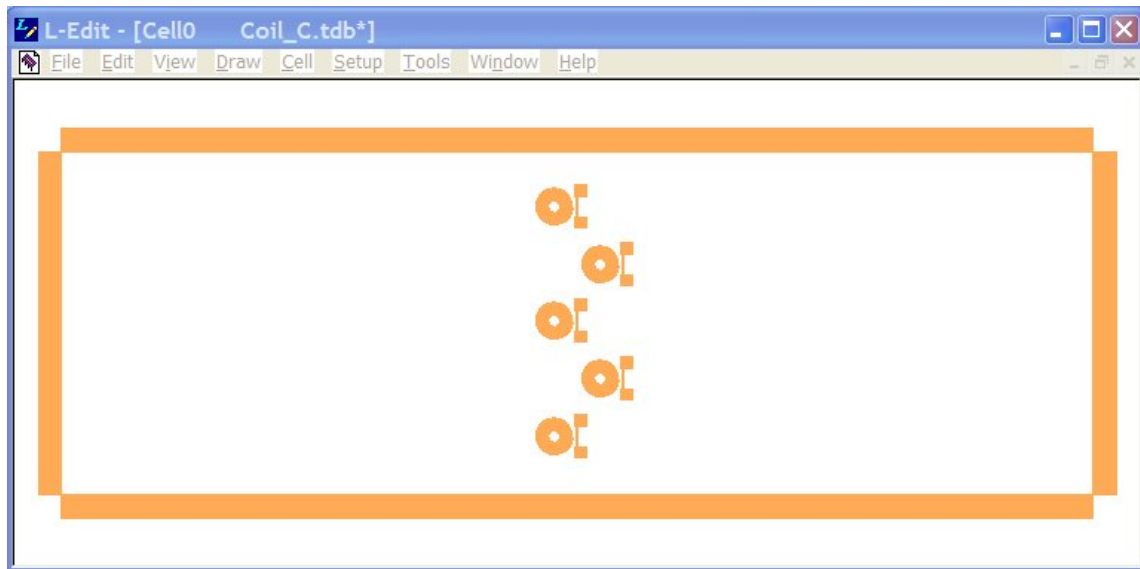


Figure B.20: L-edit layout of third deposition design for the top of the third glass slide.

Features: Coils with contact pads, alignment marks

Purpose: Allow current to flow as the stator magnet rotates above

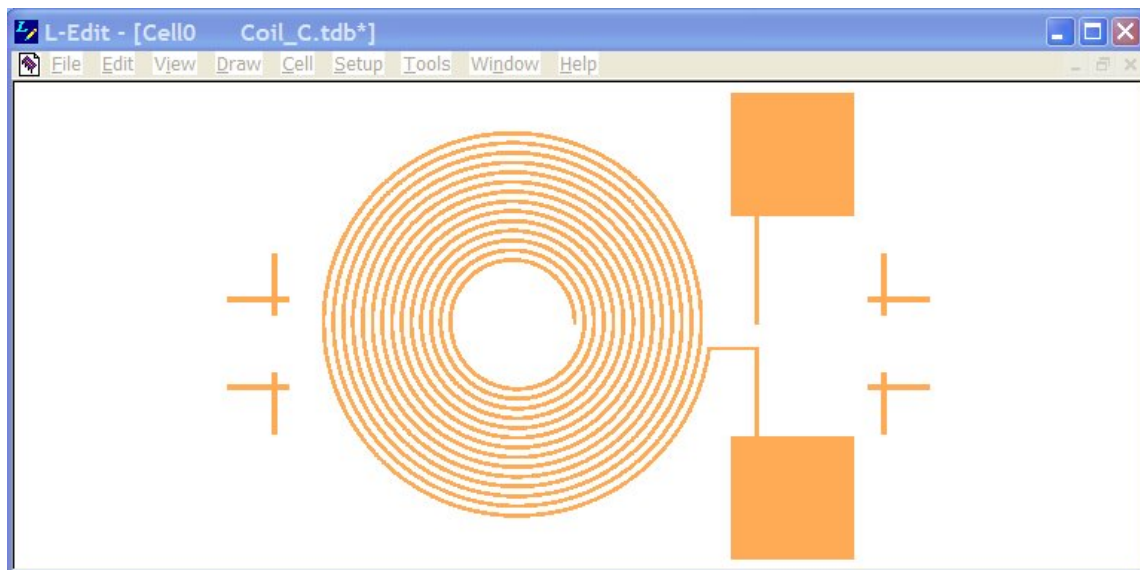


Figure B.21: Enlarged image of features of the third deposition design for the top of the third glass slide.

Features: Coils with contact pads, alignment marks

Purpose: Allow current to flow as the stator magnet rotates above

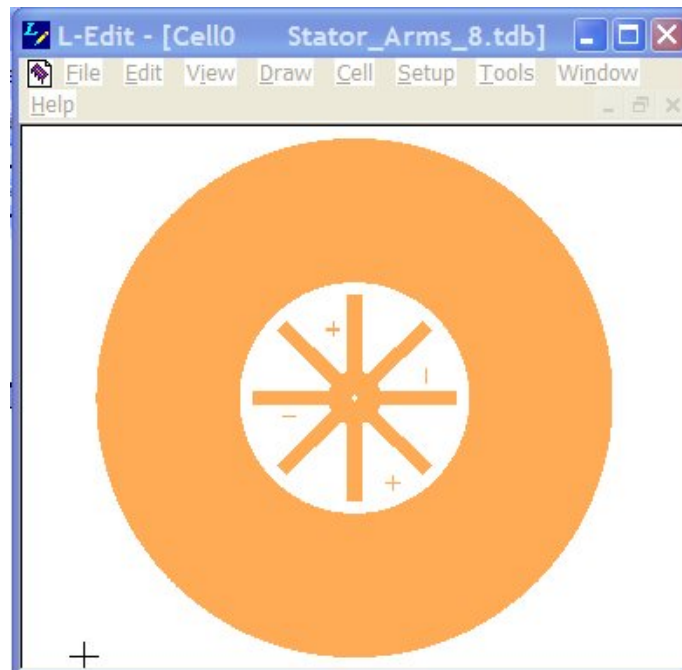


Figure B.22: L-edit layout of stator arms with alignment marks and non-etch buffer.

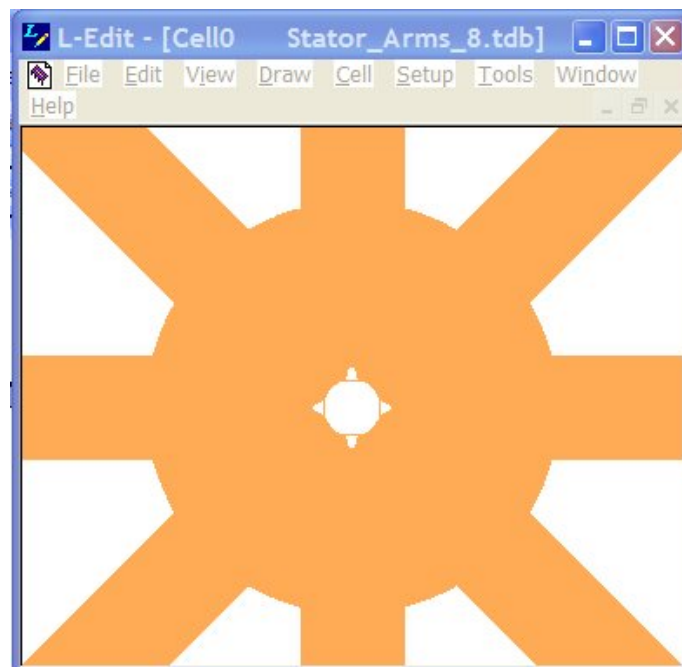


Figure B.23: Enlarged image of stator center showing shaft opening with grooves.

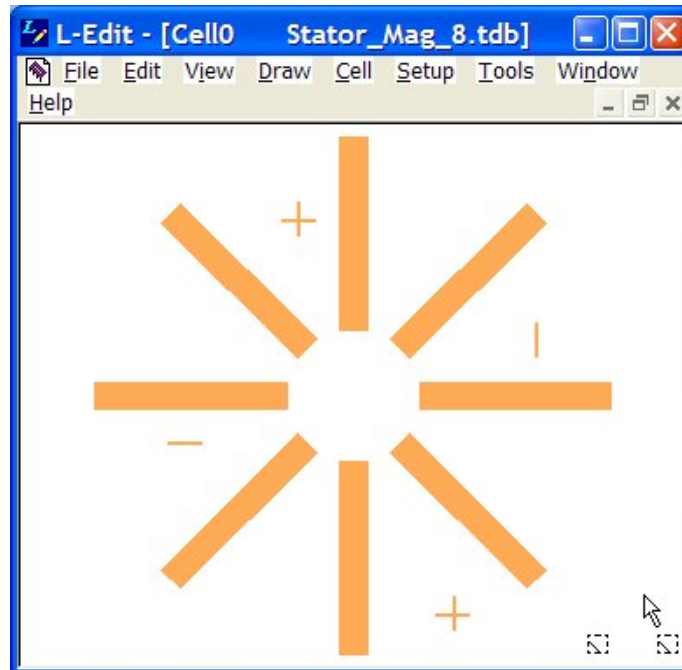


Figure B.24: L-edit layout of stator magnets with alignment marks.

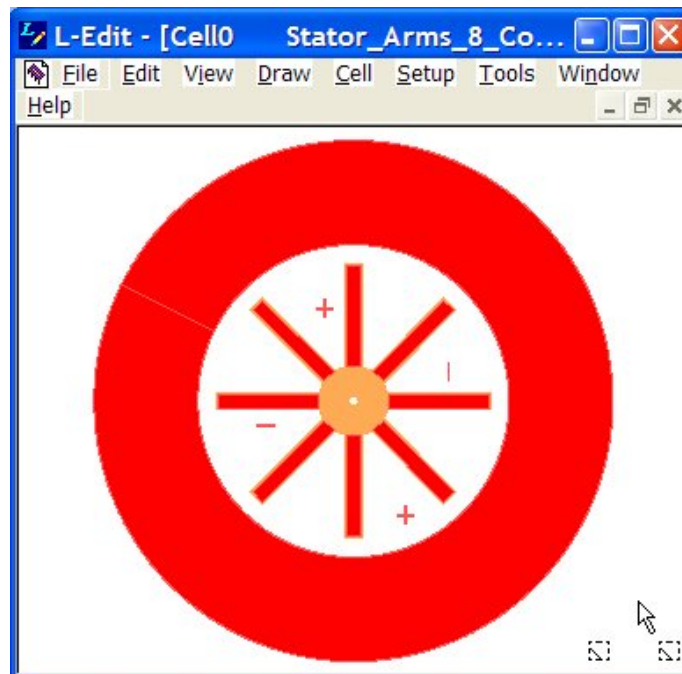


Figure B.25: L-edit layout of stator magnets (red) superimposed on stator arms (gold) with alignment marks and non-etch buffer.

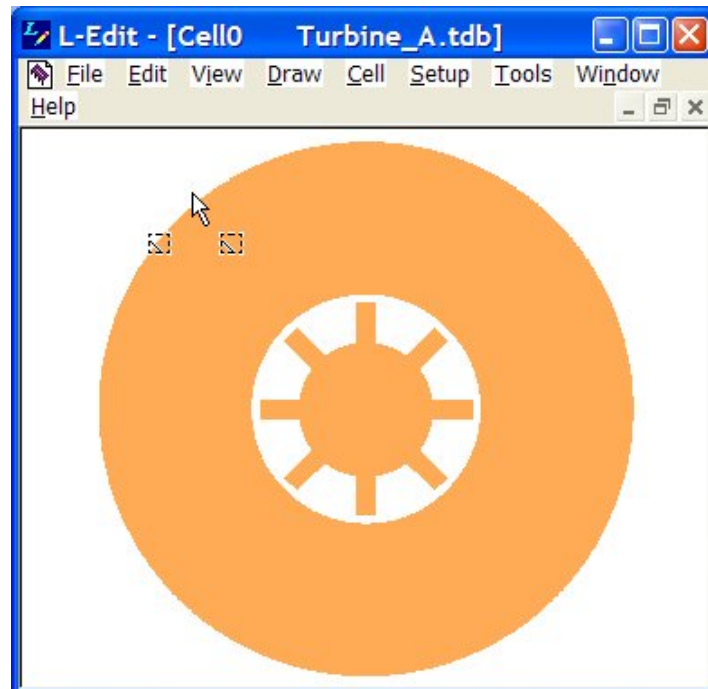


Figure B.26: L-edit layout of the turbine wheel with non-etch buffer.

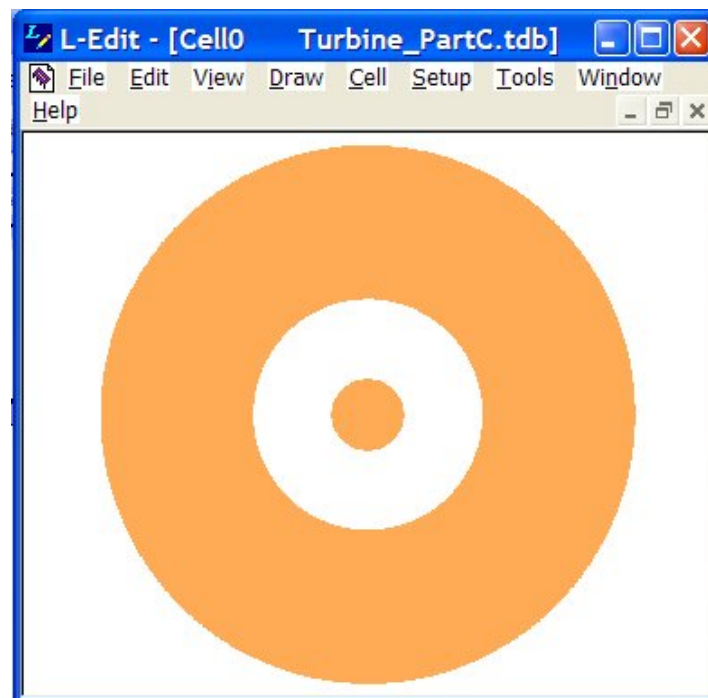


Figure B.27: L-edit layout of primary turbine shaft design.

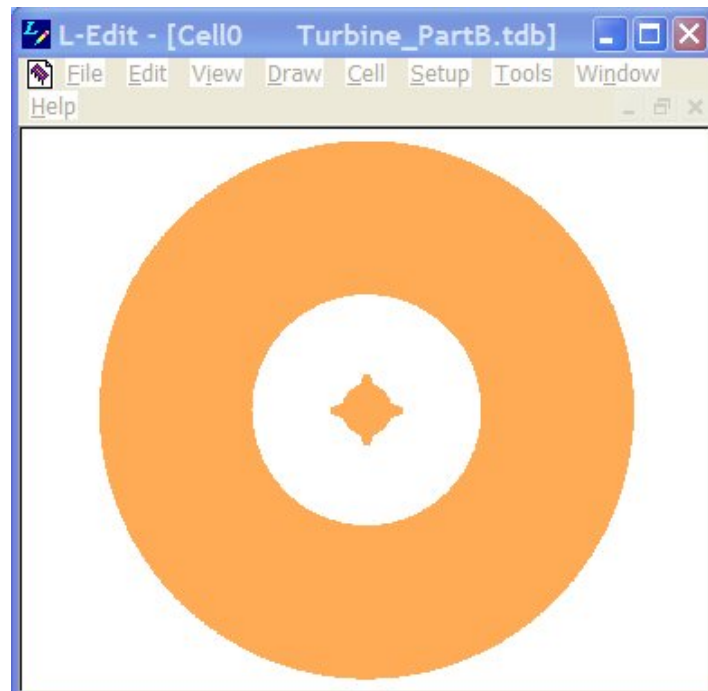


Figure B.28: L-edit layout of secondary turbine shaft design.

Appendix C: Fabrication Methods

This appendix contains figures and tables showing detailed recipes for lithograph, metal deposition and electroplating derived from recipes provided by AFRL/SND.

Exposure times and temperatures on lithography recipes have been modified to reflect the actual equipment used.

Table C.1: Recipe used for patterning of metal deposition with SF-11 and AZ5214E photoresist.

Process Step	Notes	Date/Time
Inspect Wafer: Note any defects Solvent clean only if needed	<u>Start Date</u> <u>Start Time</u>	
Solvent Clean (if needed): 20 sec acetone rinse at 500 rpm 20 sec isopropyl alcohol rinse at 500 rpm Dry with nitrogen at 500 rpm Dry wafer with nitrogen on clean texwipes		
Dehydration Bake: 1 min 110°C hot plate bake		
PMGI SF11 COAT: Flood wafer with PMGI SF11 30 sec Spin at 4000 rpm, Ramp=200 Clean backside with EBR and swab 2 min 200°C Hot Plate Bake Cool Wafer on Cooling Plate		
Resist Coat: Spin on 5214E Resist at 4000 rpm, ramp at 200 for 1.4 um thickness. 60 sec 110°C hot plate bake		
Expose with Mask: No alignment for first level mask 2 sec exposure on MA6 Mask Aligner, 7 mW/cm ² , 365 nm	2.8 sec @ 5.6 mW/cm² ~16 mJ/cm²	
Post-Exposure Bake (Temperature is Critical!): 120 sec 125°C hot plate bake Record relative humidity	90 sec 110°C RH = 40.0%	
Flood Exposure: 90 sec Flood expose on MA6 @ 7 mW/cm ³	5.6 mW/cm³ ~500 mJ/cm²	
Develop: 30 sec develop with 351:DI water (1:5) at 500 rpm 30 sec DI water rinse at 500 rpm Dry with nitrogen at 500 rpm Dry wafer with nitrogen on clean texwipes		
Inspect Resist: Inspect photoresist under microscope		
Tencor Measurement (if needed): Measure photoresist step height Top: Center: Bottom:		

Asher Descum: 2 min, 200 W, 500 sccm O ₂ , LFE Barrel Asher		
Bottom Metal Deposition: Evaporate 200 Å Ti / (2500Å Au, 5000Å Au, 10,000Å Au)		
Lift-Off Bottom Metal: Use tape to remove excess metal with wafer on vacuum chuck (Tape lift-off) Visually inspect for metal removal 20 sec spray with acetone gun at 1000 rpm (pressurized @ 40 psi) 20 sec spray with acetone bottle at 500 rpm 30 sec spray with isopropyl alcohol at 500 rpm Dry with nitrogen at 500 rpm Dry wafer with nitrogen on clean texwipes		
INSPECT METAL: Inspect Metal with microscope; if some metal did not lift, then: 10 min Acetone soak (do not let wafer dry when transferring from petri dish to spinner chuck) 15 sec Acetone spray at 500 rpm 15 sec Isopropyl spray at 500 rpm Dry with N ₂ on clean Texwipes		
PMGI STRIP: 2 minute soak in 1165 Stripper at 90°C 6x DI Rinse in automatic rinse tank Dry with N ₂ on clean Texwipes		
Inspect Wafer: Inspect for resist removal under microscope		
Asher Clean: 4 min, 200 W, 500 sccm O ₂ , LFE Barrel Asher		
Tencor Measurement: Measure M1 step height Top: Center: Bottom:	Finish Date:	
	Finish Time:	

Table C.2: Recipe used for patterning Silicon Nitride and Borosilicate Glass (Silicon Dioxide) with 1813 photoresist.

Init	Process Step	Notes	
	PREPARATIONS: Coordinate PECVD nitride run with nitride operator Coordinate RIE nitride etch with etch operator Coordinate metal deposition with metal operator	Start Date	
	1813 COAT: Flood wafer with 1813 Photoresist 30 sec Spin at 4000 rpm, Ramp=200 Clean backside with Acetone 75 sec 110°C Hot Plate Bake Cool Wafer on Cooling Plate		
	EXPOSE 1813 WITH POST MASK: 8 sec Expose on MA6 Mask Aligner, 7mW/cm ² , 365 nm	10 sec @ 5.6 mW/cm ²	
	351 DEVELOP: 30 sec Spin Dev. with 351 Developer:DI 1:5 at 500 rpm 30 sec Spin Rinse with DI at 1000 rpm Dry with N ₂ on clean Texwipes		
	INSPECT LITHOGRAPHY: Inspect Photoresist with microscope using Yellow Filter Make sure features are open, clean, and sharp		
	REMOVE 1813: 15 sec Acetone spray GUN at 500 rpm 15 sec Acetone spray at 500 rpm 15 sec Isopropyl spray at 500 rpm 15 DI Dry with N ₂ on clean Texwipes Check backside and clean with Acetone is necessary		
	O₂ PLASMA ASHER: 4 min LFE Barrel Asher		

Run#

Film

Substrate

**DENTON VACUUM DISCOVERY-18
SPUTTER SYSTEM**

Base Vacuum, IG1 IG2

Date

Time

User

CATHODE #1

CATHODE #2

CATHODE #3

Seq #1

	Sputter Clean	R	Deposit R
Power, W set/act	300		300
Target Voltage, V	478		478
Time, min	3		20s
Pressure, mTorr	3.13		3.13
Gas	Ar		
Gas, sccm set/act	59	58.4	59 58.4
Substrate Temp, C			

Cu

Seq #2

	Sputter Clean	R	Deposit R
Power, W set/act	300		300
Target Voltage, V	357		335
Time, min	2		1.05
Pressure, mTorr	3.13		3.13
Gas	Ar		
Gas, sccm set/act	59	58.4	59 58.4
Substrate Temp, C			

Seq #3

Total Thickness, Å

Deposition Rate, Å/s

Sputter Control ☐ MAN ☐ AUTO

Requested by:

Sample ID

Comments

Substrate Bias

Seq #

Power (For,Rev), W

Substrate Voltage

Bias Time (min)

As-deposited

Stress (Flexus), MPa

Stress (Profile), MPa

Resistivity, μOhm-cm

Flexus Temp, C

Figure C.1: Recipe used to deposit Cr/Cu seed layer for nickel electroplating.

137

FutureFab Electroplating Bench

User Date Time

Au 01

Sample ID Wafer Qty and Size

Surface Area (cm²) Wafer Material

Current Density (mA/cm²) Mask Seed Layer

Duty Cycle (%) Control ☐ Manual ☐ Recipe

Avg Current (A) Dep Rate (μm/min) Recipe

Peak Solution Temp (C)

Amp-min Solution pH

Plate time (min) Solution Sp Gravity

Plated Thickness (μm) Resist Step

Post Plate Step

Calculated Plate Cumulative AmpHrs

NI 02

Sample ID Wafer Qty and Size

Surface Area (cm²) Wafer Material

Current Density (mA/cm²) Seed Layer

Duty Cycle (%) Solution Temp (C)

Avg Current (A) Solution pH

Peak Dep Rate (μm/min)

Amp-min Solution Sp Gravity

Plate time (min) Control ☒ Manual ☐ Recipe

Plated Thickness (μm) Recipe Cumulative AmpHrs

Cu 03

Plating calculations:
 Avg Current = Surface Area x Current Density
 Peak Current = Avg Current / Duty Cycle
 Amp-min = Avg Current x Plating Time
 Duty Cycle = On time/(On time + Off time)

Comments

Figure C.2: Recipe used for first two nickel electroplating attempts.

Appendix D: Experiments and Raw Data

Table D.1: Measured height and width of the 1.0 μm center traces.

Slide #		Trace 1	Trace 2	Trace 3	Trace 4	Trace 5
1	Height (\AA)	--	--	--	--	--
	Width (μm)	--	--	--	--	--
2	Height (\AA)	1.053	1.019	1.000	1.013	1.067
	Width (μm)	13.02	12.13	12.43	12.13	12.72
3	Height (\AA)	1.041	1.039	1.044	1.041	1.050
	Width (μm)	13.12	12.92	13.12	12.52	13.12
4	Height (\AA)	1.046	1.031	1.038	1.042	1.038
	Width (μm)	13.27	12.82	13.32	13.02	13.52

Table D.2: Measured height and width of the 0.25 μm center traces.

Slide #		Trace 1	Trace 2	Trace 3	Trace 4	Trace 5
5	Height (\AA)	2617	2640	2635	2634	2597
	Width (μm)	12.72	12.02	13.12	12.92	12.52
6	Height (\AA)	2641	2855	2751	2814	2717
	Width (μm)	12.52	12.32	12.92	12.52	12.72
7	Height (\AA)	2730	2637	2643	2648	2627
	Width (μm)	12.32	22.06	22.75	20	22.65
8	Height (\AA)	2629	2654	2656	2638	2715
	Width (μm)	12.52	12.42	13.31	12.62	12.12

Table D.3: Measured height and width of the 0.5 μm center traces.

Slide #		Trace 1	Trace 2	Trace 3	Trace 4	Trace 5
9	Height (\AA)	4975	5163	5116	5190	5212
	Width (μm)	12.92	11.92	12.62	12.62	12.92
10	Height (\AA)	5049	5083	5075	5064	5063
	Width (μm)	12.22	12.82	12.42	12.32	12.62
11	Height (\AA)	4962	5086	5039	5106	5295
	Width (μm)	12.92	13.02	13.32	13.51	14.60
12	Height (\AA)	--	--	--	--	--
	Width (μm)	--	--	--	--	--

Table D.4: Measured height and width of the 1.0 μm main traces.

Slide #		Trace 1	Trace 2	Trace 3	Trace 4	Trace 5
1	Height (\AA)	--	--	--	--	--
	Width (μm)	--	--	--	--	--
2	Height (\AA)	9.98	9.99	9.99	1.05	1.02
	Width (μm)	10.47	10.47	10.47	10.47	10.47
3	Height (\AA)	1.08	1.07	1.04	1.03	1.02
	Width (μm)	10.47	10.47	10.47	10.47	8.48
4	Height (\AA)	1.09	1.10	1.10	1.10	1.03
	Width (μm)	10.47	10.47	9.98	10.47	5.49

Table D.5: Measured height and width of the 0.25 μm center traces.

Slide #		Trace 1	Trace 2	Trace 3	Trace 4	Trace 5
5	Height (\AA)	--	2728.4	2672.8	2721.5	2688.0
	Width (μm)	--	10.54	10.54	10.04	11.03
6	Height (\AA)	2710.7	2854.4	2759.2	2767.3	2715.7
	Width (μm)	10.14	10.64	10.93	9.841	9.145
7	Height (\AA)	--	--	--	--	--
	Width (μm)	--	--	--	--	--
8	Height (\AA)	--	--	--	--	--
	Width (μm)	--	--	--	--	--

Table D.6: Measured height and width of the 0.5 μm center traces.

Slide #		Trace 1	Trace 2	Trace 3	Trace 4	Trace 5
9	Height (\AA)	--	--	--	--	--
	Width (μm)	--	--	--	--	--
10	Height (\AA)	--	--	--	--	--
	Width (μm)	--	--	--	--	--
11	Height (\AA)	--	--	--	--	--
	Width (μm)	--	--	--	--	--
12	Height (\AA)	--	5214.8	--	--	--
	Width (μm)	--	10.43	--	--	--

Table D.7: Voltage versus current measurements for Slide #2 (1 μm trace thickness).

Voltage (Ω)	Current					
	Trace 1	Trace 2	Trace 3	Trace 4	Trace 5	Average
1	0.006	0.007	0.007	0.007	0.006	0.0066
2	0.013	0.014	0.014	0.014	0.013	0.0136
3	0.020	0.021	0.021	0.020	0.019	0.0202
4	0.027	0.028	0.028	0.027	0.025	0.0270
5	0.033	0.035	0.034	0.033	0.030	0.0330
6	0.040	0.041	0.040	0.039	0.035	0.0390

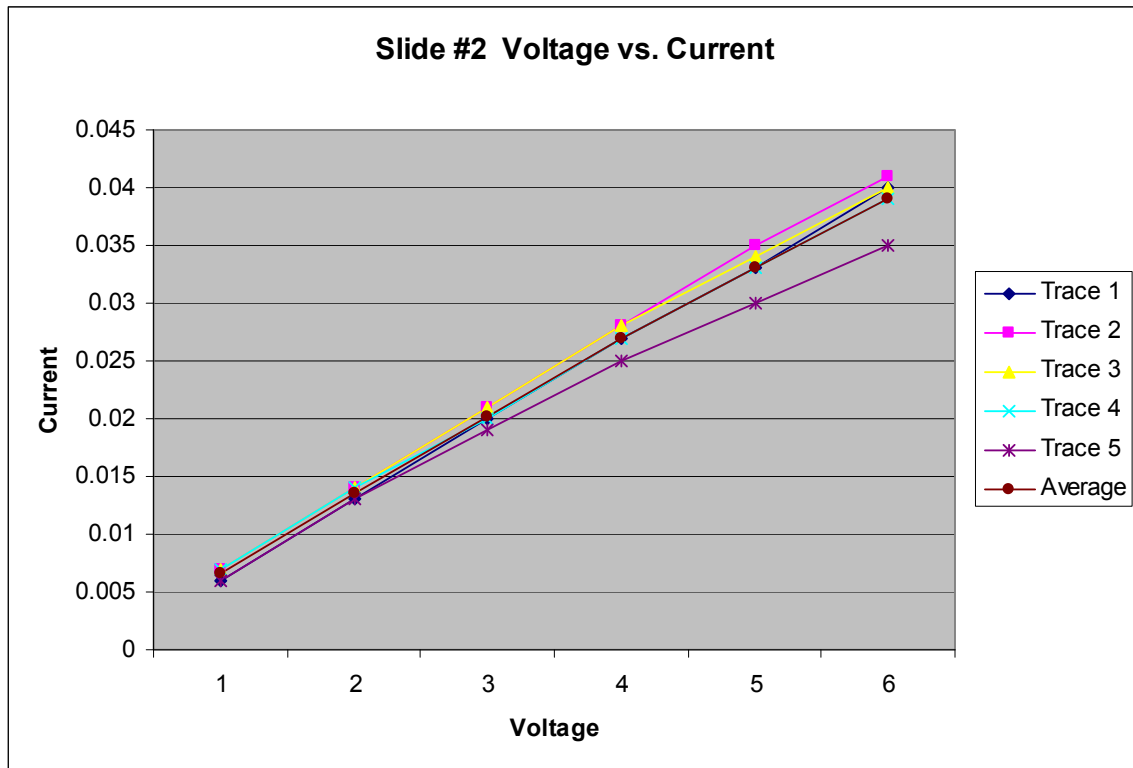


Figure D.1: Current vs. voltage plot for all five coils on slide #2 with an averaged plot line.

Table D.8: Voltage versus current measurements for Slide #3 (1 μm trace thickness).

Voltage (Ω)	Current					
	Trace 1	Trace 2	Trace 3	Trace 4	Trace 5	Average
1	0.007	0.007	0.007	0.007	X	0.007
2	0.014	0.015	0.015	0.014	X	0.0145
3	0.021	0.023	0.023	0.021	X	0.022
4	0.028	0.03	0.03	0.028	X	0.029
5	0.035	0.036	0.036	0.035	X	0.0355
6	0.041	0.043	0.042	0.04	X	0.0415

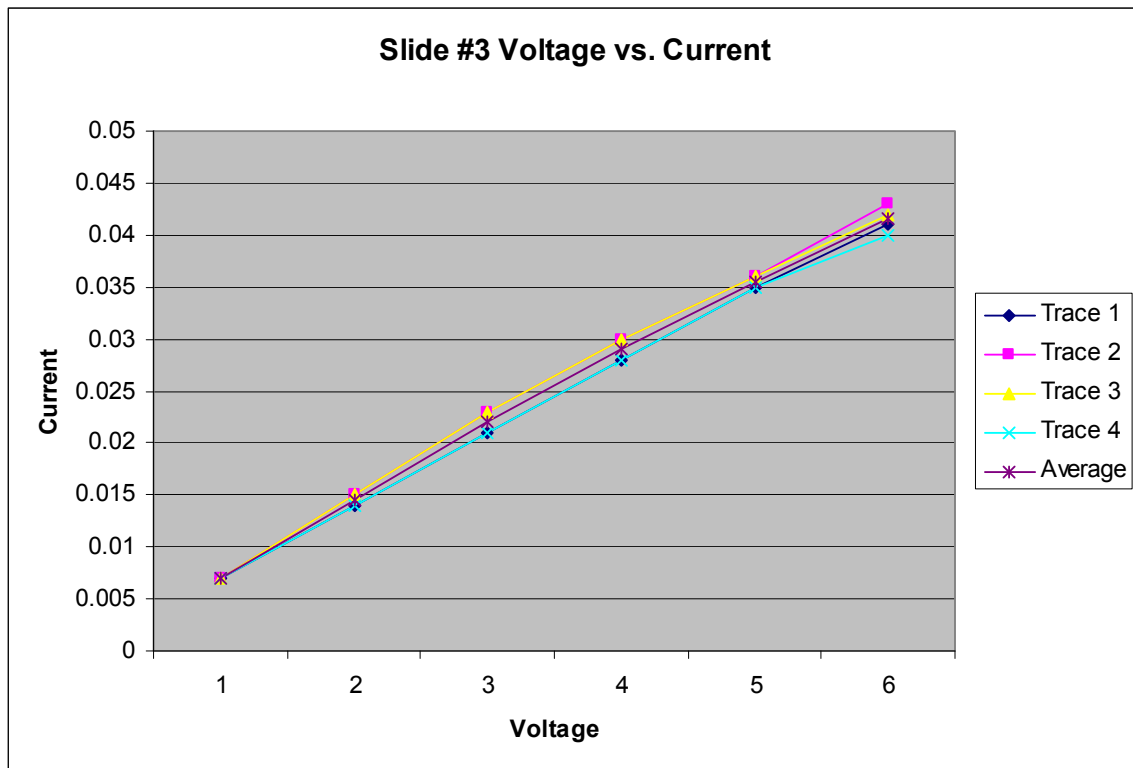


Figure D.2: Current vs. voltage plot for the remaining four coils on slide #3 with an averaged plot line.

Table D.9: Voltage versus current measurements for Slide #4 (1 μm trace thickness).

Voltage (Ω)	Current					
	Trace 1	Trace 2	Trace 3	Trace 4	Trace 5	Average
1	0.007	X	0.007	X	X	0.007
2	0.014	X	0.015	X	X	0.0145
3	0.021	X	0.023	X	X	0.022
4	0.028	X	0.03	X	X	0.029
5	0.034	X	0.037	X	X	0.0355
6	0.04	X	0.043	X	X	0.0415

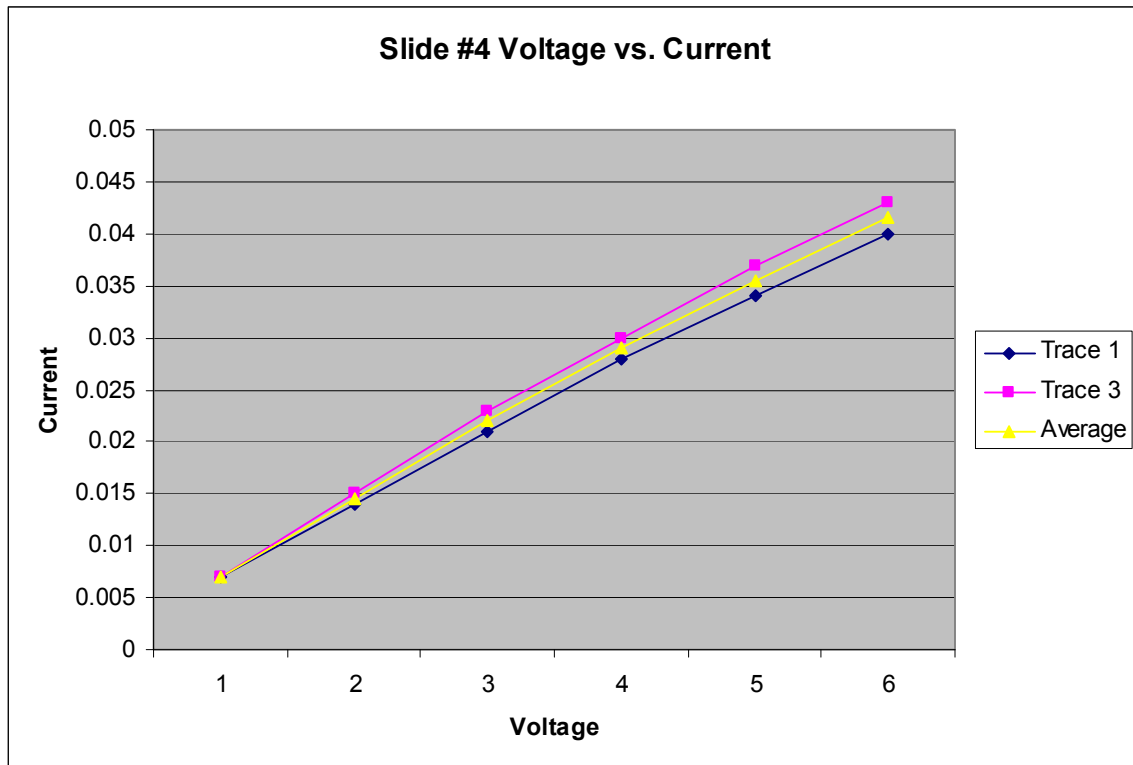


Figure D.3: Current vs. voltage plot for the remaining two coils on slide #4 with an averaged plot line.

Table D.10: Voltage versus current measurements for Slide #12 (0.5 μm trace thickness).

Voltage (Ω)	Current				
	Trace 1	Trace 2	Trace 3	Trace 4	Trace 5
1	X	0.003	X	X	X
2	X	0.007	X	X	X
3	X	0.011	X	X	X
4	X	0.015	X	X	X
5	X	0.018	X	X	X
6	X	0.021	X	X	X

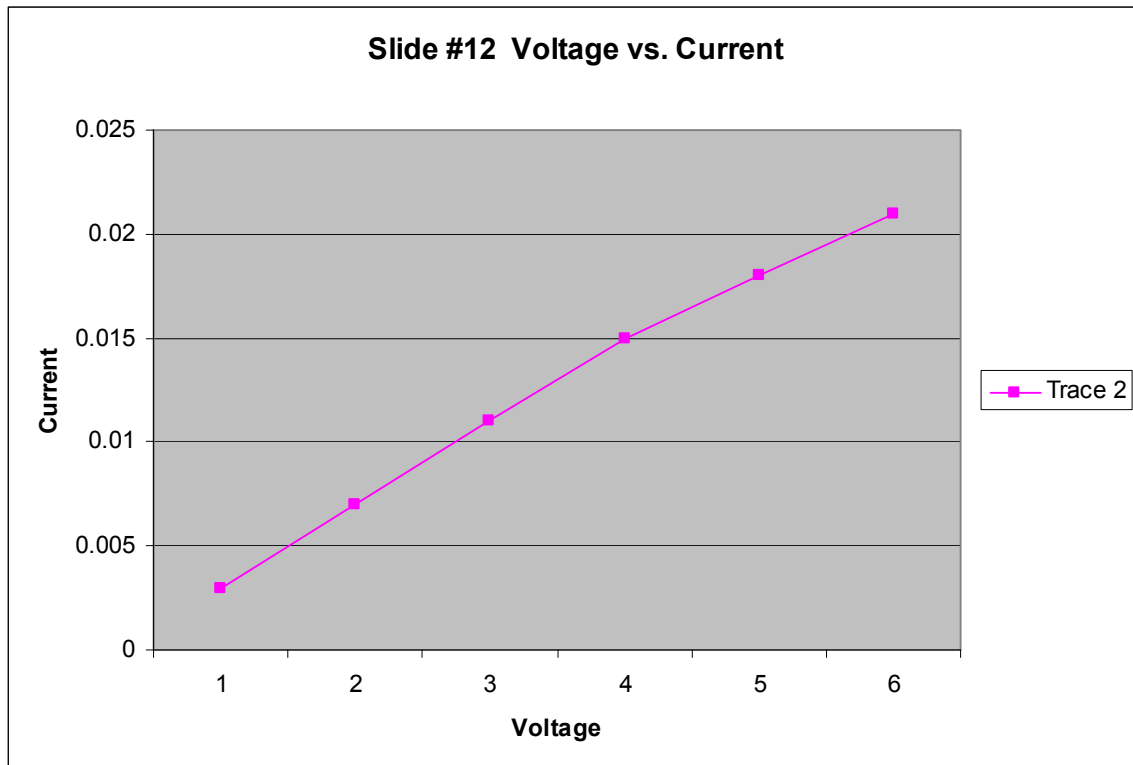


Figure D.4: Current vs. voltage plot for the one remaining coil on slide #12.

Table D.11: Voltage versus current measurements for Slide #5 (0.25 μm trace thickness).

Voltage (Ω)	Current					
	Trace 1	Trace 2	Trace 3	Trace 4	Trace 5	Average
1	X	0.002	0.002	0.002	0.002	0.002
2	X	0.004	0.004	0.004	0.004	0.004
3	X	0.006	0.006	0.006	0.006	0.006
4	X	0.008	0.008	0.008	0.008	0.008
5	X	0.01	0.01	0.01	0.01	0.01
6	X	0.012	0.012	0.012	0.012	0.012

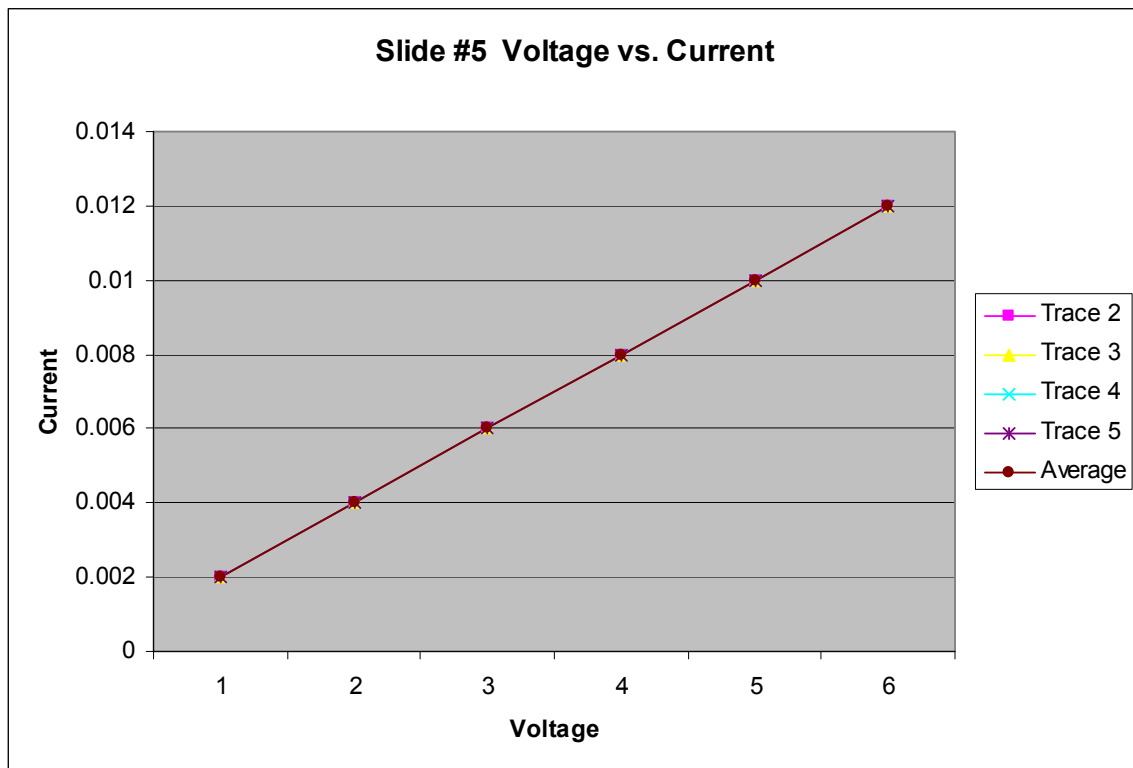


Figure D.5: Current vs. voltage plot for the remaining four coils on slide #5 with an averaged plot line.

Table D.12: Voltage versus current measurements for Slide #6 (0.25 μm trace thickness).

Voltage (Ω)	Current					
	Trace 1	Trace 2	Trace 3	Trace 4	Trace 5	Average
1	X	0.001	X	0.001	0.001	0.001
2	X	0.003	X	0.003	0.003	0.003
3	X	0.005	X	0.005	0.005	0.005
4	X	0.007	X	0.007	0.007	0.007
5	X	0.009	X	0.009	0.008	0.008667
6	X	0.011	X	0.011	0.01	0.010667

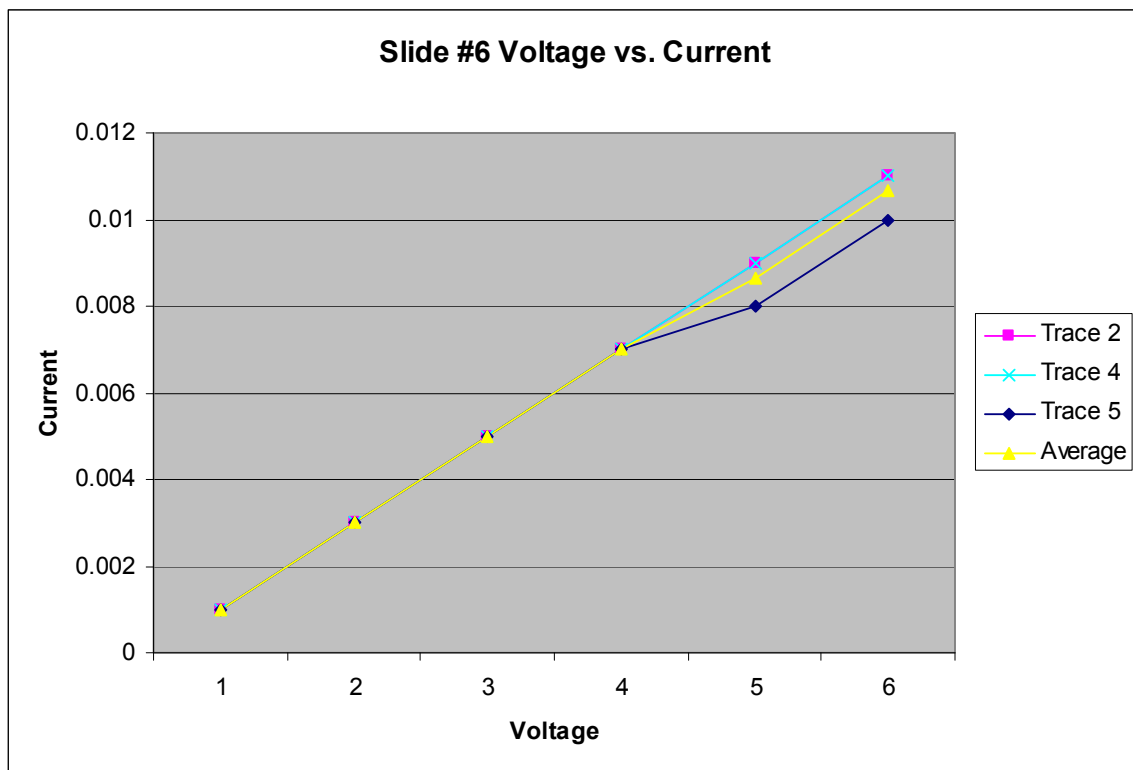


Figure D.6: Current vs. voltage plot for the remaining three coils on slide #6 with an averaged plot line.

Bibliography

- [1] K. C. Cheung and P. Renaud, "BioMEMS in Medicine: Diagnostic and Therapeutic Systems," in *Proceedings of ESSD ERC*, Grenoble, France, 2005, pp. 345 - 350.
- [2] M. Robert Hurd, "Monitor Blood Glucose - Series: Part 1." vol. 2007 Bethesda, MD: U.S. National Library of Medicine, 2007.
- [3] K. Peterson, *Micromachined Transducers Sourcebook Prologue*. San Jose, CA, 1998.
- [4] J. P. Wikswo, A. Prokop, F. Baudenbacher, D. Cliffl, B. Csukas, and M. Velkovsky, "Engineering Challenges of BioNEMS: The Integration of Microfluidics, Micro- and Nanodevices, Models, and External Control for Systems Biology," *IEEE Proceedings*, vol. 153, pp. 81-101, August 2006 2006.
- [5] R. Allan, "Implants Bring Hope to the Toughest Medical Handicaps," *Electronic Design*, June 29, 2007 2007.
- [6] "Micronit Microfluidics BV." vol. 2007 The Netherlands, 2007.
- [7] S. Franssila, *Introduction to Microfabrication*. West Sussex, England: Wiley, 2005.
- [8] R. K. Jain, "Paracrine Regulation of Angiogenesis and Adipocyte Differentiation During In Vivo Adipogenesis," *Journal of the American Heart Association: Circulation Research*, pp. 88 - 97, October 31, 2003 2003.
- [9] "Minimed Continuous Glucose Monitoring System, Summary of Safety and Effectiveness Data," Sylmar, CA: Minimed Inc., 1999.
- [10] K. D. Wise, "Wireless Implantable Microsystems: Coming Breakthroughs in Healthcare," in *Symposium on VLSI Circuits Digest of Technical Papers*, 2002, pp. 106 - 109.

- [11] Hutchinson, "Prehistoric Medicine." vol. 2007: Research Machines, plc, 2007.
- [12] "Islamic Culture and the Medical Arts," Bethesda, MD: National Library of Medicine, 2007.
- [13] "National Diabetes Fact Sheet," American Diabetes Association 2005.
- [14] M. Glenn Gandelman, "Pacemaker." vol. 2007 Bethesda, MD: U.S. National Library of Medicine, 2006.
- [15] P. Hemminger, "Science - Sampling and Extraction." vol. 2007.
- [16] "Polymicro Technologies, LLC," Phoenix, Arizona, USA, 2006.
- [17] B. J. McGuire and T. C. Secomb, "Estimation of Capillary Density in Human Skeletal Muscle Based on Maximal Oxygen Consumption Rates," *American Journal of Physiology Heart Circulatory Physiology* vol. 285, pp. 2382-2391, December 2003.
- [18] R. S. R. Gorla and A. A. Khan, *Turbomachinery Design and Theory*. New York: Marcel Dekker, Inc., 2003.
- [19] J. B. Calvert, "Turbines."
- [20] "Turbines," in *The Columbia Encyclopedia*: The Columbia University Press, 2006.
- [21] *Handbook of Turbomachinery*. New York: Marcel Dekker, Inc., 1995.
- [22] E. Bedi and H. Falk, "Hydro Power Technology." vol. 2007.
- [23] "Microhydropower System Turbines, Pumps, and Waterwheels." vol. 2007: U.S. Department of Energy.
- [24] G. L. Pollack and D. R. Stump, *Electromagnetism*. San Fransico: Addison Wesley, 2002.

- [25] "Battery (Voltaic Pile)." vol. 2007.
- [26] Y. B. Jeon, R. Sood, J.-h. Jeong, and S.-G. Kim, "MEMS Power Generator with Transverse Mode Thin Film PZT," Science Direct, 2004.
- [27] A. S. Holms, G. Hong, K. R. Pullen, and K. R. Buffard, "Axial-flow Microturbine with Electromagnetic Generator," in *17th IEEE International Conference on MEMS*, 2004, pp. 568 - 571.
- [28] J. L. Steyn, S. H. Kendig, R. Khanna, T. M. Lyszczarz, S. D. Umans, J. U. Yoon, C. Livermore, and J. H. Lang, "Generating Electric Power With a MEMS Electroquasistatic Induction Turbine-generator," in *18th IEEE International Conference on MEMS*, 2005, pp. 614 - 617.
- [29] N. W. Hagood, D. C. Roberts, and e. al., "Micro Hydraulic Transducer Technology for Actuation and Power Generation," in *Proceedings of SPIE*, 2000.
- [30] J. Yang, F. Lu, L. W. Kostiuk, and D. Y. Kwok, "Electrokinetic Power Generation via Streaming Potentials in Microchannels: A Mobile-Ion-Drain Method to Increase Streaming Potentials," in *Proceedings of the 2004 International Conference on MEMS, NANO, and Smart Systems (ICMENS '04)*, 2004.
- [31] R. A. Serway, *Physics For Scientists & Engineers with Modern Physics*, Fourth ed.: Saunders College Publishing, 1996.
- [32] F. M. White, *Viscous Fluid Flow*, Third Edition ed.: McGraw-Hill, 2006.
- [33] "How DRAs Work." vol. 2007 Waller, TX: Flowchem Pipeline improver Products.
- [34] "Laminar Flow," in *Encyclopedia Britannica*, 2007.
- [35] T. Caplow, "Poiseuille Flow Between Parallel Plates." vol. 2007.
- [36] J. Kimball, "The Human Circulatory System: How It Works." vol. 2007, 2006.

- [37] G. T. A. Kovacs, *Micromachined Transducers Sourcebook*: McGraw-Hill, 1998.
- [38] Z. S. Spakovszky and I. A. Waitz, "Unified: Thermodynamics and Propulsion." vol. 2007, 2006, p. MIT Lecture notes.
- [39] "Angular Velocity," in *Wikipedia*. vol. 2007.
- [40] J. Camacho and A. I. Olivia, "Surface and Grain Boundary Contributions in the Electrical Resistivity of Metallic Nanofilms," *Thin Solid Films*, vol. 2006, pp. 1881-1885, 13 July 2006 2006.
- [41] V. Pizzella, S. D. Penna, C. D. Gratta, and G. L. Romani, "SQUID Systems for Biomagnetic Imaging," *Institute of Physics Semiconductor Science Technology*, vol. 14, pp. R79 - R114, 25 April 2001 2001.
- [42] P. Fargis, *The New York Public Library Science Desk Reference*. New York: Macmillan, 1995.
- [43] "Voltaic Cells," in *Electrochemical Cells*. vol. 2007: Georgia State University.
- [44] T. Rabas, C. Panchal, and L. Genens, "Design and Cost of Near-term OTEC Plants for the Production of Desalinated Water adn Electric Power," U. S. D. o. Energy, Ed., 1990.
- [45] J. R. Stein and A. Meier, "Monitored Energy Use of Homes with Geothermal Heat Pumps: A Compilation and Analysis of Performance. Final Report," U. S. D. o. Energy, Ed., 1997.
- [46] H. Pearlman, "Hydroelectric Power Water Use." vol. 2007: United States Geological Survey.
- [47] S. Gawad, L. Schild, and P. Renaud, "Micromachined Impedance Spectroscopy Flow Cytometer for Cell Analysis and Sizing," *Lab on a Chip*, vol. 2001, pp. 76-82, Aug 13, 2001 2001.

- [48] C. D. Costin and R. E. Synovec, "Measuring the transverse concentration gradient between adjacent laminar flows in a microfluidic device by a laser-based refractive index gradient detector," *Talanta*, vol. 58, pp. 551 - 560, 2002.
- [49] L. Fielding, *Turbine Design*. New York: ASME Press, 2000.
- [50] C. R. Nave, "HyperPhysics." vol. 2007 Atlanta, GA: Georgia State University.
- [51] M. Gad-el-Hak, *The MEMS Handbook*. New York: CRC Press, 2002.
- [52] B. Gale, "Fabrication of Micromolding Using Electroplating of Nickel," University of Utah, 2004.
- [53] G. D. Bari, *ASM Handbook* vol. 5, Surface Engineering. Materials Park, OH: ASM International, 1994.
- [54] D. Hsu, "ChemiCool." vol. 2008, 2005.

Vita

Aaron Sprecher was born on Peas AFB, New Hampshire in 1979. After graduating from Warrensburg High School in 1997, Aaron joined the Air Force ROTC detachment at Northern Arizona University in Flagstaff, AZ. He left NAU in 1998 and completed his undergraduate degree in Electrical Engineering at the University of Texas at San Antonio in 2003. Upon completion of his degree, Aaron applied to the United States Air Force. He was accepted into Officer Training School and commissioned in September of 2003. His first assignment was to the Air Force Information Warfare Center as an information warfare systems engineer and later, as an information operations test engineer. Aaron entered the Air Force Institute of Technology in May 2006 and completed the Microelectronics and MEMS sequences. Following graduation from AFIT, he is assigned to work as a developmental engineer at the Air Force Research Laboratory Information Directorate.

REPORT DOCUMENTATION PAGE				Form Approved OMB No. 074-0188	
<p>The public reporting burden for this collection of information is estimated to average 1 hour per response, including the time for reviewing instructions, searching existing data sources, gathering and maintaining the data needed, and completing and reviewing the collection of information. Send comments regarding this burden estimate or any other aspect of the collection of information, including suggestions for reducing this burden to Department of Defense, Washington Headquarters Services, Directorate for Information Operations and Reports (0704-0188), 1215 Jefferson Davis Highway, Suite 1204, Arlington, VA 22202-4302. Respondents should be aware that notwithstanding any other provision of law, no person shall be subject to a penalty for failing to comply with a collection of information if it does not display a currently valid OMB control number.</p> <p>PLEASE DO NOT RETURN YOUR FORM TO THE ABOVE ADDRESS.</p>					
1. REPORT DATE (DD-MM-YYYY)		2. REPORT TYPE		3. DATES COVERED (From – To)	
28-03-2008		Master's Thesis		May 2006 – March 2008	
4. TITLE AND SUBTITLE MICROFLUIDIC POWER GENERATION				5a. CONTRACT NUMBER	
				5b. GRANT NUMBER	
				5c. PROGRAM ELEMENT NUMBER	
6. AUTHOR(S) Sprecher, Aaron J. Captain, USAF				5d. PROJECT NUMBER	
				5e. TASK NUMBER	
				5f. WORK UNIT NUMBER	
7. PERFORMING ORGANIZATION NAMES(S) AND ADDRESS(S) Air Force Institute of Technology Graduate School of Engineering and Management (AFIT/EN) 2950 Hobson Way, Building 640 WPAFB OH 45433-8865				8. PERFORMING ORGANIZATION REPORT NUMBER AFIT/GE/ENG/08-29	
9. SPONSORING/MONITORING AGENCY NAME(S) AND ADDRESS(ES) Nancy Kelley-Loughnane, Ph.D. Applied Biotechnology Branch AFRL/RHPB Area B, Bldg 837, 2729 R Street Wright Patterson Air Force Base, OH 45433-5707				10. SPONSOR/MONITOR'S ACRONYM(S) AFRL/RHPB	
				11. SPONSOR/MONITOR'S REPORT NUMBER(S)	
12. DISTRIBUTION/AVAILABILITY STATEMENT APPROVED FOR PUBLIC RELEASE; DISTRIBUTION UNLIMITED.					
13. SUPPLEMENTARY NOTES					
14. ABSTRACT This thesis includes the detailed mathematical calculations used to determine the feasibility of harnessing electrical energy from the blood flow through human capillaries. The designs are inspired by human physiology and well established electromagnetic energy harvesting techniques and the fabrication methods have been proposed for the various components of the device. The fabrication and the design of these components have also been extensively analyzed using calculations based on the governing principles of microfluidics, kinetics, and electromagnetics. The analysis has confirmed that this design can produce sufficient energy to power a MEMS device using non-standard materials and fabrication methods. The designs were based on a standard hydroelectric dam model, modified to account for the biological aspects. Nickel and gold were selected as the primary components of the electromagnetic portion of the device because of their electromagnetic properties and the ability to deposit and pattern them. Of the four portions of the device, the coil was fully fabricated, experiments were conducted for the fabrication of the stator and the microchannels and the proposed fabrication method was explained for the turbine. Three sets of the gold induction coils were fabricated, each with different thicknesses, but the same width and length. Since the resistance of the coil is determined by the resistivity of the material and the dimensions, the cross-sectional area of these coils determined the differences in resistance. As predicted, the average resistance increased as thickness decreased. However, the resistance was greater than calculated for the two thinner coil sets due to fabrication methods.					
15. SUBJECT TERMS Biological, Electromagnetic, Microfluidic, Power					
16. SECURITY CLASSIFICATION OF:			17. LIMITATION OF ABSTRACT	18. NUMBER OF PAGES	19a. NAME OF RESPONSIBLE PERSON
a. REPORT	b. ABSTRACT	c. THIS PAGE			Starman, LaVern, Maj, USAF
U	U	U	UU	175	19b. TELEPHONE NUMBER (Include area code) (937) 255-3636, ext 4618 (lavern.starman@afit.edu)

